Targeting Energy Metabolism in Brain Cancer

Author: Laura Marie Shelton

Boston College

The Graduate School of Arts and Sciences

Department of Biology

TARGETING ENERGY METABOLISM IN BRAIN CANCER.

A dissertation

By

LAURA MARIE SHELTON

Submitted in partial fulfillment of the requirements

for the degree of

Doctor of Philosophy

May 2010

ABSTRACT

TARGETING ENERGY METABOLISM IN BRAIN CANCER

Laura M. Shelton

Thesis Advisor: Thomas N. Seyfried

It has long been posited that all cancer cells are dependent on glucose for energy, termed the "Warburg Effect". As a result of an irreversible injury to the mitochondria, cancer cells are less efficient in aerobic respiration. Therefore, calorie restriction was thought to be a natural way to attenuate tumor growth. Calorie restriction lowers blood glucose, while increasing the circulation of ketone bodies. Ketone bodies are metabolized via oxidative phosphorylation in the mitochondria. Only cells that are metabolically capable of aerobic respiration will thus be able to acquire energy from ketone bodies. To date, calorie restriction has been shown to greatly reduce tumor growth and angiogenesis in the murine CT2A, EPEN, and human U87 brain tumor models. Using the novel VM-M3 model for invasive brain cancer and systemic metastatic cancer, I found that though calorie restriction had some efficacy in reducing brain tumor invasion and primary tumor size, metastatic spread was unaffected. Using a bioluminescent-based ATP assay, I determined the viability of metastatic mouse VM-M3 tumor cells grown *in vitro* in serum free medium in the presence of glucose alone (25 mM), glutamine alone (4 mM), or in glucose + glutamine. The VM-M3 cells could not survive on glucose alone, but could survive in glutamine alone indicating an absolute requirement for glutamine in these metastatic tumor cells. Glutamine could also maintain viability in the absence of glucose and in the presence of the F1 ATPase inhibitor oligomycin. Glutamine could not

maintain viability in the presence of the Krebs (TCA) cycle enzyme inhibitor, 3-nitropropionic acid. The data indicate that glutamine can provide ATP for viability in the metastatic VM-M3 cells through Krebs cycle substrate level phosphorylation in the absence of energy from either glycolysis or oxidative phosphorylation. I therefore developed a metabolic therapy that targeted both glucose and glutamine metabolism using calorie restriction and 6-diazo-5-oxo-L-norleucine (DON), a glutamine analog. Primary tumor growth was about 20-fold less in DON treated mice than in untreated control mice. I also found that DON treatment administered alone or in combination with CR inhibited metastasis to liver, lung, and kidney as detected by bioluminescence imaging and histology. Although DON treatment alone did not reduce the incidence of tumor metastasis to spleen compared to the controls, DON administered together with CR significantly reduced the incidence of metastasis to the spleen, indicating a diet/drug synergy. In addition, the phagocytic capabilities of the VM-M3 tumor cells were enhanced during times of energy stress. This allowed for the digestion of engulfed material to be used in energy production. My data provide proof of concept that metabolic therapies targeting both glucose and glutamine metabolism can manage systemic metastatic cancer. Additionally, due to the phagocytic properties of the VM-M3 cell line also seen in a number of human metastatic cancers, I suggest that a unique therapy targeting metabolism and phagocytosis will be required for effective management of metastatic cancer.

DEDICATION

To my parents, who have supported me in everything I choose to do. Your guidance, love, and support were integral to my success.

To my sister, who continues to be a role model for me. I am grateful to have been able to share this experience with you.

To my grandparents, whose prayers and support have helped me to achieve my goals.

To Steve, your love and support has always been unwavering, especially when I needed it the most.

ACKNOWLEDGEMENTS

I would like to thank first and foremost my mentor Dr. Thomas N. Seyfried for always pushing me to be a better scientist. Without his guidance and support this work could not have been possible. I would also like to thank the members of my committee, Dr. Thomas Chiles, Dr. Kenneth Williams, Dr. Richard Veech, and Dr. Mary Roberts for their guidance and input. I also need to thank Dr. Leanne Huysentruyt who was like a second mentor to me and with whom I discussed and developed many of my methods and ideas. I would also like to thank the members of the Seyfried lab: Julian Arthur, Dr. Purna Mukherjee, Xibei Ja, and Ivan Urits whose support and friendship helped me through this process. Lastly I would like to thank everyone in the Biology Department at Boston College.

TABLE OF CONTENTS

	PAGE
DEDICATION	i
ACKNOWLEDGEMENTS	ii
TALBE OF CONTENTS	iii
LIST OF FIGURES	vi
LIST OF TABLES	x
ABBREVIATIONS	xi
INTRODUCTION	
Human brain cancer models	1
Tumor metabolism	5
Calorie restriction	6
Role of glutamine	7
Macrophage properties of metastatic cancers	10
MATERIALS AND METHODS	
Cell lines	13
Cell Culture Conditions	13
Transduction of Cell lines	14
ATP and VM-M3 cell number curve	14
Experimental Medias	15
Metabolic Profiling	15
Drug Toxicity Curves	16
Oligomycin Sensitivity	17
Matrigel™ Phagocytosis Assay	17
Latex Bead Phagocytosis Assay	18
Collagen Coated Latex Bead Phagocytosis Assay	18
Ketone Transition	19
Ketone Determination	20
Lactate Determination	20
Ammonia Determination	20
Proton NMR	20
Mice	21
Origin of VM Tumors	21
Intracranial Implants	22
Subcutaneous Implants	23
Bioluminescent Imaging	23
Dietary/Drug Regimens, Body Weight, and Food Intake Measurements	24
Plasma and Serum Glucose Measurements	24
Histology	25
PCR	25
Immunohistochemistry and Confocal Microscopy	26

RESULTS

Comparison of invasive versus non-invasive brain tumors 28
Quantitative assessment of tumor growth 28
Detection and quantitation of VM-M3 invading tumor cells 28
Quantitation of distal tumor spread 29
Migratory routes of invading tumor cells 29
Expression of CXCR4 and IGFBP-2 in brain, tumor tissue, and cultured tumor cells 30
Ki-67 expression in VM-M3 tumors 30
Effect of calorie restriction on body weights, plasma glucose and ketones (i.c.) 31
Effect of calorie restriction on tumor growth and invasion 31
The VM-M3 tumor as a model for systemic metastatic cancer 32
Effect of calorie restriction on body weights, plasma glucose and ketones (s.c.) 32
Effect of calorie restriction on tumor growth and metastasis 33
Differential response to energy stress between CT-2A and VM-M3 cell lines *in vitro* 33
VM-M3 lactate production under energy stress 33
VM-M3 cell survival in both glucose and glutamine 34
Survival of VM-M3 cells in varying glucose and glutamine concentrations 34
Effect of *meso*-Tartrate on VM-M3 cell viability 35
Effect of the TCA cycle inhibitor 3-NP on VM-M3 cell viability 35
Effect of fatty acid metabolism on VM-M3 cell viability 36
Effect of ketones on VM-M3 cell viability *in vitro* 36
Oligomycin sensitivity of the VM-M3 and CT-2A tumor cell lines 36
Effect of diadenosine pentaphosphate on VM-M3 cell viability 37
In vitro effect of DON on the VM-M3 cell line 37
Effect of DON and DON + CR on body weights, blood glucose and ketones 37
Effect of DON and DON + CR on tumor growth and metastasis 38
Effect of DON and DON + CR on mouse survival 39
Effect of CQ on CT-2A and VM-M3 cell viability *in vitro* 39
Effect of CQ on VM-M3 cell viability in a Matrigel™ Matrix 40
Effect of CQ on CT-2A cell viability in a Matrigel™ Matrix 40
Latex bead phagocytosis 41
Effect of CQ on tumor growth and metastasis 41
Effect of CQ on brain tumor growth and invasion 42
Astrocyte transition to a low glucose, high ketone media *in vitro* 42
Effect of phenylbutyrate on VM-M3 survival *in vitro* 42
Correlation between ATP concentration, cell number and bioluminescence 43

DISCUSSION 176

CONCLUSION 198

APPENDIX 200

REFERENCES 203

LIST OF FIGURES

PAGE

1. Comparative analysis of the growth behavior of mouse brain tumors VM-M3 and the CT-2A malignant astrocytoma 45

2. Growth of the VM-M3/Fluc tumor with bioluminescence imaging 47

3. Detection of VM-M3/Fluc tumor cell invasion into the contralateral hemisphere with bioluminescence imaging and histology 49

4. Bioluminescent analysis of distal tumor spread to the cortex and hippocampus 51

5. Histological evaluation of distal tumor spread to the cortex and hippocampus 53

6. Bioluminescent analysis of distal tumor spread to the brain stem and cerebellum 55

7. Histological evaluation of distal tumor spread to the brain stem and cerebellum 57

8. Migratory routes of the VM-M3/Fluc brain tumor cells 59

9. Expression of CXCR4 and IGFBP-2 in brain, tumor tissue, and in cultured tumor cells 61

10. CXCR4 protein localization in VM-M3 tumor and cells *in vitro* 63

11. Expression of CXCR4 in invasive VM-M3 tumor cells *in vivo* 65

12. Ki-67 expression in VM-M3 tumor 67

13. Experimental design 69

14. Effect of calorie restriction on VM-M3/Fluc tumor bearing mice 71

15. Influence of calorie restriction on VM-M3/Fluc tumor growth 73

16. Influence of calorie restriction on bioluminescence in the contralateral hemisphere 75

17. Influence of calorie restriction on VM-M3/Fluc tumor cell invasion to the contralateral hemisphere 77

18. Influence of calorie restriction on Ki-67 staining in the primary tumor 79

19. Growth and metastatic spread of the VM-M3/Fluc tumor with bioluminescence imaging 81

20. Experimental design 83

21. Effect of calorie restriction on VM-M3/Fluc tumor bearing mice 85

22. Effect of calorie restriction on VM-M3/Fluc primary tumor size 87

23. Effect of calorie restriction on VM-M3/Fluc tumor metastasis 89

24. A differential response to energy stress *in vitro* between CT-2A and VM-M3 tumor cell lines 91

25. VM-M3 lactate production under energy stress 93

26. Effect of glucose and glutamine on VM-M3 viability 95

27. VM-M3 lactate production in the presence of both glucose and glutamine 97

28. VM-M3 cell viability in varying glucose and glutamine concentrations 99

29. Effect of *meso*-Tartrate on VM-M3 cell viability under energy stress 101

30. Effect of *meso*-Tartrate on VM-M3 lactate production 103

31. Effect of 3-Nitropropionic acid on VM-M3 cell viability under energy stress 105

32. Effect of fatty acid metabolism on VM-M3 cell viability in glutamine 107

33. Effect of ketones on VM-M3 cell viability *in vitro* 109

34. Effect of oligomycin on VM-M3 and CT-2A cell viability under energy stress 111

35. Effect of oligomycin on CT-2A lactate production 113

36. Effect of diadenosine pentaphosphate on VM-M3 viability under energy stress 115

37. Effect of DON on VM-M3 cell viability *in vitro* 117

38. Experimental design 119

39. Effect of DON and DON + CR on VM-M3/Fluc tumor bearing mice 121

40. Effect of DON and DON + CR on VM-M3/Fluc tumor growth 123

41. Effect of DON and DON + CR on VM-M3/Fluc tumor metastasis 125

42. Influence of DON and DON + CR on liver histology 127

43. Influence of DON and DON + CR on VM mouse survival 129

44. Effect of Chloroquine on VM-M3 and CT-2A cell viability *in vitro* 131

45. *In vitro* effect of Chloroquine on VM-M3 cell viability in Matrigel™ Matrix 133

46. *In vitro* effect of Chloroquine and Matrigel™ Matrix on VM-M3 cell viability while under energy stress 135

47. Effect of Matrigel™ Matrix on VM-M3 lactate production under energy stress 137

48. *In vitro* effect of Chloroquine on CT-2A cell viability in Matrigel™ Matrix 139

49. *In vitro* effect of Chloroquine and Matrigel™ Matrix on CT-2A cell viability while under energy stress 141

50. Phagocytic behavior of the VM-M3 cell line 143

51. Effect of collagen coated latex beads on VM-M3 viability under energy stress 145

52. Effect of collagen coated latex beads on VM-M3 lactate and ammonia production under energy stress 147

53. Experimental design 149

54. Effect of Chloroquine on VM-M3/Fluc primary tumor size 151

55. Effect of Chloroquine on VM-M3/Fluc tumor metastasis 153

56. Effect of Chloroquine and CR on VM-M3/Fluc primary tumor size 155

57. Effect of Chloroquine and CR on VM-M3/Fluc tumor metastasis 157

58. Experimental design 159

59. Effect of Chloroquine on VM-M3/Fluc brain tumor growth and invasion 161

60. Effect of Chloroquine and CR on VM-M3/Fluc brain tumor growth and invasion 163

SUPPLEMENTAL FIGURES

1. Ketone transitioned astrocytes in culture 167

2. Effect of Phenylbutyrate on VM-M3 cell viability *in vitro* 169

3. Schematic representation of metabolic pathways 171

4. Proposed mechanism by which glutamine maintains viability in the VM-M3 cell line 173

5. Correlation between ATP concentration, VM-M3 cell number and bioluminescence 175

LIST OF TABLES

	Page
1. Percentage of animals with metastasis to organs (CR)	164
2. Percentage of animals with metastasis to organs (DON + CR)	165

ABBREVIATIONS

2DG	2-deoxy-glucose
3-NP	3-nitropropionic acid
AC	astrocyte type III clone cell line
AL	ad libitum
Ap5A	diadenosine pentaphosphate
ATP	adenosine tri-phosphate
B6	C57BL/6J mouse strain
β-OHB	β-hydroxybutyrate
cDNA	complimentary DNA
C.I.	confidence interval
CMV	cytomegalovirus
Col	collagen
CQ	chloroquine
CR	calorie restriction
CT-2A	chemically induced mouse astrocytoma
CXCL-12	chemokine
CXCR4	chemokine receptor
DMEM	Dulbecco's Modified Eagle medium
DNA	deoxyribonucleic acid
DON	6-Diazo-5-oxo-L-norleucine
EGFP	enhanced green florescent protein
EPEN	chemically induced mouse ependymoma
ETC	electron transport chain
FBS	fetal bovine serum
Fluc	firefly luciferase
GBM	Glioblastoma multiforme
Gln	glutamine
Gluc	glucose
HA	heptanoic acid
H & E	haematoxylin and eosin
i.c.	intracerebrally
IGFBP-2	insulin-like growth factor binding protein 2
i.p.	intra-peritoneal
IRES	internal ribosome entry site
IVIS	in vivo imaging system
Ki-67	proliferation marker
LB	latex beads
LTR	long terminal repeats
Meso	meso-Tartrate
MOI	multiplicity of infection

PBA	phenylbutyrate
PCR	polymerase chain reaction
PBS	phosphate buffered saline
PPP	pentose phosphate pathway
RNA	ribonucleic acid
RT	reverse transcriptase
s.c.	subcutaneously
SEM	standard error of the mean
TCA	tri-carboxylic acid cycle
U-87	human xenograft glioma
VM	VM/Dk mouse strain
VM-M3	spontaneous murine metastatic brain tumor
VM-M3/Fluc	the VM-M3 murine metastatic brain tumor expressing firefly luciferase
VM-NM1	spontaneous murine non-metastatic/non-invasive brain tumor

INTRODUCTION

Human brain cancer models

Glioblastoma multiforme (GBM) is the most common form of adult brain cancer (Wen and Kesari 2008). GBM has a poor outcome due to its invasive and aggressive nature. Treatments have been largely ineffective and consist of surgical resection followed by radiation and/or chemotherapy (Chang et al. 2005; Wen and Kesari 2008). Due to the invasive nature of GBM, complete surgical removal is not possible. Many GBMs are multicentric, having secondary lesions at sites distant to the primary tumor (Scherer 1940a; Rubinstein 1972; Laws et al. 1993). In addition, chemotherapy and radiation are toxic, often resulting in further brain damage (Duffner 2006). In order to develop better therapies, reliable animal models are required that focus on the invasive nature of GBM. Although a number of brain tumor models exist, none recapitulate all of the characteristics of a human GBM, such as the typical growth patterns and infiltrative behavior (Szatmari et al. 2006). While xenograft models are attractive, the mouse hosts are immune compromised and ignore the effect of an immune-mediated response when assessing potential therapies as well as the effects of a native host microenvironment (Candolfi et al. 2007; Xie et al. 2008; Huse and Holland 2009). Additionally, xenografted human tumors tend to lose their invasive properties when grown *in vivo* following *in vitro* culturing (Fomchenko and Holland 2006). Growth patterns in xenografts also do not replicate the growth patterns seen in humans with GBM (Fomchenko and Holland 2006; Candolfi et al. 2007; Huse and Holland 2009). New

animal models for GBM are therefore needed that better reflect the properties seen in the natural host.

Chemically induced models are grown in immune competent hosts, and to date are some of the most commonly used murine syngeneic brain tumor models (Mukherjee et al. 2002; Mukherjee et al. 2004; Maes et al. 2008). However, these brain tumors lack glial differentiation markers, typical GBM growth patterns, and extensive invasion (Szatmari et al. 2006; Maes et al. 2008). Rat brain tumor models are also available but are highly immunogenic thus complicating results of potential therapies (Barth 1998). There is also evidence of spontaneous tumor regression in some rat models of brain cancer (Vince et al. 2004). The rat CNS-1 glioma model is useful for assessing immuno-based therapies because it is weakly immunogenic and has greater invasive properties than those seen in the more common rat glioma models to include periventricular and perivascular spread (Kruse et al. 1994). The leptomeningeal spread however, could also be a result of the inoculation method (Kruse et al. 1994). In general, the invasive properties of most rodent models are limited to within the area of the main tumor mass (Candolfi et al. 2007; Zagzag et al. 2008). Hence, none of the currently available rodent brain tumor models reflect the growth characteristics of human GBM.

Due to the limitations of current brain tumor models, transgenic models have been developed based on gain of function or targeted deletions in glioma-associated genes (Holland 2001). Complicated breeding and genotyping procedures however are required

to generate these transgenic models (Dai and Holland 2001; Holland 2001; Hu and Holland 2005). Though these transgenic models often replicate high-grade gliomas, a model with a mutation in a single pathway is not a realistic representation of the human disease because human gliomas contain a number of distinct genetic abnormalities (Louis 2006; Parsons et al. 2008; Huse and Holland 2009). Also, the tumors that develop are not always identical in morph or grade (Huse and Holland 2009). As an alternative, MMLV (moloney murine leukemia virus)-based somatic gene-transfer glioma models rely on retroviral infection of glial cells (Dai and Holland 2001; Assanah et al. 2006). This method allows for the delivery of multiple genes thus bypassing the production of additional transgenic lines (Huse and Holland 2009). However, retroviral infection is often non-specific, targeting numerous cells and resulting in heterogeneous tumors of unknown origin (Dai and Holland 2001; Hu and Holland 2005).

In addition to the available rodent models, a number of dog breeds are predisposed to spontaneous brain tumors to include boxers and golden retrievers (Heidner et al. 1991; LeCouteur 1999). Some of these brain tumors are highly invasive and closely resemble the histological and growth characteristics of human GBM (Lipsitz et al. 2003; Candolfi et al. 2007). However, dog models are not readily available and researchers would need to rely on the recruitment of recently diagnosed dogs for studies (Candolfi et al. 2007). The specific grade and type of dog glioma also varies and only about 5% of all dog brain tumors are GBM (Foster et al. 1988; Lipsitz et al. 2003).

The VM-M3 tumor is unique in that it arose spontaneously in the brain of the VM mouse strain. The VM strain is known to have a relatively high incidence (1.5%) of spontaneous brain tumors most of which are described histologically as astrocytomas (Fraser 1971, 1986a). The VM-M3 brain tumor expresses multiple properties of microglia similar to that seen in numerous other types of invasive/metastatic cancers of neural and non-neural origin (Huysentruyt et al. 2008; Huysentruyt et al. 2010). In addition, the VM-M3 tumor cells highly express the chemokine receptor CXCR4, whose expression has been linked to the degree of malignancy of human gliomas and has been found to play a major role in tumor cell migration (Bian et al. 2007; Ehtesham et al. 2008; Huysentruyt et al. 2008; Stevenson et al. 2008; Zagzag et al. 2008). High CXCR4 levels are more often associated with the higher-grade gliomas, including GBM and indicate a poor postoperative prognosis (Bian et al. 2007). The VM-M3 tumor is highly invasive when implanted orthotopically and invading tumor cells can be found deep within the brain parenchyma. These tumors are weakly immunogenic and can be grown in the syngeneic VM mouse host with predictable and reproducible growth rates and patterns (Huysentruyt et al. 2008; Huysentruyt et al. 2010). In addition, the VM-M3 tumors are labeled with the firefly luciferase gene allowing for non-invasive detection of tumor growth via bioluminescent imaging (Huysentruyt et al. 2008; Huysentruyt et al. 2010). Bioluminescent imaging has been developed for a number of glioma tumor model systems and is established as an accurate measurement of tumor growth over time (Deroose et al. 2006; Szentirmai et al. 2006; Maes et al. 2008). Therefore, the VM-M3

tumor manifests several of the characteristics seen in aggressive malignant gliomas to include GBM.

Tumor metabolism

Over 70 years ago, Otto Warburg theorized that all cancer cells are heavily dependent on glycolysis, which was later termed "The Warburg Effect". This theory was based on metabolic studies in a large number of carcinomas, including lung, colon, skin, and larynx (Warburg 1931). A high rate of glycolysis was found in tumors with low oxygen uptake. The release of lactic acid was correspondingly high in the carcinomas even in the presence of oxygen, thus suggesting that all tumor cells suffered from a disturbance of respiration. A mitochondrial dysfunction was thought to be the cause of the respiration impairment and hence the "origin of cancer cells" (Warburg 1956). As a result, tumor cells were thought to be strictly reliant on glucose for energy. Therefore, exploiting abnormal brain tumor metabolism is an attractive therapeutic target. Under normal physiological conditions brain cells acquire most, if not all of their energy from glucose (Seyfried and Mukherjee 2005a). However, under conditions of fasting or low blood glucose, normal tissue as well as the brain is capable of utilizing ketone bodies for energy (Owen et al. 1967; Cahill 1970; VanItallie and Nufert 2003; Morris 2005). β-hydroxybutyrate is the main blood ketone that is capable of crossing the blood brain barrier through the monocarboxylic acid transporters (MCTs) (Koehler-Stec et al. 1998; Pellerin et al. 2005). Although astroctyes are highly glycolytic in cell culture, they maintain the capabilities to perform oxidative phosphorylation. It has been shown that

astrocytes will shift to fatty acid oxidation during glucose withdrawal (Jelluma et al. 2006). An impaired respiration would prevent tumors from utilizing ketones as an energy source because ketones are oxidized to acetyl Co-A and directly enter the TCA (VanItallie and Nufert 2003). Hence, a diet therapy based on reducing glucose levels while maintaining high ketone levels may prove effective in the treatment of cancers that rely on glycolysis (Magee et al. 1979; Mukherjee et al. 2002; Mukherjee et al. 2004; Zhou et al. 2007).

Calorie Restriction

Cancer cells frequently exhibit increased glycolysis and therapies that target glucose metabolism have been exploited in the past to include 2-deoxyglucose (2-DG) and calorie restriction (CR) (Mukherjee et al. 2002; Mukherjee et al. 2004; Marsh et al. 2008a). Calorie restriction is a powerful anti-angiogenic therapy that also reduces tumor growth in various mouse and human xenograft models of brain cancer (Mukherjee et al. 2002; Mukherjee et al. 2004; Marsh et al. 2008a). In addition, calorie restriction has been shown to target Akt signaling pathways involved in the antiapoptotic and glycolytic phenotype of some tumors (Marsh et al. 2008b). Calorie restriction is an effective tool for reducing circulating blood glucose, thereby limiting this energy source to the tumor cells. Calorie restriction also acts by elevating ketone bodies due to the lowered blood glucose levels, which as previously stated, can be metabolized by oxidative phosphorylation in normal healthy cells (Seyfried and Mukherjee 2005a). Because tumor cells have an impaired respiration, ketone bodies cannot be used as an energy substrate.

In addition, calorie restriction reduces the production of free radicals and thus reduces inflammation (Veech 2004; Seyfried and Mukherjee 2005b). Evidence has since confirmed that high blood glucose levels act as an accurate biometric predictor of poor survival in humans with Glioblastoma multiforme (McGirt et al. 2008; Derr et al. 2009). To date, the effect of calorie restriction has not been tested on invasive brain cancer in mice.

Role of Glutamine

In recent years a focus has shifted to the role glutamine plays in the growth of cancer cells. It has long been known that glutamine is essential for rapidly dividing cells, cells of myeloid origin, fibroblasts in culture, and cancer cells (Zielke et al. 1976; McKeehan 1982; Kovacevic and McGivan 1983; Newsholme et al. 1985; Newsholme et al. 1987; Baggetto 1992; Medina 2001; Yuneva 2008). Tumors have been termed "glutamine traps," consistent with their ability to take in exceedingly large amounts of glutamine relative to the rest of the body (Souba 1993; Medina 2001). In addition to enhanced expression of glutamine transporters, enzyme activities such as glutaminase, which are involved in glutamine metabolism, are elevated in a number of tumors (Board et al. 1990; Perez-Gomez et al. 2005). Evidence has shown a correlation between enhanced tumor glutaminase activity and enhanced malignancy (Souba 1993; Medina 2001). Glutamine was believed to play a role in macromolecular synthesis particularly of purines and pyrimidines and as a precursor in anapleurotic reactions (DeBerardinis et al. 2007; DeBerardinis 2008; Deberardinis et al. 2008). In this capacity, it was thought that

glutamine was converted to pyruvate via mitochondrial malate and ultimately to lactic acid. This would regenerate NADPH to be used in the pentose phosphate pathway and fatty acid synthesis (DeBerardinis et al. 2007; DeBerardinis 2008). However, it was determined that glutamine intake far exceeded macromolecular synthesis and instead was used as an energy substrate (Reitzer et al. 1979; DeBerardinis et al. 2007; Matheson et al. 2007). Evidence has indeed shown that glutamine, not glucose, is the major source of energy for HeLa cells (Reitzer et al. 1979). However, there is debate as to the origin of this ATP, as cancer cells frequently exhibit mitochondrial respiratory impairments (Warburg 1956; Kiebish et al. 2008a; Ortega et al. 2009).

Glutamine is capable of entering a truncated TCA cycle whereby it can be converted back to pyruvate via malate. However, this could occur either at the expense of TCA malate as well as at the expense of extramitochondrial malate (See Supplemental Figures 3 and 4). The first possibility is that TCA malate exits the mitochondria and is converted to pyruvate via cytosolic malic enzyme (Newsholme et al. 2003b; DeBerardinis et al. 2007; Deberardinis et al. 2008). In addition, citrate is capable of exiting the mitochondria resulting in the production of extramitochondrial malate (Sauer and Dauchy 1978; McKeehan 1982; Moreadith and Lehninger 1984; Baggetto 1992; Teller et al. 1992). Extramitochondrial malate is derived from citrate via the sequential action of ATP citrate lyase and malate dehydrogenase. This takes place in the cytoplasm where citrate from the TCA is used to generate acetyl-CoA for fatty acid synthesis (Baggetto 1992; Board and Newsholme 1996). Extramitochondrial malate re-enters the mitochondria where

mitochondrial malic enzyme regenerates pyruvate (Kovacevic and McGivan 1983; Moreadith and Lehninger 1984), thus allowing acetyl-CoA to continually feed into the TCA. This could potentially allow for the continual generation of ATP via substrate level phosphorylation in the TCA in the absence of oxidative phosphorylation. In the same manner, cytosolic pyruvate derived from mitochondrial malate is capable of re-entering the TCA as acetyl-CoA. However, DeBeradinis et al. demonstrated that glutamine derived pyruvate generated from TCA malate is more frequently converted to lactic acid (DeBerardinis et al. 2007). Therefore, it is unclear whether glutamine primarily plays an active role in macromolecular synthesis and anapleurosis or whether it can also serve as an energy generating substrate.

Currently, there are a number of drug targets of glutamine metabolism to include phenylbutyrate (PBA), and the glutamine analogs acivicin and 6-diazo-5-oxo-L-norleucine (DON) (Livingston et al. 1970; Darmaun et al. 1998). PBA has been used extensively *in vitro* and in human trials as a histone deacetylase inhibitor (Engelhard et al. 1998; Dyer et al. 2002; Li et al. 2004; Lopez et al. 2007). In the body, PBA is metabolized to phenylacetate (PA) by β-oxidation (Darmaun et al. 1998). PA then covalently conjugates with glutamine via phenylacetyl-CoA ligase and acyl-CoA-L-glutamine N-acyl-transferase (Darmaun et al. 1998). This glutamine-PA conjugate is then excreted, effectively reducing the amount of free glutamine available to the tumor cells. The glutamine analogs have also shown promising results *in vitro* and in murine models of cancer (Rabinovitz et al. 1959; Ovejera et al. 1979; Lyons et al. 1990; Griffiths

et al. 1993). However, limited success has been achieved with PBA, and high toxicities of the glutamine analogs limit their use for human studies (Magill et al. 1957; Livingston et al. 1970; Griffiths et al. 1993; Phuphanich et al. 2005)

Macrophage properties of metastatic cancers

Recent evidence indicates that metastatic cancers display multiple properties of macrophages. In particular, phagocytosis appears to be an important mechanism employed by metastatic cancer cells (Fais 2007). Metastatic breast cancer cells were found to internalize fluorescent Matrigel™, latex beads, and yeast (Montcourrier et al. 1994; Coopman et al. 1996; Coopman et al. 1998; Ghoneum and Gollapudi 2004). This phagocytic capacity was observed among the more aggressive and invasive cell lines studied (Montcourrier et al. 1994). In addition, tumor phagocytosis of erythrocytes as well as other tumor cells was found in a patient with a cerebellar medulloblastoma (Youness et al. 1980). However, this mechanism seems to function particularly when the tumor cells have become nutrient stressed (Fais 2007). Metastatic melanoma cells were shown to survive on human T-lymphocytes when stressed by a reduction of nutrients (Lugini et al. 2006). This perhaps allows the tumor cells to avoid autophagy, which is a self-destructive process (Fais 2007). Therefore, phagocytosis could perhaps become a novel target of anticancer therapies, particularly for the invasive and metastatic cancers.

Currently, a few reports have suggested potential anti-cancer effects of cholorquine (CQ), a traditional anti-malarial compound (Zeilhofer et al. 1989; Briceno et al. 2007; Maclean

et al. 2008). Specifically, CQ targets to the lysosomes, raising intra-lysosomal pH (Pless and Wellner 1996). As a result, lysosomal digestive enzymes are rendered inactive (Fredericksen et al. 2002). Chloroquine is thought to exert its effect by inhibiting the autophagy pathway (Dang 2008; Maclean et al. 2008). Also termed "self-eating", this pathway allows for the digestion of internal organelles during times of nutrient deprivation (Fais 2007; Dang 2008). However, inhibiting the digestion of phagocytosed extracellular material would represent a novel use for chloroquine. The therapeutic effects of choloquine should be at a maximum when the tumor cells are stimulated to phagocytose. If nutrient deprivation is a phagocytic trigger, then calorie restriction combined with chloroquine could exert a significant amount of stress on the tumor cells, resulting in cell death.

The VM-M3 cell line has a number of myeloid properties to include morphology, gene expression, lipid profile, and phagocytic capacity (Huysentruyt et al. 2008). This tumor arose spontaneously in the brain of a VM mouse and has multiple properties of Glioblastoma multiforme to include systemic metastasis (Ng et al. 2005). While metastasis is not commonly seen in gliomas, GBM is highly metastatic once the tumor cells reach the blood stream (Rubinstein 1972; Youness et al. 1980; Hoffman and Duffner 1985; Taha et al. 2005; Kauffman et al. 2007). From a subcutaneous implantation site, the VM-M3 tumor recapitulates all the major hallmarks of metastasis, to include detachment from the primary tumor, intravasation into the blood stream, evasion of immune attack, extravasation at a distant capillary bed, and growth at distant sites

(Chambers et al. 2002; Bacac and Stamenkovic 2008; Huysentruyt et al. 2008; Huysentruyt et al. 2010). In addition, this tumor has multiple properties of myeloid cells also seen in a number of human metastatic cancers to include lung, breast, colon, and skin (Spivak 1973; Abodief et al. 2006; Lugini et al. 2006; Fais 2007; Huysentruyt et al. 2008; Moonda and Fatteh 2009; Huysentruyt et al. 2010). It has been established as a model for both the study of invasive brain cancer and systemic metastatic cancer (Huysentruyt et al. 2008; Huysentruyt et al. 2010). Therefore, the VM-M3 model is a valuable tool for the pre-clinical evaluation of potential anti-invasive and anti-metastatic therapies.

I hypothesized that due to the myeloid origin of the VM-M3 cell line, these tumor cells are highly dependent on glutamine for energy and survival. In addition, I hypothesized that phagocytosis may play a role in the survival of the VM-M3 cell line during energy stress. Therefore, I suggest that a diet/drug combination that specifically targets glucose, glutamine and phagocytosis is required to manage VM-M3 metastatic and invasive cancer. Due to the similar properties of the VM-M3 cell line to various other human metastatic tumors, I also suggest that the management of human metastatic cancer will rely on a similar therapeutic combination.

MATERIALS AND METHODS

Cell Lines

Tumor cell lines were prepared as described previously (Huysentruyt et al. 2008; Huysentruyt et al. 2010). Briefly, tumor tissue was removed from the mice and was transferred to a Petri dish containing Dulbecco's Modified Eagle medium (DMEM, Sigma, St. Louis, MO) with high glucose (25 mM) supplemented with 10% fetal bovine serum (FBS, Sigma) and 50 μg/ml penicillin-streptomycin (Sigma). The tumor tissue was minced thoroughly to obtain a cell suspension. 1 ml of the cell suspension was then seeded into a tissue culture flask containing DMEM (25mM glucose, 10%FBS). The VM tumor cells were evaluated after a minimum of eight passages to insure that the cells lines were uniformly homogeneous. The astrocyte C8-D30 (Astrocyte type III clone, AC) was purchased from American Type Culture Collection (Manassas, VA). The mouse astrocytoma CT-2A cell line was generated from the chemically induced tumor as previously described (Seyfried et al. 1992).

Cell Culture Conditions

The cell lines were grown in cell culture flasks (Corning, Inc., Corning, NY) in Dulbecco's Modified Eagle medium (DMEM, Sigma, St. Louis, MO) with high glucose (25 mM) supplemented with 10% fetal bovine serum (FBS, Sigma) and 50 μg/ml penicillin-streptomycin (Sigma) (complete DMEM). The cells were cultured in a CO_2 incubator with a humidified

atmosphere containing 95% air and 5% CO_2 at 37°C. At confluency, cells were removed from the flasks with a cell scraper and were passed to a new culture flask.

Transduction of Cell Lines

Transduction was performed as previously described (Huysentruyt et al. 2008). Briefly, the lentiviral vector CSCGW2-Fluc-IG was derived from CSCGW by deleting all promoter elements from the U3 region in the 3'LTR and inserting a firefly luciferase (Fluc)-IRES-EGFP cassette under control of the CMV promoter (gift from Miguel Sena-Esteves). Lentiviral vector stocks were produced with titers of $1x10^8$ tu/mL. One day prior to infection, approximately 100,000 cells were plated in a 6-well plate in DMEM. Infection was performed with a multiplicity of infection (MOI) of 100 in a total volume of 1.5 ml of DMEM. After 24 hr of incubation, 2.0 ml of fresh medium was added to the well. To obtain a clonal cell line, we passaged the cells 3 times and then sorted them into a 96-well plate based on EGFP expression using a MoFlo cell sorter (Dako, Carpinteria, CA).

ATP and VM-M3 cell number curve

For the ATP curve, varying concentrations of ATP were diluted in culture media and added to a 24 well plate. Both luciferase and luciferin were added and the plate was imaged for approximately 5 minutes on the Xenogen IVIS System as described below. For the cell number curve, varying cell numbers were seeded in culture media in a 24 well plate. The cells were then imaged on the Xenogen IVIS System for approximately 5

minutes.

Experimental Medias

DMEM powder (Sigma) was prepared as directed without the addition of glucose, glutamine or FBS. The pH of this media was adjusted to 7.4. This "minimal" media was then sterile filtered, supplemented with 50 μg/ml penicillin-streptomycin (Sigma) and stored at 4°C. Using this minimal media as a base, all other experimental medias were prepared. The pH of each experimental media was re-adjusted to 7.4 and was sterile filtered. Experimental medias include 25 mM glucose + 4 mM glutamine, 25 mM glucose (Sigma), 4 mM glutamine (Sigma), 4 mM glutamine + 1 mM hepanoic acid (Sigma), 25 mM glucose or 4 mM glutamine + 10mM β-hydroxybutyrate (Sigma), and various combinations of glucose and glutamine concentrations.

Metabolic Profiling

Approximately 5 x 10^4 cells were seeded into two 24 well plates in complete DMEM. 300 μg/ml of D-luciferin was added to the wells of one plate and the cells were imaged immediately on the Xenogen IVIS system for 3-5 minutes (Xenogen, Hopkington, MA) to record the bioluminescent signal from the cells. This reading was recorded as the 0 hr time point. After imaging, the cells were allowed to settle for 6-9 hrs before being rinsed with minimal media and incubated in the various experimental medias. For select experiments, these medias also contained various drugs to include 3 mM *meso*-Tartrate (Sigma), 2 mM 3-Nitropropionic acid (3NP, Sigma) and 175 μM Diadenosine

Pentaphosphate (Ap5A, Sigma). 24 hrs later the cells were imaged again on the Xenogen IVIS system for 3-5 minutes. The data is represented as the percent survival relative to the 0 hr time point. For select experiments, media aliquots were taken at each time point for lactate measurements. A drug toxicity curve was initially generated for all metabolic inhibitors as described below. The inhibitor dose chosen for each experiment yielded an approximate 40% reduction in cell number relative to the non-drug control. At this concentration, the inhibitor in complete media reduced cell growth but did not result in any cell death. This concentration was chosen in an effort to avoid potential non-specific toxicities.

Drug Toxicity Curves

Approximately 1 x 10^5 cells were seeded in 24-well plates and allowed to settle for 24 hrs. After 24 hrs some wells were imaged to obtain a 0 hr initial bioluminescent signal. The wells were then rinsed with minimal media and incubated in complete media plus the various drug concentrations (Sodium Phenybutyrate (PBA), Scandinavian Formulas, Sellersville, PA, 6-Diazo-5-oxo-L-norleucine (DON), Sigma). All drug stocks were prepared in complete media and sterile filtered. After a 24 hr incubation in the various drug medias, the cells were imaged for 3-5 minutes on the Xenogen IVIS system (Xenogen, Hopkington, MA) to record the bioluminescent signal from the cells. For extended experiments, the wells were incubated in fresh media + drug and incubated for an additional 24 hrs. Data is represented as the percent survival relative to the non-drug control at 24 hrs or as the percent survival relative to a 0 hr time point over 48 hrs.

Oligomycin Sensitivity

Approximately 1 x 10^5 VM-M3 or CT-2A cells were seeded in 24 well plates and allowed to settle for 24 hrs. After 24 hrs, the wells were rinsed with minimal media and incubated in various medias containing 5 ug/ul oligomycin (Sigma). An initial reading on the Xenogen IVIS system was obtained prior to the addition of oligomycin. The cells were incubated in the medias containing oligomycin over 2 hrs and then imaged again on the Xenogen imaging system. Media aliquots from the CT-2A experiment were taken for lactate measurements.

Matrigel™ Phagocytosis Assay

Approximately 5 x 10^5 cells were added to 200 μL growth factor reduced Matrigel™ Matrix (BD Biosciences) in a 1:2 ratio (v:v). The cell/matrix mixture was then divided among 6 wells of a 24 well plate. Additional wells were seeded for the 0 hr time point. The matrix was allowed to solidify at room temperature for 20 minutes before the addition of complete DMEM. Non-matrigel wells were seeded with approximately 8.3 x 10^4 cells. The cells with or without Matrigel were imaged on the Xenogen IVIS system (Xenogen, Hopkington, MA) to record the bioluminescent signal. This reading is recorded as the 0 hr time point. After imaging the cells were allowed to settle for 6-9 hrs in complete DMEM before being rinsed with minimal media and incubated in 5 mM glucose (VM-M3) or 0.8 mM glutamine (CT-2A) ± 20 μM chloroquine. The plate was then imaged again at 24 hrs. The data is represented as the percent survival relative to the

0 hr time point. Media aliquots were taken for lactate determinations.

Latex Bead Phagocytosis assay

Cell phagocytic capacity was determined by using a modification of a standard fluorometric assay (Oda and Maeda 1986). Fluoresbrite® YG carboxylate microspheres (1 μm diameter, Polysciences, Warrington, PA) were prepared in a gly-NaOH buffer as described below. Cells were seeded in 2-well Lab-Tek Chambered Coverglass Systems (Nunc, Rochester, NY) and were allowed to adhere in DMEM. The cells were then incubated with the beads for 1 hr and were rinsed with DMEM to remove excess beads. Phagocytosis of beads was detected by confocal microscopy (Leica DMI6000 inverted scope equipped with the Leica TCSSP5 confocal system, Wetzlar, Germany) and the cells were photographed using Lecia software.

Collagen Coated Latex Bead Phagocytosis Assay

Latex beads (Polysciences) were prepared as previously described (Naidu et al. 1988; Castellanos et al. 2000). Briefly 250 μL of beads were mixed with 750 μL gly-NaOH buffer (pH 8.2). This mixture was centrifuged for 5 min at 4500 x g. The bead pellet was then resuspended in 750 μL of fresh gly-Na0H buffer. This suspension was divided into 4 aliquots. The aliquots were incubated in the presence or absence 0.5 μg/μL of type VI collagen (Sigma) for 12 hrs at 30 °C on at horizontal shaker at 50 rpm. After 12 hrs the mixture was centrifuged for 5 min at 9200 x g at room temperature. The pellet was resuspended in 1 mL of PBS and stored at 4°C. For the cell assay, approximately 1 x 10^5

VM-M3 cells were seeded in 24 well plates. The cells were imaged on the Xenogen IVIS system (Xenogen, Hopkington, MA) to record the bioluminescent signal from the cells. This reading is recorded as the 0 hr time point. After imaging, the cells were allowed to settle for 6-9 hrs before being rinsed with minimal media and incubated in minimal media + 5 mM glucose with coated or non-coated latex beads. The plate was then imaged again 24 hrs later. The data is represented as the percent survival relative to the 0 hr time point. Media aliquots were taken for lactate and ammonia measurements.

Ketone Transition

Approximately 5 x 10^4 Astrocyte and VM-M3 cells were seeded into 24 well plates in complete media. Cells were allowed to settle for 6 hrs and the media was changed to 12.5 mM glucose, 2 mM glutamine ± 10 mM β-hydroxybutyrate (β-OHB, Sigma) for 48 hrs. After 48 hrs the cells were incubated in media that was diluted 1:1 with minimal media ± 10 mM β-OHB. After 24 hrs, the media was again diluted 1:1 with minimal media ± 10 mM β-OHB. After each 24 hr incubation the media was serially diluted until a final concentration of 0.39 mM glucose, 0.0625 mM glutamine ± 10 mM β-OHB. The cells were then incubated in 0 mM glucose, 0 mM glutamine ± 10 mM β-OHB for 24 hrs. The cells were then incubated in complete DMEM ± 10 mM β-OHB until the cells began to divide again. At this point, all VM-M3 cells had died, while the astrocytes began to divide. After a new population of cells was established, the astrocytes were transitioned again off of DMEM down to 0.39 mM glucose, 0.0625 mM glutamine ± 10 mM β-OHB.

Once a stable population was established cells were maintained in 3 mM glucose, 0.5 mM glutamine, and 10 mM β-OHB.

Ketone Determination

The ketone body β-hydroxybutyrate (β-OHB) was measured enzymatically in plasma or serum with a modification of the Williamson et al. procedure (Williamson et al. 1962).

Lactate Determination

Lactate was determined using the Lactate Assay Kit from the Biomedical Research Service Center at the University of Buffalo, NY.

Ammonia Determination

Ammonia was determined using an ammonia/glutamine Assay Kit from Megazyme (Bray, Ireland).

Proton NMR

VM-M3 cells were grown to approximately 80% confluency under normal culture conditions. The cells were then incubated in either 25 mM glucose + 4 mM glutamine, 25 mM glucose, or 4 mM glutamine for 12-24 hrs. Media aliquots were lyophilized and stored at -80°C until the time of analysis. Adherent cells were scraped and rinsed in PBS for a total of 3 times. They were spun down and lysed in 0.5 mL cold 70% ethanol. The lysate was then bath sonicated for 10 minutes and spun down for 5 min at 4,000 r.p.m.

The supernatant was collected and the resulting pellet was washed again in 70% ethanol for a total of 4 times. The resulting supernatant was frozen at -80°C and lyophilized. For ^{13}C labeling experiments, the cells were incubated in either [U] ^{13}C glutamine (Cambridge Isotope Laboratories, Inc, Andover, MA) or [U] ^{13}C glutamine + unlabeled 25 mM glucose for 12 hrs and the cell lysates and media were collected as described above.

Mice

Mice of the VM/Dk (VM) strain were obtained as gifts from G. Carlson (McLaughlin Research Institute, Great Falls, Montana) and from H. Fraser (University of Edinburgh, Scotland). All Mice used in this study were housed and bred in the Boston College Animal Care Facility using husbandry conditions as previously described (Ranes et al. 2001). All animal procedures were in strict accordance with the NIH Guide for the Care and Use of Laboratory Animals and were approved by the Institutional Animal Care Committee.

Origin of VM tumors

The VM-NM1 and the VM-M3 tumors arose spontaneously in the cerebrum of adult VM mice as described previously (Huysentruyt et al. 2008). The tumors were detected during routine examination of the VM mouse colony over a period of several years (1993-2000). The tumors were grossly identified in the cerebrum as poorly defined masses (about 3 x 1 x 1 mm) similar to those described previously for other spontaneous tumors in the VM mouse brain (Fraser 1986b;

El-Abbadi et al. 2001). In order to preserve *in vivo* viability, each tumor was immediately resected and implanted intracerebrally (i.c.) into host VM mice as described below. As soon as cranial domes appeared, the tumors were passaged again into several host VM mice. After a total of three i.c. passages, the tumors were grown subcutaneously (s.c.) and cell lines were prepared from each tumor as described above. All cell lines were cultured under identical conditions to reduce environmental variability.

Intracranial Implants

Tumor implantation was performed as previously described (Ranes et al. 2001). Briefly mice are anaesthetized with Avertin (0.1mL/10g). The tops of the heads are disinfected with ethanol and a small incision is made in the scalp of the mouse over the midline. A $3mm^3$ burr hole is made in the skull over the right parietal region behind the coronal suture and lateral to the sagital suture. Using a trocar, a small ($1mm^3$) tumor fragment is implanted into the hole made in the skull. The flaps of skin are then immediately closed with collodion. Additionally, some implants were performed using approximately 1-2 x 10^4 cells in 5μL PBS. The cells were injected into the right cerebral hemisphere using a Hamilton syringe. All tumor-implanted mice reached morbidity at approximately 12-15 days regardless of implant method. Both methods result in the implantation of tumor fragments or tumor cells approximately 1.5-2 mm deep into the cortical region as previously described (Shapiro et al. 1970). Tumor cells are also highly invasive regardless of implant method. The mice were placed in a warm room (37°C) until they were fully recovered.

Subcutaneous Implants

For s.c. implantation, VM mice were anaesthetized with Isoflurane (Halocarbon, River Edge, NJ), and the tumor was implanted by a s.c. injection of 0.1 ml of small tumor pieces suspended in 0.2 ml PBS by use of a 1 cc tuberculin syringe attached to an 18-gauge needle into the right flank. All mice recovered from their surgical procedure and were returned to their cages when they became fully active.

Bioluminescent Imaging

The Xenogen IVIS system (Xenogen, Hopkington, MA) was used to record the bioluminescent signal from the luciferase labeled tumors as described previously (Huysentruyt et al. 2008). For *in vivo* imaging, mice received an intraperitoneal injection of D-Lucifierin (50 mg/kg, Xenogen) and Avertin (0.1 mL/10g). Imaging times ranged from 30 sec to 15 min, depending on the time point. For *ex vivo* imaging, organs were entirely removed and rinsed in PBS. Organs were imaged in 300 μg/ml D-luciferin in PBS from 1-6 min. For i.c. studies, brains were removed and split down the midline. Individual hemispheres were imaged separately in 300 μg/ml D-luciferin in PBS, and imaged from 1-15 min. For the analysis of distal tumor spread, each hemisphere was further dissected into the cerebellum, brain stem, cortex, and hippocampus and imaged in an additional 300 μg/ml D-luciferin in PBS. Right and left hemisphere brain regions were imaged separately.

Dietary/Drug Regimens, Body Weight, and Food Intake Measurements

Adult male and female VM mice of approximately 60-90 days old were separated into individual housing 1-2 days before tumor implantation. Individually housed mice were kept in plastic cages with filter tops containing Sani-Chip bedding (P.J. Murphy Forest Products Corp., Montville, NJ). Body weights and food intake measurements were recorded daily and food was provided *ad libitum*. Tumor fragments were implanted on day zero. The mice were then separated into groups matched for body weights 4-7 days post implantation after imaging on the Xenogen Imaging System to confirm the presence of a tumor. For the duration of the study, mice on calorie restriction received 40% of their normal food intake at approximately 10 AM (60% CR). The AL control mice continued to receive food *ad libitum.* All mice were weighed daily prior to food administration. For those mice that received drug injections, a fresh stock was prepared and diluted to an appropriate concentration in PBS. Drug was administered intra-peritoneally (i.p.). Drug was stored at 4°C for the duration of the study. Mice were dosed at approximately 10 AM daily unless indicated otherwise. For DON studies, mice received daily injections of either 1.0 mg/kg or 0.5 mg/kg. Mice in the DON survival study received DON at either 1.0 mg/kg/day or 0.5 mg/kg/day depending on individual mouse response. Some doses were skipped if the mice appeared lethargic or if body weight loss exceeded 1.5 g from the previous day. For chloroquine (Sigma) studies, mice received daily injections of 45 mg/kg. Studies were terminated at the time of morbidity for the control group.

Plasma and Serum Glucose Measurements

Mice were anesthetized with isoflurane and euthanized by exsanguination, involving collection of blood from the heart as previously described (Marsh et al. 2008a) or from the carotid artery via decapitation. The blood was centrifuged at 4,000 x *g* for 20 min, the plasma or serum supernatant was collected were stored at –80°C before analysis. Blood glucose was measured in a spectrophotometer using the appropriate enzymatic assay (Stanbio Laboratories).

Histology

Brain tumor samples were fixed in 10% neutral buffered formalin (Sigma) and embedded in paraffin. The brain-tumor samples were sectioned at 5 μm, were stained with haematoxylin and eosin (H & E) at the Harvard University Rodent Histopathology Core Facility (Boston, MA), and were examined by light microscopy using either a Zeiss Axioplan 2 or Nikon SMZ1500 light microscope as we previously described (Mukherjee et al. 2002). Images were acquired using SPOT Imaging Solutions (Diagnostic Instruments, Inc) cameras and software. All histological sections were evaluated by a veterinary neuropathologist, (Roderick Bronson) at the Harvard University Rodent Histopathology Core Facility.

PCR

All cell lines were grown under identical conditions as described above. VM brain and VM-M3 tumor samples were frozen at -80°C until time of analysis. Single strand cDNA was synthesized from total RNA and used for PCR amplification as we previously described (Abate et al. 2006). Primer sequences used for PCR were for β-actin, forward 5′-TGTGATGGTGGGAATGGGTCAG-3′ and reverse 5′

TTTGATGTCACGCACGATTTCC-3′; for IGFBP-2, forward 5′-GGGTACCTGTGAAAAGAGACG-3′ and reverse 5′-TGCAGGGAGTAGAGATGTTCC-3′; for CXCR4, forward 5′-CTACAGCAGCGTTCTCATCC-3′ and reverse 5′-GGATGACTGTCGTCTTGAGG -3′. Primers were optimized for annealing temperatures and cycle numbers as previously described (Abate et al. 2006). RT-PCR products were separated on a 1-1.6% agarose gel containing ethidium bromide and visualized by UV light. RT-PCR was performed on the total RNA of each sample in the absence of reverse transcriptase to control for possible DNA contamination.

Immunohistochemistry and Confocal Microscopy

Cells in culture were maintained as described above. Cells were seeded in glass-chambered slides in complete DMEM (Sigma) media. After 24 hours cells were stimulated with 100 ng/ml of CXCL-12 (SDF-1) in serum free media for 30 minutes. Cells were washed and fixed with 4% formaldehyde for 20 minutes at 37^{o}C. After blocking with 10% goat serum in 0.1% BSA, cells were incubated with CXCR4 primary antibody (1:100) for 1 hour followed by secondary antibody (1:100) incubation for 1 hour at room temperature. Cells were washed and stained with Hoechst for 10 minutes and mounted. Corresponding wells without primary antibody served as negative controls.

For the immunohistochemical studies, the tissue sections from untreated tumor bearing mice were deparaffinized, rehydrated and washed. The tissue sections were then heat

treated (95°C) in antigen unmasking solution (Vector Laboratories, Burlingame, CA) for 30 min. Tissue sections were blocked in goat serum (1:10 in PBS) for one hour at room temperature, treated with CXCR4 primary antibody (rabbit polyclonal, 1:200 SantaCruz) in blocking buffer for one hour at room temperature, followed by alexafluor 585 conjugated anti-rabbit secondary (Invitrogen) at 1:200 dilution for 45 minutes. Sections were incubated with Hoechst (10μg/ml) for 10 minutes and mounted. Corresponding tissue sections without primary antibody served as negative controls. For confocal microscopy, digital images were obtained on a Leica DMI6000 inverted scope equipped with the Leica TCSSP5 confocal system, using HCX PL APO 40X/1.25 NA oil and HCX PL APO 63X/1.4 NA oil objective lenses. Leica confocal software was used to acquire images.

For Ki-67 staining, tissue slides were processed similarly as for CXCR4 and then treated with Ki-67 primary antibody (rat monoclonal, Dako, 1;100) overnight at 4°C followed by a biotinylated anti-rat secondary antibody at 1:100 dilution (Vector laboratories, Inc). The sections were then treated with avidin biotin complex followed by 3,3'-diaminobenzidine as substrate for staining according to the manufacturer's protocol (Vectastain Elite ABC kit, Vector laboratories, Inc.). The sections were counter stained with haematoxylin and mounted. Corresponding tissue sections without primary antibody served as negative controls. Bright field images were captured by a Zeiss Axioplan 2 light microscope. The percent of Ki-67 positive cells were determined using a photoshop-based image analysis as described previously (Lehr et al. 1999).

RESULTS

The goal of this research was to develop a model for the study of malignant brain tumor growth and invasion. Additionally, I sought to evaluate our VM-M3 cells for metabolic alterations that could lead to the development of a metabolic therapy.

Comparison of invasive versus non-invasive brain tumors

Figure 1 shows the gross histological phenotype of the non-invasive C57BL/6 CT-2A astrocytoma model and the VM-M3 brain tumor model. The CT-2A tumor showed a sharp border with minimal local invasion and no distant invasion consistent with its previously reported behavior (Martinez-Murillo and Martinez 2007). In contrast, the VM-M3 tumor showed a diffuse border with several secondary focal lesions within the brain parenchyma as well as in the contralateral hemisphere.

Quantitative assessment of tumor growth

We used the luciferase labeled VM-M3 tumor and monitored tumor growth non-invasively over time (Figure 2). The bioluminescent signal could be evaluated both qualitatively (Figure 2A), and quantitatively (Figure 2B) during tumor progression. Bioluminescence, above the lower limit of the imaging system (~ $1x10^3$ photons/sec), could be detected as early as day 6.

Detection and quantitation of VM-M3 invading tumor cells

In order to quantitate the level of tumor invasion, the brains were removed at the end of the study and imaged *ex vivo* as described in Materials and Methods. The brains were sectioned down the midline and each half was imaged separately. As shown in Figure 3A, bioluminescence was detected in both the ipsilateral and the contralateral hemispheres. The level of invasion into the contralateral hemisphere was also quantitated. In addition, histology was used to confirm the presence of invading tumor cells in both the ipsilateral and contralateral hemispheres (Figure 3B).

Quantitation of distal tumor spread

In order to further evaluate the invasion of the VM-M3 tumor cells, the removed brains were dissected into the cortex, hippocampus (Figure 4), brain stem, and cerebellum (Figure 6). Using the Xenogen Imaging System, bioluminescence was detected and quantitated in all of the brain regions. Histology was used to confirm the presence of invading tumor cells in the corresponding regions (Figure 5 and 7).

Migratory routes of invading tumor cells

We next identified the routes of VM-M3 tumor cell invasion (Figure 8). We identified surface or sub-pial spread as the major route of invasion (Figure 8A). However, we also identified tumor cells invading along and within white matter tracts, such as the corpus callosum and along myelinated axons crossing through the striatum (Figure 8B, C), through the ventricular space (Figure 8D), along blood vessels (Figure 8D) and along neurons (Figure 8F).

Expression of CXCR4 and IGFBP-2 in brain, tumor tissue, and cultured tumor cells

As shown in Figure 9, the VM-M3 tumor cells both *in vivo* and *in vitro* expressed high levels of CXCR4, a chemokine receptor highly expressed in human GBM. In addition, the less invasive VM-NM1 tumor from the same VM mouse host had very low CXCR4 gene expression. Also, we showed that insulin-like growth factor binding protein 2 (IGFBP-2) was not highly expressed in the invasive VM-M3 cells whereas the less invasive VM-NM1 tumor cells had high expression of IGFBP-2. We also found that CXCR4 was localized to the surface of the VM-M3 tumor cells that were grown either *in vivo* or *in vitro* (Figure 10). Additionally, CXCR4 expression was found in the cells that had invaded throughout the brain via the sub-pial space, white matter tracts, and blood vessels (Figure 11).

Ki-67 expression in VM-M3 tumors

As shown in Figure 12, the VM-M3 tumors stain positive for the proliferation marker Ki-67, indicating a high proliferation rate of these cells *in vivo.* Ki-67 is a protein highly expressed during all phases of cell proliferation, though its specific function is largely unknown (Scholzen and Gerdes 2000). High Ki-67 expression was seen in tumor cells in the tumor core as well as in invasive tumor cells found within the brain parenchyma (Figure 12). Invasive cells staining positive for Ki-67 include those cells migrating through the pial membrane (Figure 12B), along blood vessels (Figure 12B, arrow),

through white matter tracts such as the corpus callosum (CC) (Figure 12C, arrow) and into the brain parenchyma (Figure 12D, arrow).

Effect of calorie restriction on body weights, plasma glucose and ketones

I next evaluated the effect of calorie restriction on body weights and circulating levels of glucose and ketones. Calorically restricted mice received a 60% restriction in food intake as described in Materials and Methods (Figure 13). Calorie restriction significantly reduced the body weights of the mice over the course of the study (Figure 14A). In addition, circulating glucose levels were significantly lower (Figure 14B), while circulating ketone levels were significantly increased (Figure 14C), in the CR group compared to the control *ad libitum* (AL) fed group.

Effect of calorie restriction on tumor growth and invasion

As seen in Figure 15, calorie restriction reduced the growth and invasion of the VM-M3 primary tumor in mice under CR. Compared to the diffuse, ill-defined border of the tumor of the AL control group, the tumor of the CR group was denser with a more defined border. I evaluated the level of invasion into the contralateral hemisphere using bioluminescent imaging as described in the Materials and Methods. I showed that the total amount of bioluminescence in the contralateral hemisphere of the CR group compared to the amount of bioluminescence in the contralateral hemisphere of the AL group was significantly reduced (Figure 16). Histology was used to confirm the extent of tumor cell invasion into the contralateral hemisphere between the AL and CR groups. As

shown in Figure 17, invading tumor cells were identified in all regions of the contralateral hemisphere of the AL group. In contrast, we only identified sub-pial spread to the cortex in the contralateral hemisphere of the CR group. The number of migrating cells was also noticeably less in the CR mice than in the AL mice (Figure 17). In addition, as shown in Figure 18, the percentage of Ki-67 (+) tumor cells was significantly reduced in the CR group compared to the AL control group.

The VM-M3 tumor as a model for systemic metastatic cancer

As shown in Figure 19, the VM-M3 tumor is metastatic to all organs when implanted subcutaneously. Tumor spread can be evaluated over time non-invasively both qualitatively (Figure 19A), and quantitatively (Figure 19B). In addition, *ex vivo* imaging of the organs allows for a more specific assessment of tumor spread (Figure 19C).

Effect of calorie restriction on body weights, plasma glucose and ketones

I next evaluated the effect of calorie restriction on body weights and circulating plasma glucose and ketones in mice implanted subcutaneously with the VM-M3 tumor. Calorically restricted mice received about 40% of their normal food intake (60% CR) as described in Materials and Methods (Figure 20). Calorie restriction significantly reduced the body weights of the calorically restricted (CR) group over the course of the study (Figure 21A). In addition, CR significantly reduced circulating plasma glucose (Figure 21B) and significantly increased circulating plasma ketones (Figure 21C) in the CR group compared to the *ad libitum* (AL) fed group.

Effect of calorie restriction on tumor growth and metastasis

As shown in Figure 22, primary tumor growth was significantly lower in the CR group than in the AL group. However, metastatic spread was not statistically different between the control and CR group for any organ (Figure 23). The incidence of metastatic spread to each organ was also not significantly different (Table 1).

Differential response to energy stress between CT-2A and VM-M3 cell lines in vitro

In order to assess the metabolic requirements of the VM-M3 cell line, a bioluminescent-based cell viability assay was developed as described in the Materials and Methods to test the ability of the cells to survive under extreme energy stress in serum free media in the absence of either glucose or glutamine. As shown in Figure 24, the CT-2A astrocytoma cell line, which has previously been shown to respond to calorie restriction, is primarily glycolytic and uses glucose (gluc) as its preferred fuel. However, the VM-M3 cell line, which is less responsive to calorie restriction, is more dependent on glutamine (gln) than glucose (gluc) for energy and survival. Because bioluminescence is directly correlated to ATP concentration (Supplemental Figure 5A), I show that glutamine is better able to support ATP production than is glucose in the VM-M3 cells.

VM-M3 lactate production under energy stress

Though lactate traditionally serves as an indicator of glycolytic flux, glutaminolysis can also result in the production of lactate. As shown in Figure 25, very little lactate was

generated from a 24 hour incubation in glutamine. In contrast, a significantly larger amount of lactate was generated from the cells incubated in glucose. However, as shown previously in Figure 24, cell viability was significantly lower in glucose than in glutamine, indicating that VM-M3 cell survival in glutamine is independent of glycolysis or lactate production.

VM-M3 cell survival in both glucose and glutamine

In order to determine if glucose and glutamine act synergistically to promote cell survival in the VM-M3 cell line, the two metabolites were tested together in culture (Figure 26). Cell viability and hence ATP production was significantly enhanced relative to viability in either metabolite alone. In addition, the production of lactic acid was enhanced when the two metabolites were combined (Figure 27), suggesting that glycolysis and glutaminolysis acted synergistically to maintain cell viability and growth.

Survival of VM-M3 cells in varying glucose and glutamine concentrations

VM-M3 cells were incubated in varying concentrations of glucose and glutamine. As shown in Figure 28, when the glucose concentration was held constant while reducing the glutamine concentration, a corresponding reduction in cell viability was observed. However, when the glutamine concentration was held constant, we see that only small amounts of glucose were necessary to maintain a constant level of cell viability. This again suggests that the VM-M3 cells rely more on glutamine than glucose for energy and cell survival.

Effect of meso-Tartrate on VM-M3 cell viability

Meso-Tartrate, a malate analog, is an inhibitor of malic enzyme (Supplemental Figure 3) (Do Nascimento et al. 1975). Current hypotheses suggest that cytosolic malic enzyme is responsible for generating pyruvate from glutamine-derived malate (DeBerardinis et al. 2007). *Meso*-Tartrate had little effect on glutamine metabolism (Figure 29). Interestingly, *meso*-Tartrate had a significant effect on cell viability when in the presence of both glucose and glutamine, suggesting that *meso*-Tartrate is potentially inhibiting glycolysis. In support of this, lactic acid was significantly reduced when the VM-M3 cells were incubated in both glucose and glutamine in the presence of *meso*-Tartrate (Figure 30). Additionally, there was no reduction in lactate production when the VM-M3 cells were incubated in glutamine and *meso*-Tartrate (Figure 30).

Effect of the TCA cycle inhibitor 3-Nitropropionic acid (3-NP) on VM-M3 cell viability

I next sought to determine the effect of the TCA cycle inhibitor 3-NP on VM-M3 cell viability and ATP production while under energy stress (Supplemental Figure 3). As shown in Figure 31, 3-NP caused a significant reduction in cell viability when the cells were in media containing glutamine. Incubation of VM-M3 cells in glucose alone with 3-NP had only a slight effect on cell viability. Therefore this suggests that 3-NP is specific to glutamine metabolism and that the VM-M3 cells generate a significant amount of ATP from glutamine.

Effect of fatty acid metabolism on VM-M3 cell viability

Because a large amount of lactic acid is generated from glucose derived pyruvate, an additional source of acetyl-CoA would be necessary for continued TCA cycling and glutamine metabolism. As shown in Figure 32, the addition of heptanoic acid, a short chain fatty acid, significantly enhanced VM-M3 survival when in the presence of glutamine. Thus acetyl-CoA can continually feed in to the TCA allowing for glutamine metabolism to maintain cell viability and ATP production.

Effect of ketones on VM-M3 cell viability in vitro

As shown in Figure 33, the addition of 10mM β-hydroxybutyrate was not toxic to the VM-M3 cells. The presence of β-hydroxybutyrate was however slightly but significantly inhibitory in the presence of glutamine alone.

Oligomycin sensitivity of VM-M3 and CT-2A tumor cell lines

As shown in Figure 34, both the VM-M3 and CT-2A cell lines were able to maintain a sufficient level of ATP over 2 hours in media containing 5ug/ul oligomycin, the F1-ATPase inhibitor (Supplemental Figure 3). A short incubation time was used to eliminate non-specific toxicity as described previously (Matheson et al. 2007). In addition, after 1 hour in oligomycin, the CT-2A cells had a lower amount of ATP compared to the controls, but produced significantly more lactic acid, consistent with the upregulation of glycolysis in response to an inhibition of respiration (Figure 35). This suggests that in

both CT-2A and VM-M3 cell lines, metabolism of glucose and glutamine occurs respectively in the absence of a functional respiratory capacity.

Effect of diadenosine pentaphosphate (Ap5A) on VM-M3 cell viability

As shown in Figure 36, incubation of the VM-M3 cells with the adenylate kinase inhibitor Ap5A resulted in a significant reduction in cell viability when glutamine was the only metabolite present. There was no significant effect of Ap5A on the VM-M3 cells in either gluc + gln or gluc alone. This suggests that ATP generated from glutamine in the mitochondria is heavily dependent on efficient phosphate transfer reactions particularly in the absence of cytosolic ATP.

In vitro effect of 6-Diazo-5-oxo-L-norleucine (DON) on the VM-M3 cell line

As shown in Figure 37, DON was effective in inhibiting cell growth over 48 hours at both low (50 μM) and high (250 μM) concentrations. Over the first 24 hours DON did not cause cell death but rather inhibited cell growth compared to the non-drug control. A slight reduction in cell viability was observed over 48 hours.

Effect of DON and DON + CR on body weights, blood glucose and ketones

I next evaluated the effect of DON alone and in conjunction with calorie restriction on body weights and blood glucose levels in mice implanted subcutaneously with the VM-M3 tumor. DON was administered beginning on day 5 at an initial dose of 1 mg/kg/day (Figure 38). Over the course of the study, dosing was adjusted based on individual

mouse response as described in Materials and Methods. As shown in Figure 39A, the body weights of DON treated mice were similar during drug treatment compared to the control mice. However, the body weights of DON treated mice declined over the last 3 days of the study. The DON + CR mice showed a steady decrease in body weight which was maintained over the last 2 days of the study. As shown in Figure 39B, blood glucose levels were similar between the DON group and control group, though blood glucose levels were significantly lower in the DON + CR group compared to the control or DON group. In addition, circulating blood ketones were elevated in the DON + CR group compared to the DON group (Figure 39C).

Effect of DON and DON + CR on tumor growth and metastasis

As shown in Figure 40, the removed tumors from both DON treated groups were significantly smaller compared to the control mice. The control mice had an average tumor weight of approximately 2.0 g. However, both DON treated groups had an average tumor weight of 0.1 g, nearly 20-fold less than the control mice. As seen in Figure 41, the control mice had tumor metastasis to the liver, lung, kidney, and spleen, consistent with the behavior of this tumor (Huysentruyt et al. 2008). However, both DON treated groups had no detectable metastasis to the liver, lung, or kidney. In addition, I examined liver histology because it is an organ most heavily infiltrated with tumor cells from the control group and is found in 100% of the control mice. As shown in Figure 42, histological analysis confirmed the lack of tumor cells in the liver of the DON and DON + CR treated mice in comparison to the control AL non-treated mouse

group. Interestingly, both DON treated groups did have metastasis to the spleen. Spleen bioluminescence was not significantly different between the control and either DON treated groups. However, using a chi square analysis, the incidence of metastasis to spleen was significantly lower in the DON + CR group than in the untreated controls (Table 2).

Effect of DON and DON + CR on mouse survival

As seen in Figure 43, all control mice reached morbidity 15-19 days post implantation. However, mice in the DON and DON + CR groups survived significantly longer. The DON treated group reached morbidity due to extreme drug toxicity as indicated by loss of body weight, hind leg paralysis, and urinary blockages. The primary tumors in the DON treated mice remained small and systemic metastasis detected with bioluminescent imaging was not apparent (data not shown). The DON + CR group however survived longer without any signs of toxicity. However, drug toxicity did eventually become apparent in the DON + CR group as well.

The aim of this last section was to determine if the VM-M3 cells were capable of generating ATP from the digestion of phagocytosed material and if this occurred primarily while under energy stress. Finally, the goal was to determine if this phagocytic property could be exploited for therapeutic options.

Effect of cholorquine (CQ) on CT-2A and VM-M3 cell viability in vitro

As shown in Figure 44, chloroquine, the lysosomal enzyme inhibitor, had no inhibitory effect on CT-2A cells grown in culture and may have been stimulatory at low concentrations. However, CQ did display a dose dependent toxicity toward the VM-M3 cells in culture over 24 hours.

Effect of chloroquine on VM-M3 cell viability in a Matrigel™ Matrix

In order to test the phagocytic capabilities of the VM-M3 cells, I developed an assay within a 3-dimensional Matrigel™ matrix. As shown in Figure 45A, over 24 hours 20μM chloroquine caused a slight reduction in VM-M3 cell viability in complete media and no significant reduction in VM-M3 cell viability in Matrigel™ plus complete media. Additionally, as shown in Figure 45B, VM-M3 cell viability was significantly reduced when grown in a glucose media in the absence of glutamine or FBS. The presence of Matrigel™ however significantly increased VM-M3 cell viability (Figure 46). In addition, chloroquine caused significant cell death in the VM-M3 cells when under energy stress either in the presence or absence of Matrigel™. This indicated that these cells were potentially capable of generating energy from phagocytosed components only while under energy stress. In support of this, as shown in Figure 47, the cells incubated in glucose + Matrigel™ generated significantly more lactic acid in the media than those cells in glucose alone, indicating that components of the carbohydrate rich Matrigel™ matrix were being used via glycolysis to generate energy.

Effect of chloroquine on CT-2A cell viability in a Matrigel™ Matrix

Similar to the VM-M3 cells, over 24 hours 20μM chloroquine did not cause a significant reduction in CT-2A cell viability in complete media or in Matrigel™ plus complete media (Figure 48A). Additionally, as shown in Figure 48B, CT-2A cell viability was significantly reduced when the cells were grown in a media containing only glutamine. Unlike VM-M3 cells, the presence of Matrigel™ did not rescue the CT-2A cells when placed under energy stress in a media containing only glutamine (Figure 49). In addition, chloroquine had no effect on CT-2A cell survival while under energy stress. This indicated that the CT-2A cells differed from the VM-M3 cells in that they were unable to use phagocytosis as a mechanism to acquire nutrients during times of energy stress.

Latex bead phagocytosis

As shown in Figure 50 using confocal microscopy, the VM-M3 cells phagocytosed un-opsinized latex beads. Additionally, when placed under energy stress, the VM-M3 cells internalized collagen coated latex beads resulting in a significant increase in survival relative to a non-coated latex bead control (Figure 51). However, as shown in Figure 52, the presence of collagen coated latex beads did not result in an increase in either lactate or ammonia accumulation in the media compared to the uncoated controls.

Effect of chloroquine on tumor growth and metastasis

I next evaluated the effect of chloroquine in conjunction with calorie restriction on VM-M3 tumor growth and metastasis (Figure 53). As shown in Figure 54, CQ had a slight but not significant inhibitory effect on the size of the primary tumor in mice treated with

CQ only compared to the controls. However, as seen in Figure 55, CQ treatment had no effect on metastasis. As seen in Figure 56, the combination of CR and CQ did not act synergistically and no further reduction in primary tumor wet weight was observed compared to the CR group. Additionally, as seen in Figure 57, the combination of CR and CQ did not have any inhibitory effect on metastatic spread compared to either the control or the CR group.

Effect of Chloroquine on brain tumor growth and invasion

Chloroquine in conjunction with calorie restriction was also evaluated on VM-M3 brain tumor growth and invasion (Figure 58). As shown in Figure 59, CQ had no effect on brain tumor growth or invasion in mice treated with CQ alone compared to the controls. Additionally, as seen in Figure 60, the combination of CR and CQ did not act synergistically and no further reduction in tumor invasion was observed compared to the CR group.

Astrocyte transition to a low glucose, high ketone media in vitro

As shown in Supplemental Figure 1, *in vitro,* astrocytes successfully transitioned to a high ketone, low glucose media. VM-M3 cells were unable to transition and no cell survival was apparent compared to the astrocytes.

Effect of phenylbutyrate (PBA) on VM-M3 survival in vitro

As shown in Supplemental Figure 2, PBA showed a does dependent effect on VM-M3 cell survival compared to the non-drug treated controls.

Correlation between ATP concentration, cell number and bioluminescence

As shown in Supplemental Figure 5, quantitation of bioluminescence can be directly correlated to both ATP concentration (Supplemental Figure 5A) and cell number (Supplemental Figure 5B).

Figure 1. Comparative analysis of the growth behavior of mouse brain tumors, VM-M3 and the CT-2A malignant astrocytoma. Small tissue fragments from the CT-2A and VM-M3 tumors were implanted into the right cerebral hemisphere (i.c.) of their syngeneic host C57BL/6J and VM strains, respectively. Brains were removed approximately 11-15 days post implantation and were stained with haematoxylin and eosin (H & E) as described in Materials and Methods. The CT-2A tumor shows a distinct tumor border with little local invasion and no distant invasion. The VM-M3 tumor is highly invasive both locally and distally with numerous secondary tumor lesions (arrows). Images are shown at 7.5x.

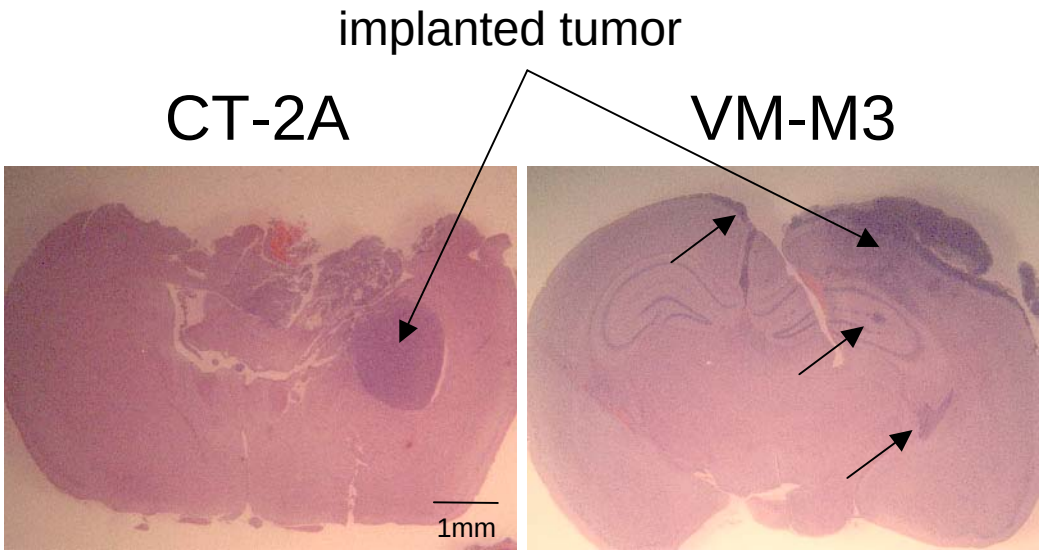
implanted tumor
CT-2A
VM-M3
1mm

Figure 2. Growth of the VM-M3/Fluc tumor with bioluminescence imaging. (**A)** VM-M3/Fluc tumor fragments were implanted as described in Figure 1. Cranial images were taken over 15 days (representative mouse shown). (**B)** Bioluminescence from the whole mouse was quantified and plotted on a log scale. All values are expressed as the mean of 6 independent samples ± SEM.

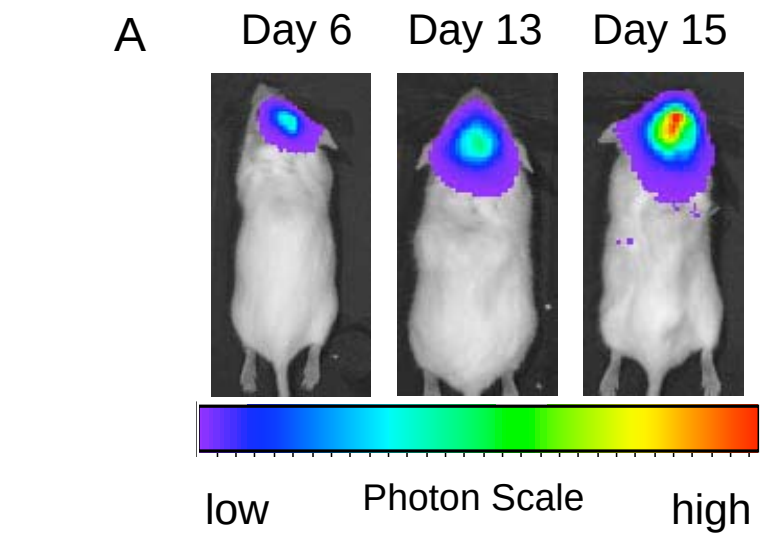
A
Day 6
Day 13
Day 15
low
Photon Scale
high

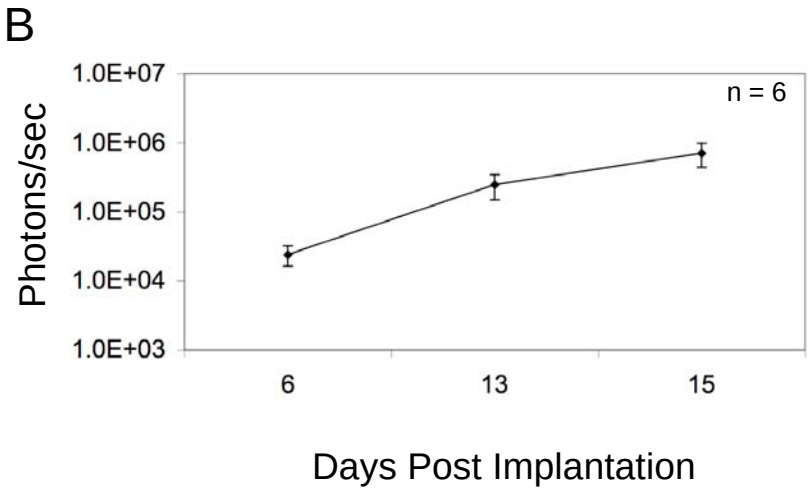
B
Photons/sec
1.0E+07
1.0E+06
1.0E+05
1.0E+04
1.0E+03
n = 6
6
13
15
Days Post Implantation

Figure 3. Detection of VM-M3/Fluc tumor cell invasion into the contralateral hemisphere with bioluminescent imaging and histology. (**A**) VM-M3/Fluc tumor fragments were implanted as described in Figure 1. Removed brains were dissected into ipsilateral and contralateral hemispheres. Each hemisphere was imaged for bioluminescence *ex vivo* as described in Materials and Methods. Bioluminescence from each brain half was quantified and plotted on a log scale. Bioluminescence in the contralateral hemisphere is indicative of distal tumor spread. The values are expressed as means ± SEM of six independent tumor-bearing mice. (**B**) Histological analysis (H&E) was used to validate the presence of tumor cells in the contralateral hemisphere as described in Materials and Methods. Tumor cells are shown in the contralateral hemisphere invading the neural parenchyma from the sub pial membrane (arrows). Images are shown at 200X.

A

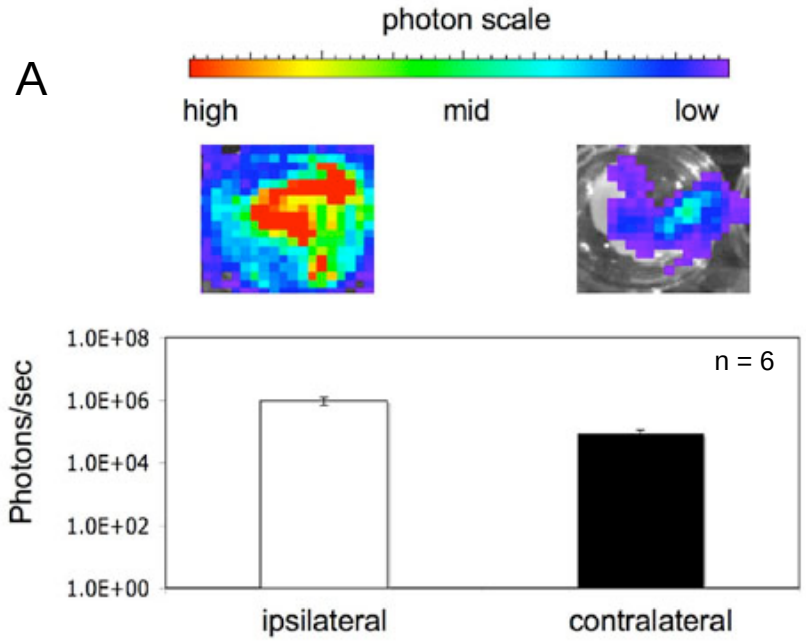
photon scale
high
mid
low
Photons/sec
1.0E+08
1.0E+06
1.0E+04
1.0E+02
1.0E+00
n = 6
ipsilateral
contralateral

B

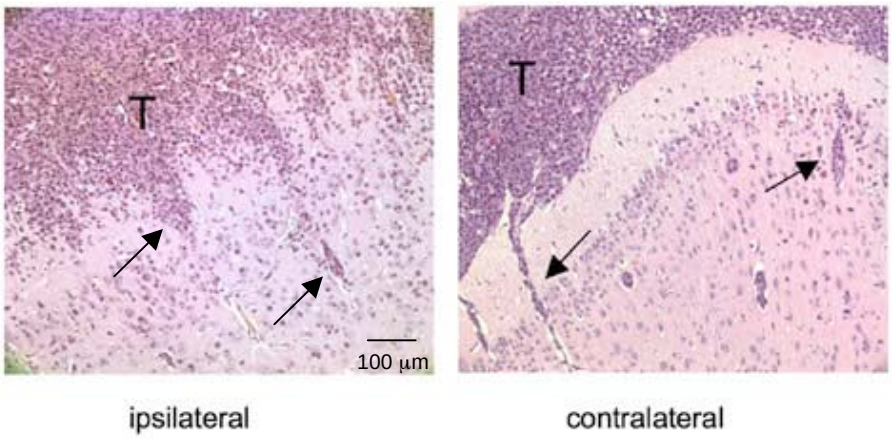
T
100 μm
T
ipsilateral
contralateral

Figure 4. Bioluminescent analysis of distal tumor spread to the cortex and hippocampus. VM-M3/Fluc tumor fragments or cells were implanted as described in Figure 1. Removed brains were sectioned through the midline and were further dissected into the cortex and hippocampus of the ipsilateral (I) and contralateral (C) hemispheres. Bioluminescence was quantified and plotted on a log scale. All values are expressed as the mean ± SEM of 10 independent samples.

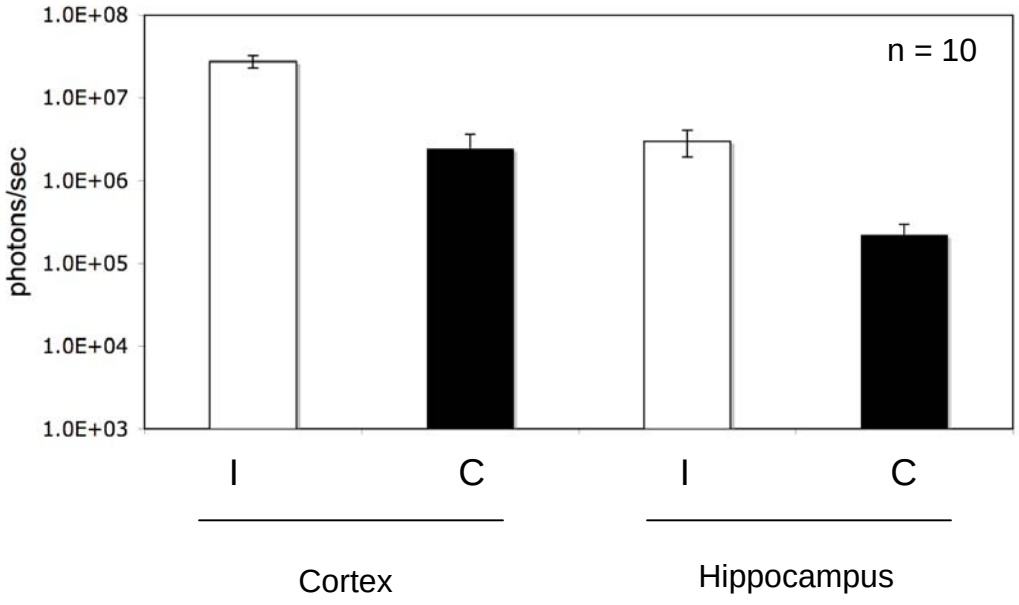
1.0E+08
1.0E+07
1.0E+06
1.0E+05
1.0E+04
1.0E+03
photons/sec
n = 10
I
C
I
C
Cortex
Hippocampus

Figure 5. Histological evaluation of distal tumor spread to the cortex and hippocampus. VM-M3/Fluc tumor fragments or cells were implanted as described in Figure 1. Histological analysis (H&E) was used to validate the presence of tumor cells as described in Materials and Methods. Top panel images are shown from left to right at 100X, 50X, 50X, and 100X. The black boxes from the top panel images are shown in higher power in the bottom panel. Bottom panel images are shown from left to right at 400X, 200X, 200X, and 400X. Arrows indicate invasive tumor cells.

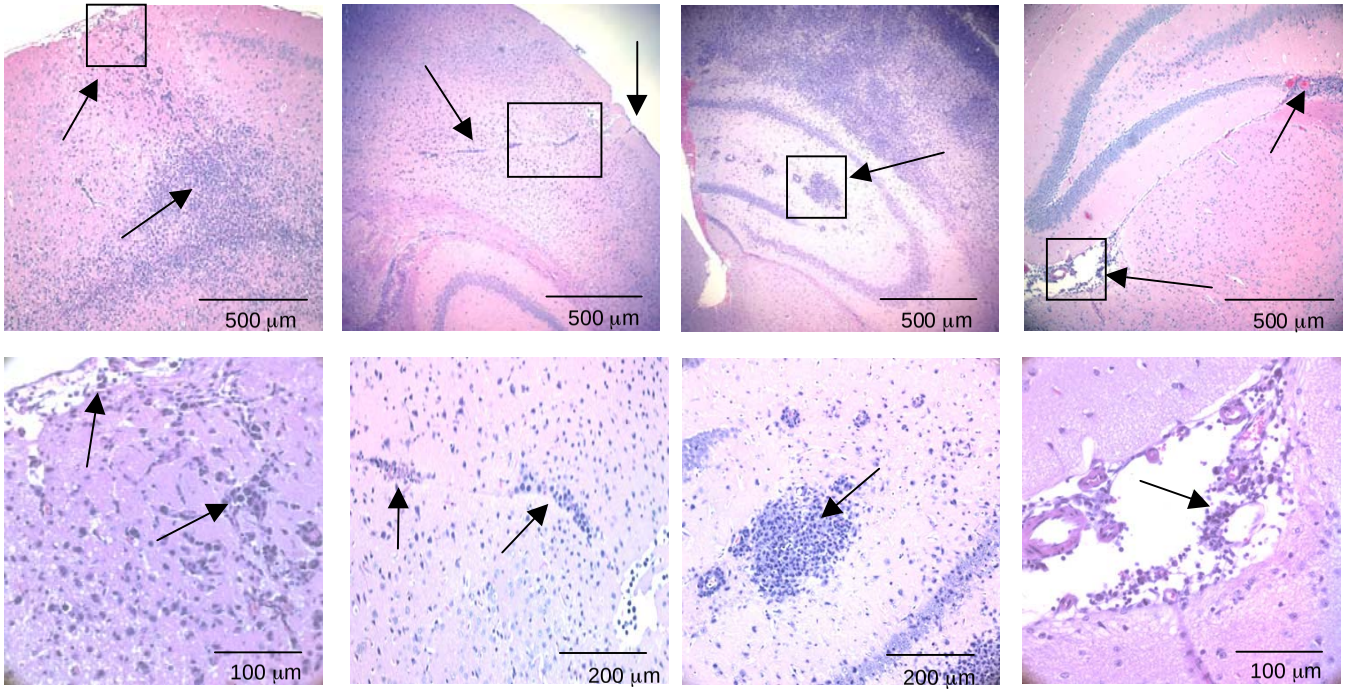
500 μm
500 μm
500 μm
500 μm
100 μm
200 μm
200 μm
100 μm
I
C
I
C
Cortex
Hippocampus

Figure 6. Bioluminescent analysis of distal tumor spread to the brain stem and cerebellum. VM-M3/Fluc tumor fragments or cells were implanted as described in Figure 1. Removed brains were sectioned down the midline and were further dissected into cerebellum and brain stem. Bioluminescence was quantified and plotted on a log scale. All values are expressed as the mean ± SEM of 10 independent samples.

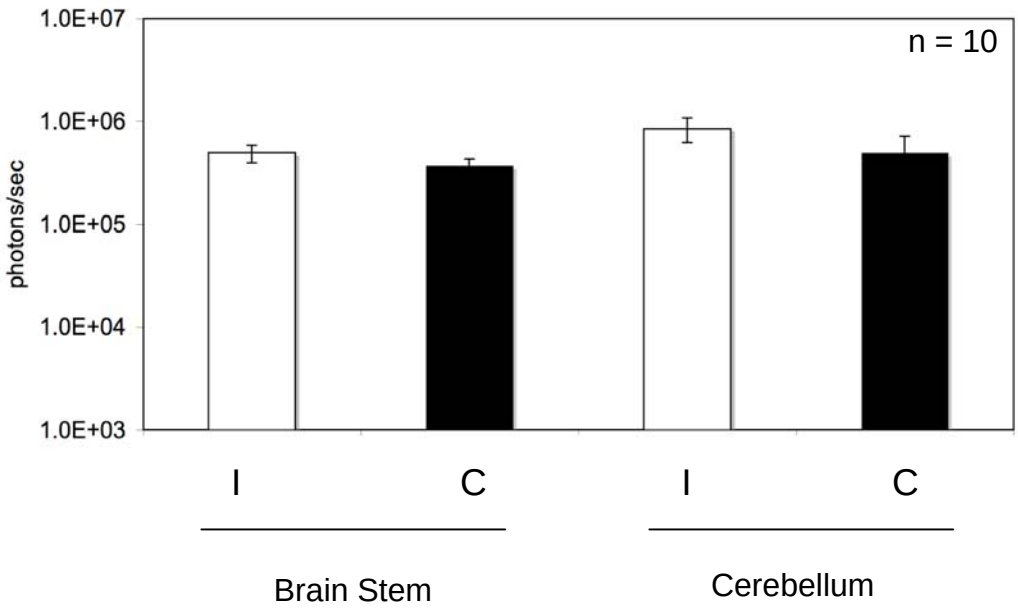
1.0E+07
1.0E+06
1.0E+05
1.0E+04
1.0E+03
photons/sec
n = 10
I
C
I
C
Brain Stem
Cerebellum

Figure 7. Histological evaluation of distal tumor spread to the brain stem and cerebellum. VM-M3/Fluc tumor fragments or cells were implanted as described in Figure 1. Histological analysis (H&E) was used to validate the presence of tumor cells as described in Materials and Methods. Top panel images are shown at 50X. The scale bar represents 250 μm. The black boxes from the top panel images are shown in higher power in the bottom panel. Bottom panel images are shown at 200X. Arrows identify subpial tumor cell spread in the cerebellum and tumor cell invasion in the brain stem. The dashed line demarcates the ipsilateral from the contralateral side of brain stem.

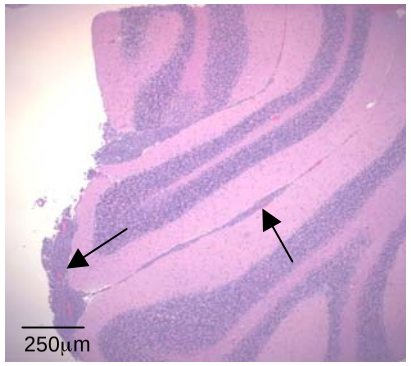

I

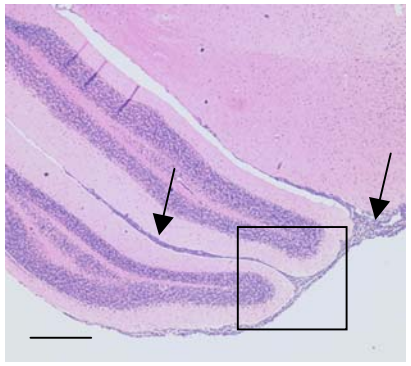

C

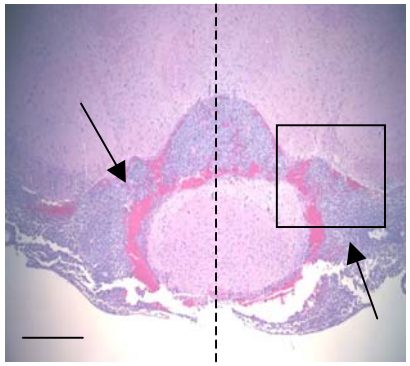

I C

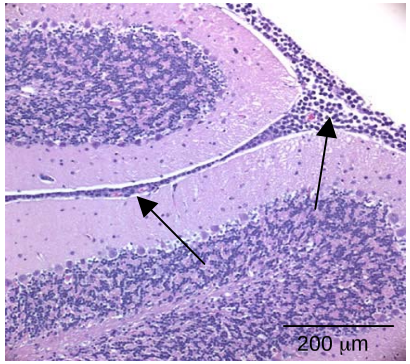

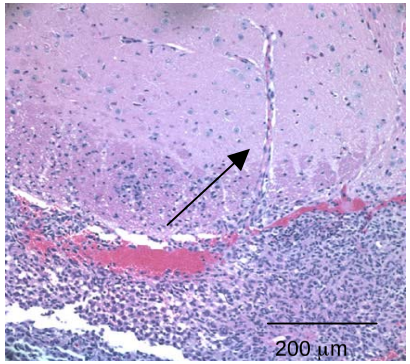

Cerebellum

Brain Stem

Figure 8. Migratory routes of the VM-M3/Fluc brain tumor cells. VM-M3/Fluc tumor fragments or cells were implanted as described in Figure 1. Histological analysis (H&E) was used to validate the presence of tumor cells as described in Materials and Methods. The VM-M3/Fluc tumor cells are shown invading along the pial surface (arrow, **A**), within the corpus callosum (CC, arrow, **B**), along myelinated axons crossing through the striatum (arrow, **C),** through the ventricular system (arrows, **D**), around the blood vessels (arrow, **E**), and around neurons (arrow, **F)**. Images are shown at 100X (A), 50X (B), 400X (C), 200X (D), and 400X (E and F). Arrows identify regions containing tumor cells.

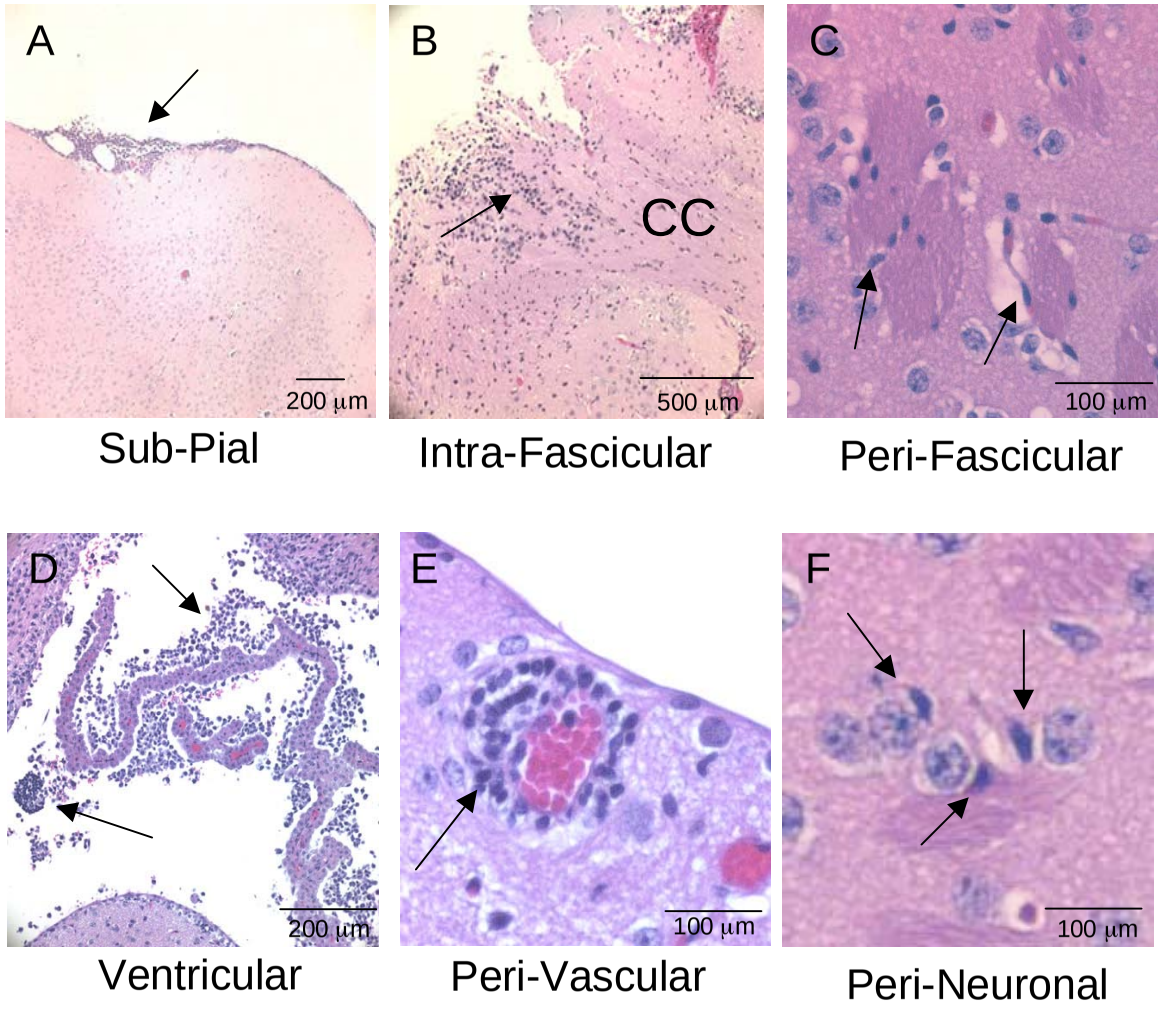
A
200 μm
Sub-Pial
B
CC
500 μm
Intra-Fascicular
C
100 μm
Peri-Fascicular
D
200 μm
Ventricular
E
100 μm
Peri-Vascular
F
100 μm
Peri-Neuronal

Figure 9. Expression of CXCR4 and IGFBP-2 in brain, tumor tissue, and in cultured tumor cells. CXCR4 and IGFBP-2 gene expression was determined by semi-quantitative RT-PCR as described in Materials and Methods.

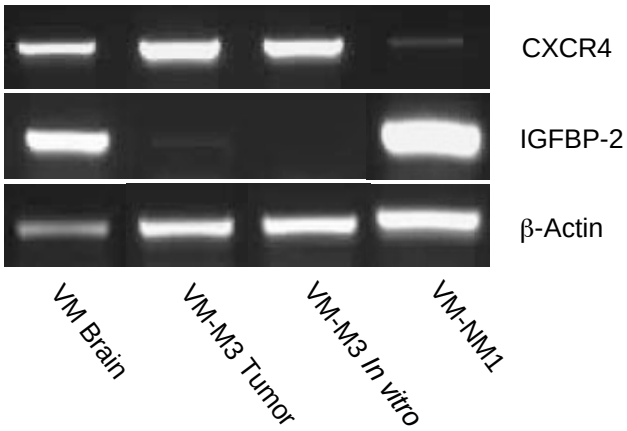
CXCR4
IGFBP-2
β-Actin
VM Brain
VM-M3 Tumor
VM-M3 In vitro
VM-NM1

Figure 10. CXCR4 protein localization in VM-M3 tumor and cells *in vitro*. CXCR4 protein localization was determined *in vitro* and *in vivo* as described in Materials and Methods. Images are shown at 400X, and 630X (insert). Scale bars in the insert represent 10μm.

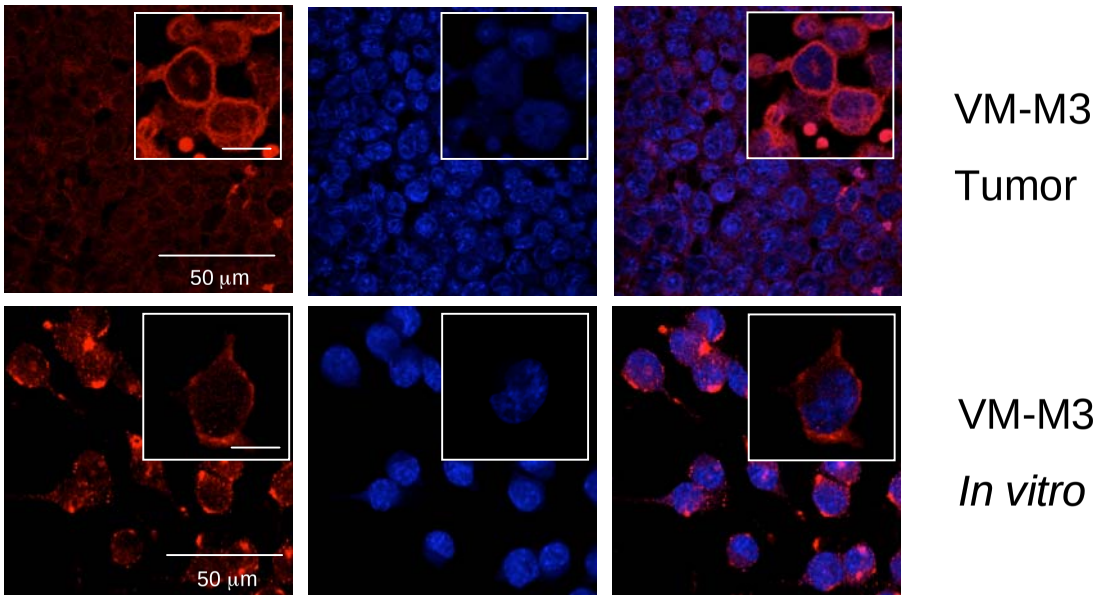
50 μm
50 μm
VM-M3
Tumor
VM-M3
In vitro
CXCR4
Hoechst
Merge

Figure 11. Expression of CXCR4 in invasive VM-M3 tumor cells *in vivo.* CXCR4 protein localization was determined as described in Materials and Methods. Images are shown at 630X. The scale bar is representative of all images shown. Arrows indicate regions of positive CXCR4 expression. The arrow in the top panel illustrates tumor cells invading into the brain parenchyma from the tumor mass (T) under the pial membrane. (BV = blood vessel, P = normal brain parenchyma, T = tumor, WM = white matter)

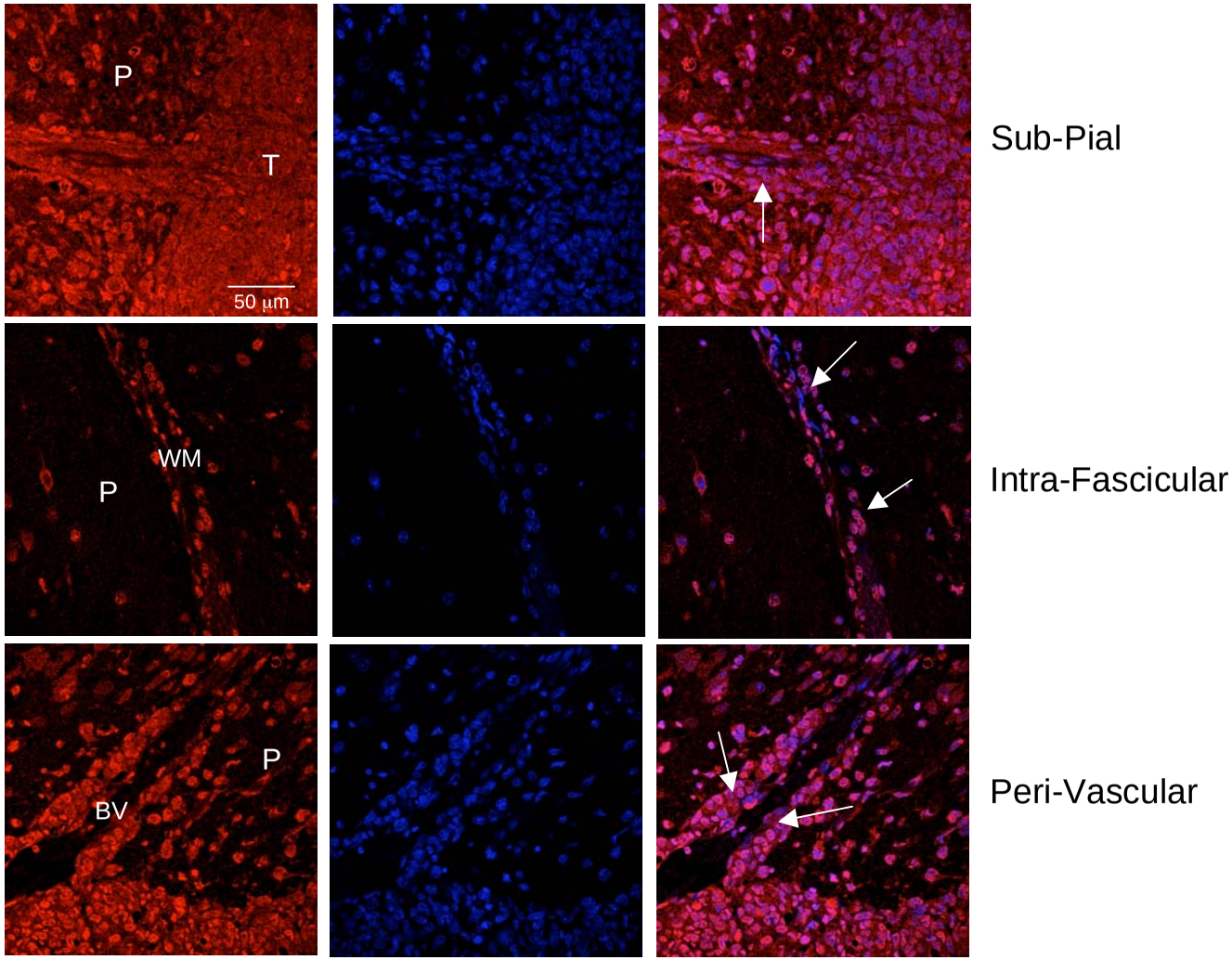
P
T
50 µm
WM
P
P
BV
Sub-Pial
Intra-Fascicular
Peri-Vascular
CXCR4
Hoechst
Merge

Figure 12. Ki-67 expression in VM-M3 tumor. (A) Ki-67 expression in normal brain and in the tumor core was determined as described in Materials and Methods. The black boxes from the top panel images are shown under higher digital zoom in the bottom panel. Ki-67 expression in the invasive tumor cells found migrating through the pial membrane **(B)**, around blood vessels **(B,** arrow), within white matter **(C)**, and invading into the brain paryenchyma **(D)**. Images are shown at 400X. Scale bars are representative of all images of that panel. Arrows indicate tumor cells staining positive for Ki-67 (brown). (CC = corpus callosum)

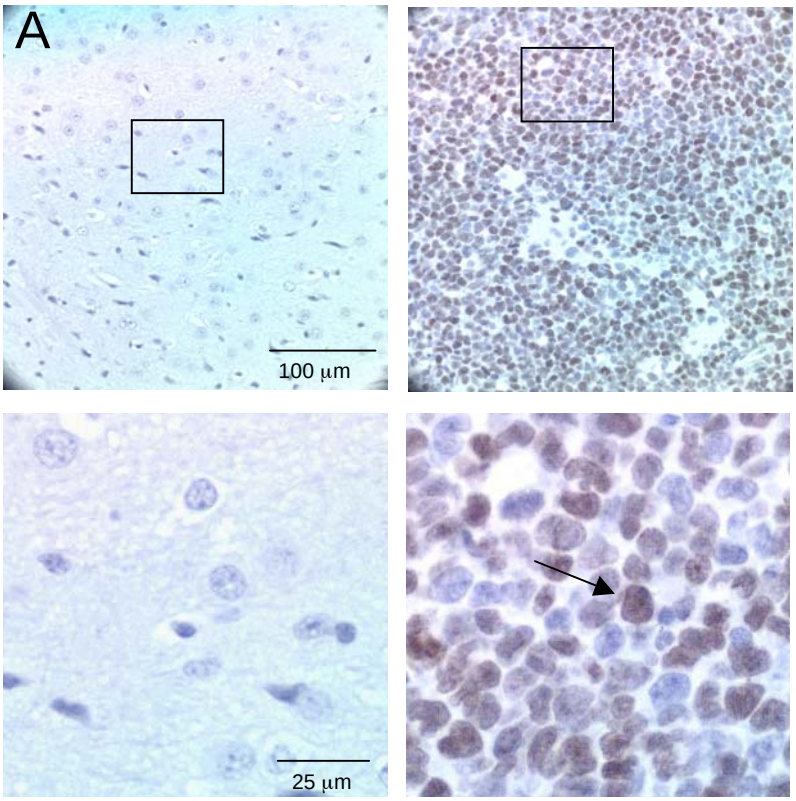

Normal Brain Tumor Core

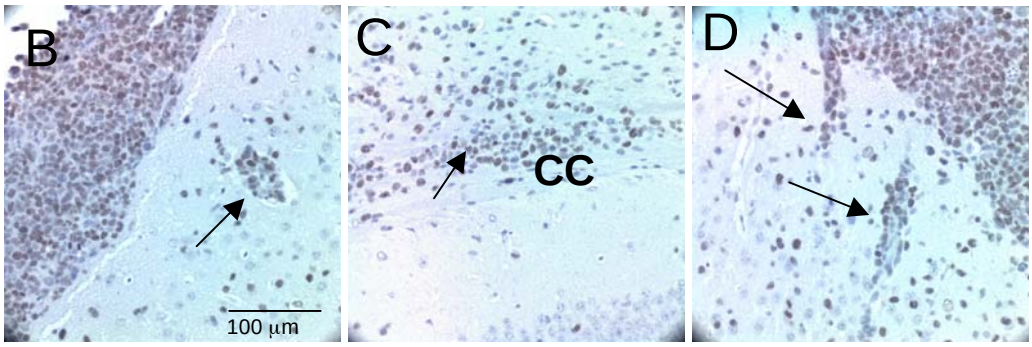

Invasive Tumor Cells

Figure 13. Experimental Design. VM mice were implanted with the VM-M3/Fluc tumor i.c. as described in Materials and Methods and were given a 60% CR starting on day 4-6. Brains were removed 12-15 days post implantation and imaged *ex vivo.*

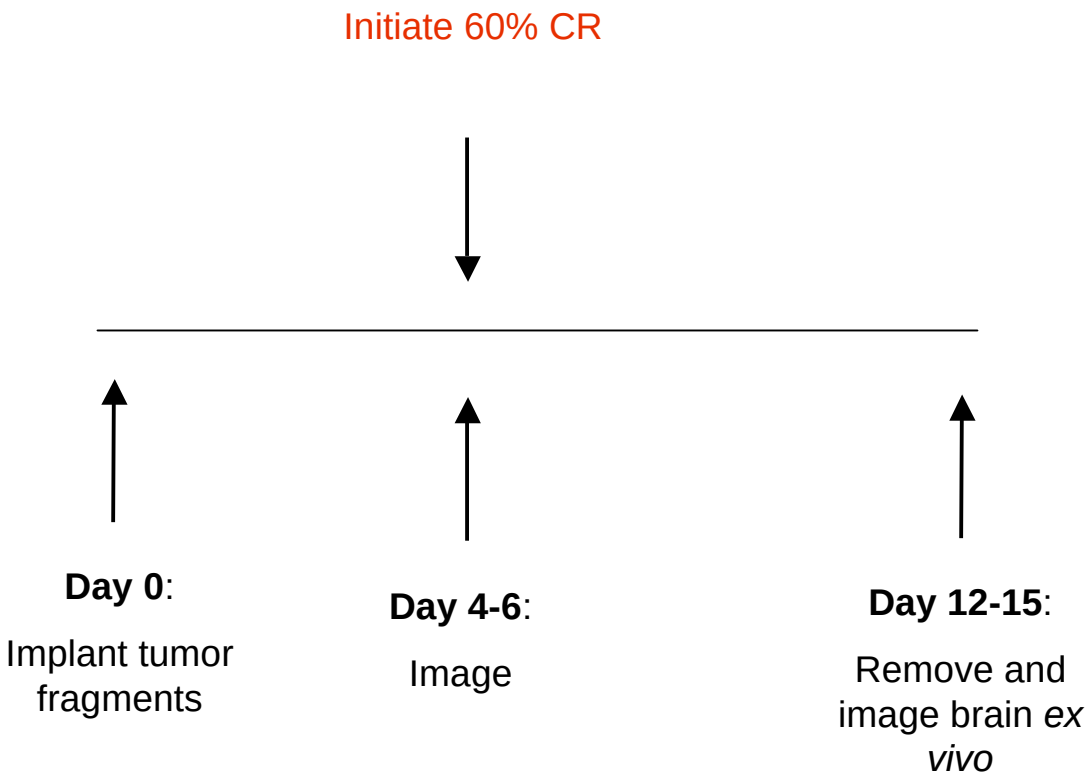
Initiate 60% CR
Day 0:
Implant tumor fragments
Day 4-6:
Image
Day 12-15:
Remove and image brain ex vivo

Figure 14. Effect of calorie restriction on VM-M3/Fluc tumor bearing mice. VM mice were implanted with the VM-M3/Fluc tumor i.c. as described in Materials and Methods. **(A)** The body weights of the VM mice were monitored daily. Values represent the mean ± SEM of 9-10 mice per group. VM mice were sacrificed and plasma was collected for the analysis of glucose **(B)** and ketone **(C)** levels using an enzymatic assay. Values represent the mean ± SEM. The asterisk indicates that the CR values differ significantly from the AL control group at $p < 0.05$.

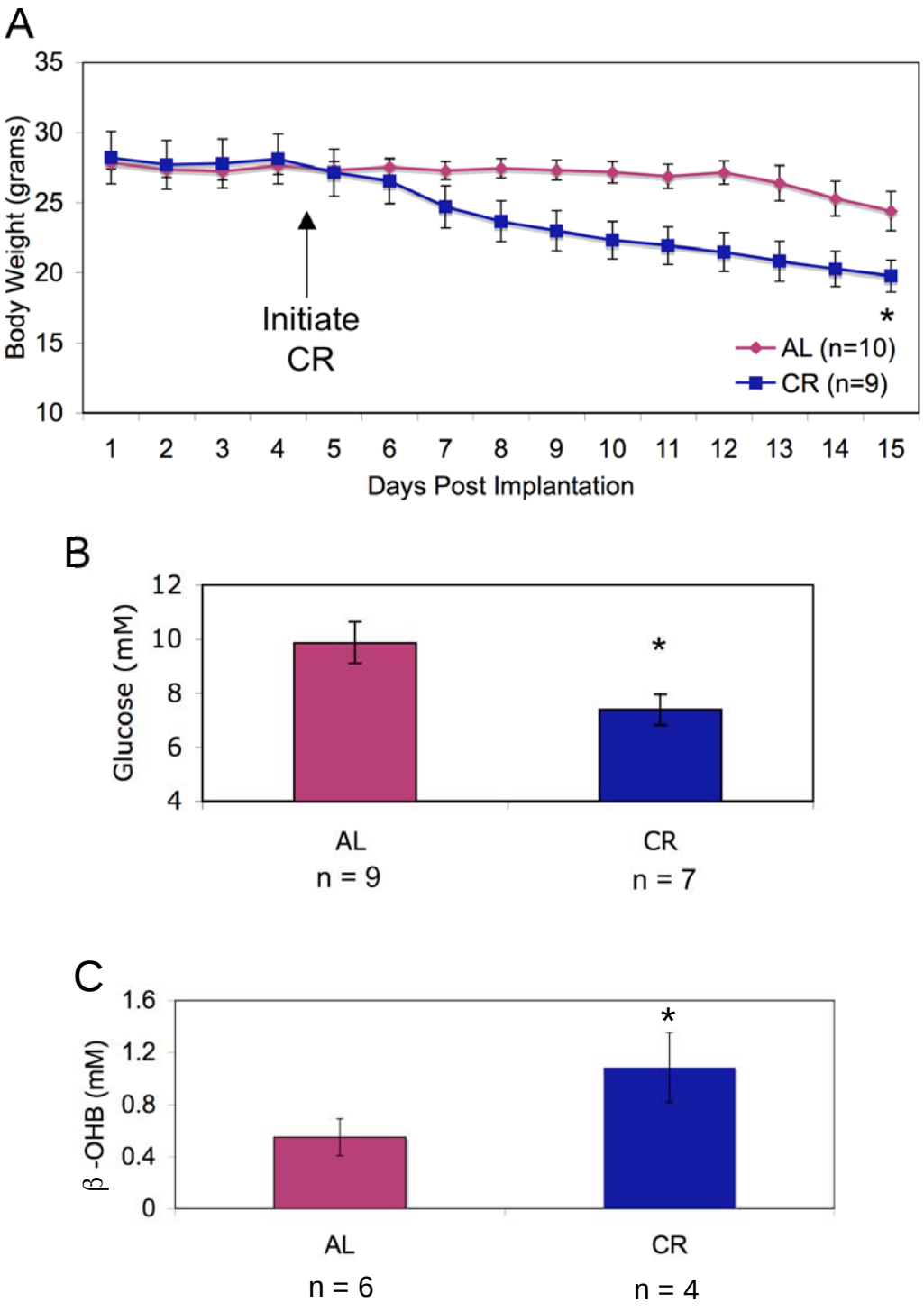
A
Body Weight (grams)
35
30
25
20
15
10
1 2 3 4 5 6 7 8 9 10 11 12 13 14 15
Days Post Implantation
Initiate CR
*
AL (n=10)
CR (n=9)
B
Glucose (mM)
12
10
8
6
4
*
AL
n = 9
CR
n = 7
C
β -OHB (mM)
1.6
1.2
0.8
0.4
0
*
AL
n = 6
CR
n = 4

Figure 15. Influence of calorie restriction on VM-M3/Fluc tumor growth

VM-M3/Fluc tumor fragments were implanted i.c. as described in Materials and Methods. Post imaging, brains were fixed and stained with haematoxylin and eosin (H & E) as described in Materials and Methods. Images are shown at 50X (T=tumor, H=Hippocampus). At least 3 samples were examined per experimental group.

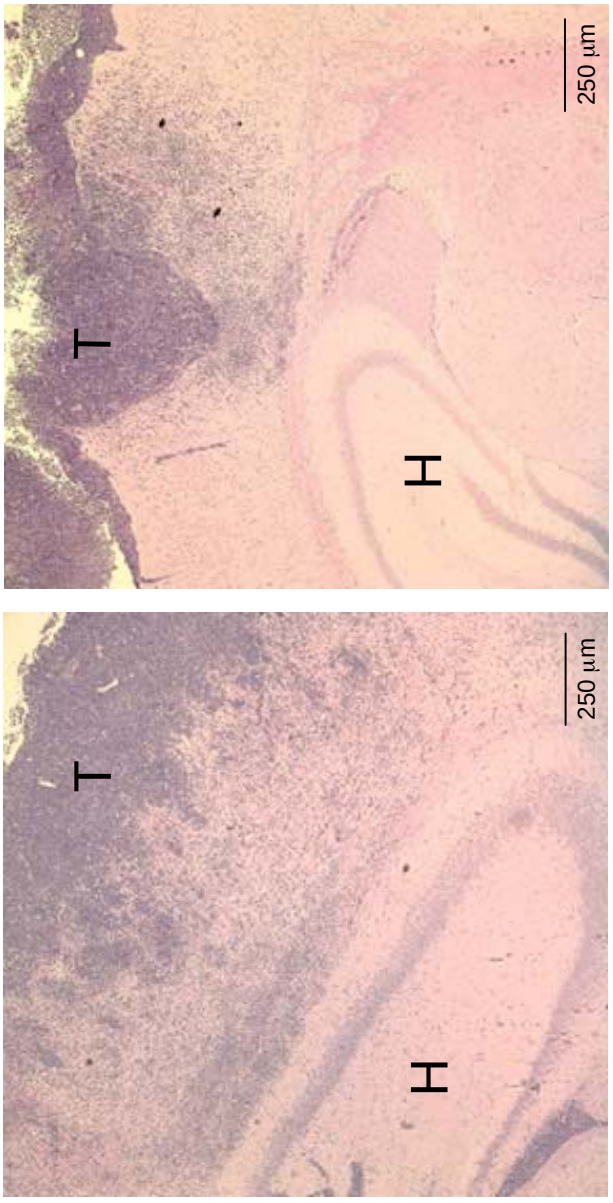
250 µm
T
H
CR
250 µm
T
H
AL

Figure 16. Influence of calorie restriction on bioluminescence in the contralateral hemisphere. VM-M3/Fluc tumor fragments were implanted as described previously. Each hemisphere was imaged for bioluminescence *ex vivo* as described in Materials and Methods. The bioluminescence given off from each hemisphere was added for a total bioluminescence value (photons/sec). Data for the contralateral hemisphere is expressed as the percent of the total photons/sec. Values represent the mean ± SEM of 9-10 mice per group. Representative bioluminescent images are shown. The asterisk indicates that the CR values differ significantly from the AL control group at $p < 0.05$.

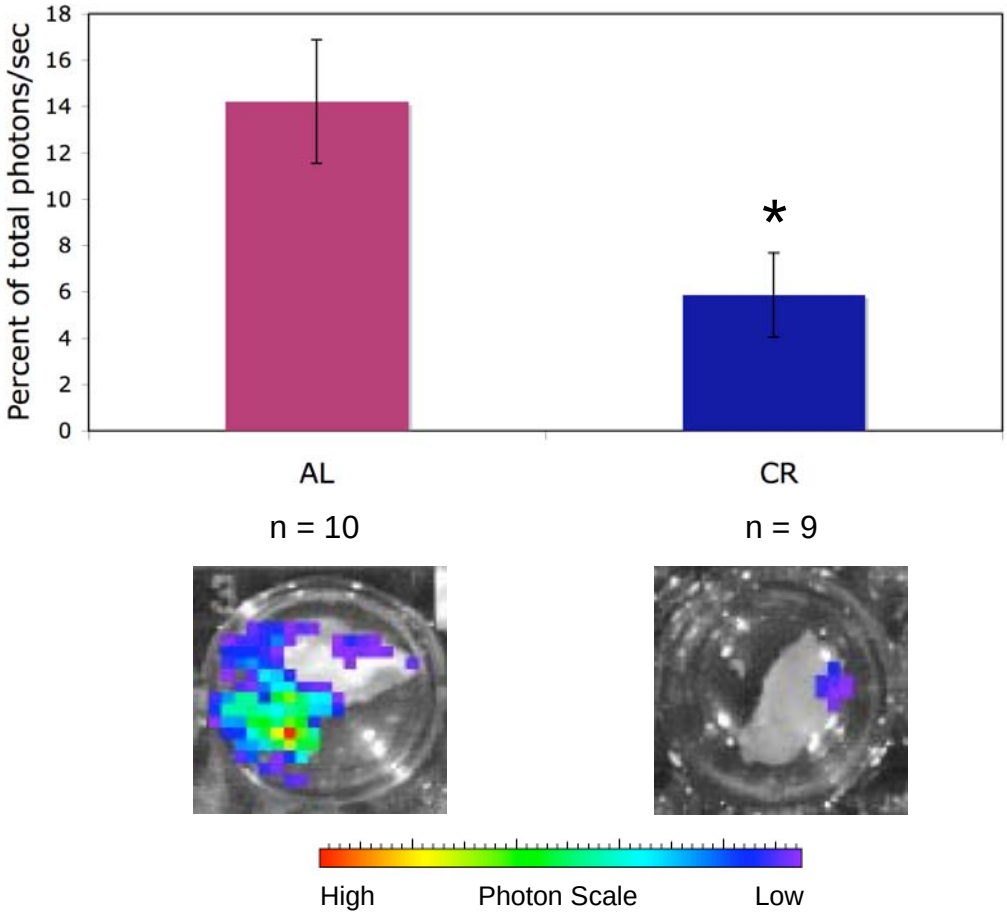
Percent of total photons/sec
18
16
14
12
10
8
6
4
2
0
*
AL
CR
n = 10
n = 9
High
Photon Scale
Low

Figure 17. Influence of calorie restriction on VM-M3/Fluc tumor cell invasion to the contralateral hemisphere. VM-M3/Fluc tumor fragments were implanted as described in Materials and Methods. Histological analysis (H&E) was used to validate the presence of tumor cells as described in Materials and Methods. Top panel images (AL) are shown from left to right at 200X, 100X, 100X, and 200X. Bottom panel (CR) images are shown from left to right at 200X, 100X, 100X, and 200X. At least 3 samples were examined per experimental group.

AL
CR
Brain Stem
Cerebellum
Hippocampus
Cortex
200 µm

Figure 18. Influence of calorie restriction on Ki-67 staining in the primary tumor

Tissue sections were stained and quantitated for Ki-67 (+) tumor cells as described in the Materials and Methods. Three independent areas were quantitated per tumor sample and averaged for a single value. Values represent the mean ± SEM of 3 independent samples per group. The asterisk indicates that the values for the CR group differ from those of the AL control group at a $p < 0.05$. Representative immunohistological sections are shown. Images are shown at 400X. (Ki-67 (+) = brown, arrows)

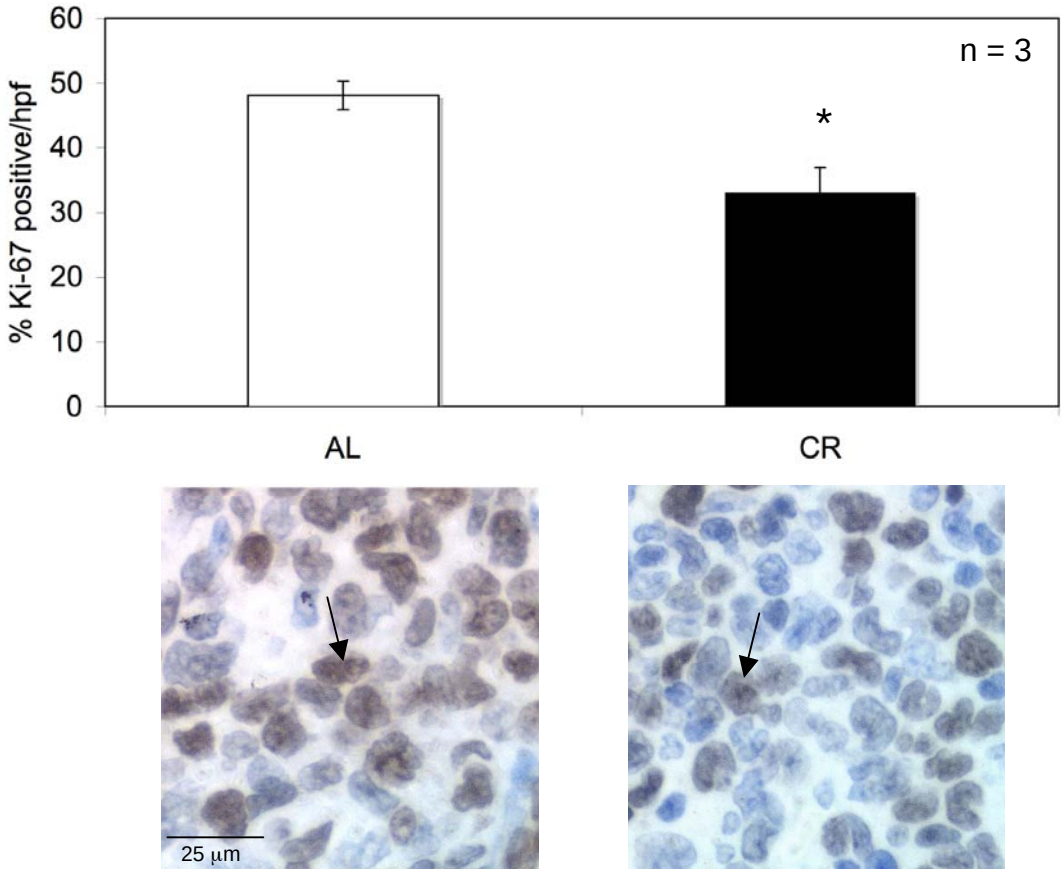
60
50
40
30
20
10
0
% Ki-67 positive/hpf
n = 3
*
AL
CR
25 μm

Figure 19. Growth and metastatic spread of the VM-M3/fluc tumor with bioluminescence imaging. Tumors were implanted s.c as described in the Materials and Methods. **(A)** Dorsal (upper panels) images were taken over 23 days. Ventral (lower panel) images were taken once metastasis was detectable (representative mice shown). **(B)** Bioluminescence from the whole mouse (dorsal and ventral images added together) was quantified and plotted on a log scale. **(C)** At the end of the study organs were removed and imaged *ex vivo* in 300 μg/ml D-luciferin in PBS from 1-15 min and metastasis was quantified and plotted on a log scale. All values are expressed as the means of 6 independent samples ± 95% C.I.

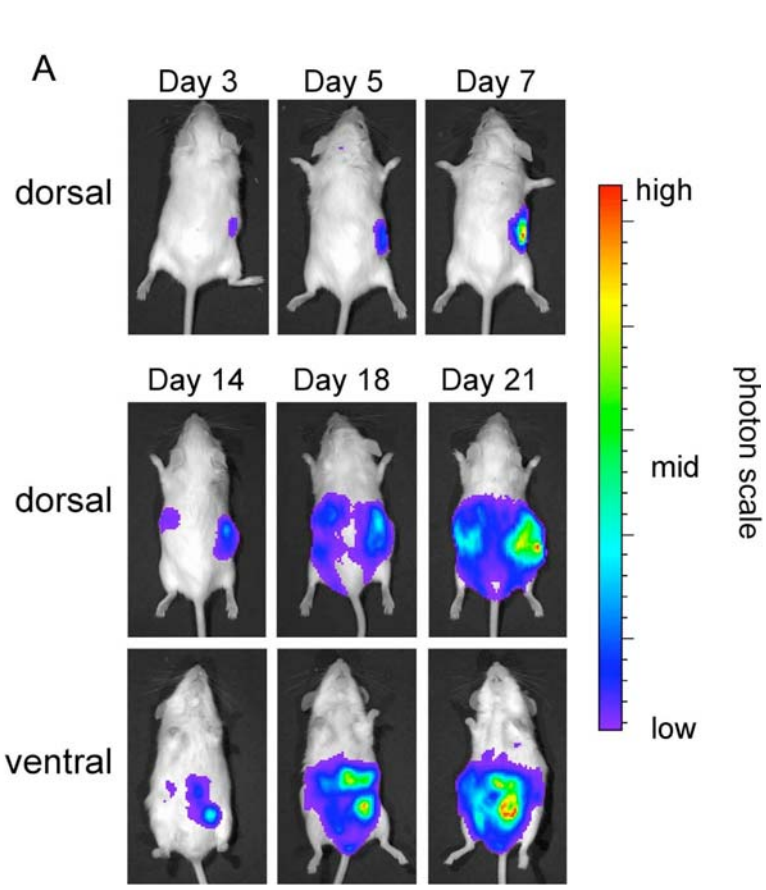
A
Day 3
Day 5
Day 7
dorsal
Day 14
Day 18
Day 21
dorsal
ventral
high
mid
low
photon scale

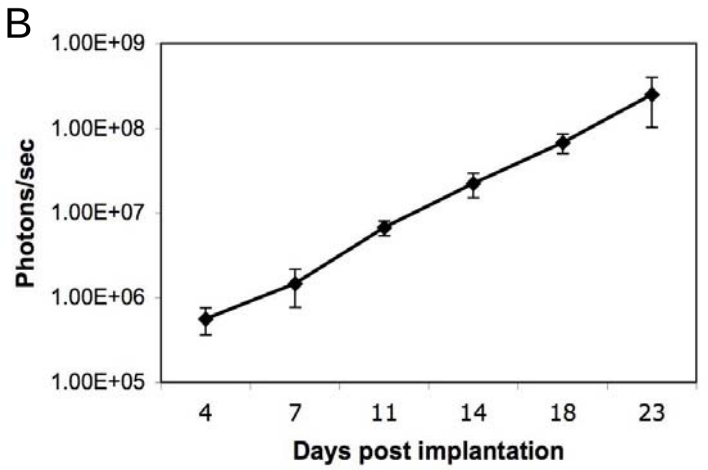
B
1.00E+09
1.00E+08
1.00E+07
1.00E+06
1.00E+05
Photons/sec
4
7
11
14
18
23
Days post implantation

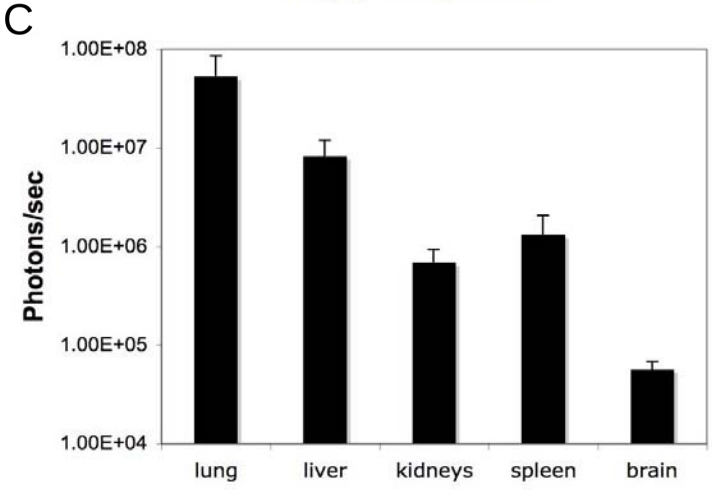
C
1.00E+08
1.00E+07
1.00E+06
1.00E+05
1.00E+04
Photons/sec
lung
liver
kidneys
spleen
brain

Figure 20. Experimental design. VM mice were implanted with the VM-M3/Fluc tumor s.c. as described in Materials and Methods and were given a 60% CR starting on day 5-7. Organs were removed 15-19 days post implantation and imaged *ex vivo.*

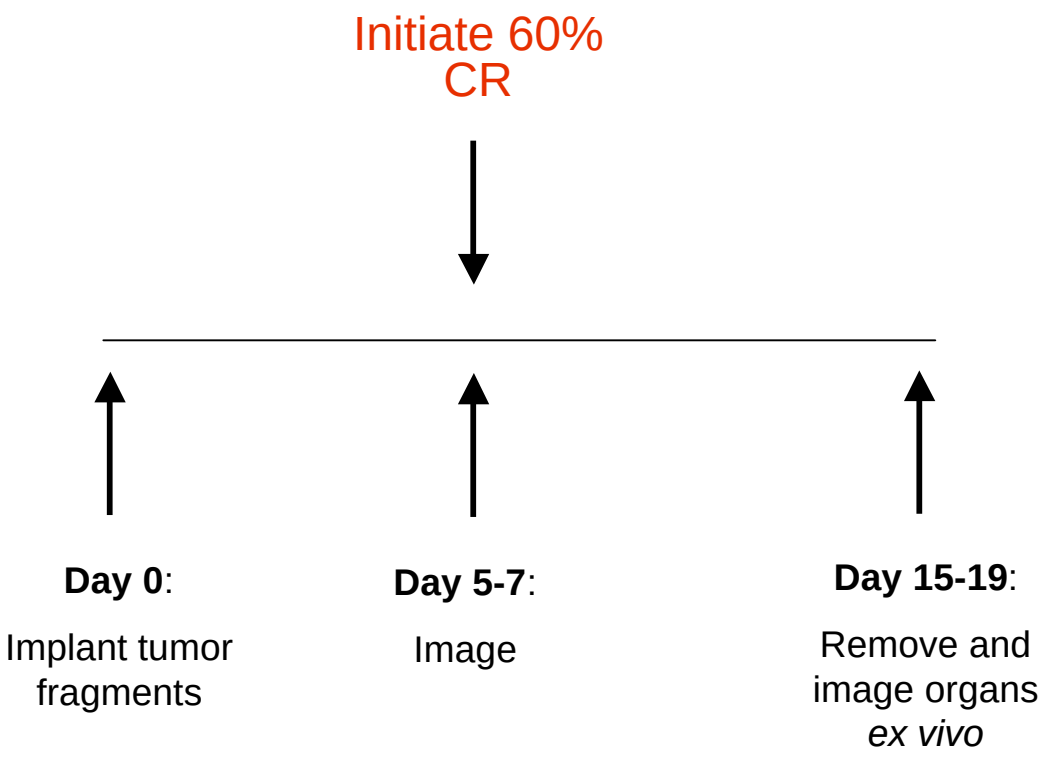
Initiate 60% CR
Day 0:
Implant tumor fragments
Day 5-7:
Image
Day 15-19:
Remove and image organs *ex vivo*

Figure 21. Effect of calorie restriction on VM-M3/Fluc tumor bearing mice. VM mice were implanted with the VM-M3/Fluc tumor s.c. as described in Materials and Methods. **(A)** Body weights were monitored daily. Mice were sacrificed 15-19 days post implantation and blood was collected for the analysis of glucose **(B)** and ketone **(C)** levels using an enzymatic assay. All values represent the mean ± SEM. CR values differ significantly from the AL control group at * $p < 0.05$, ** $p < 0.01$.

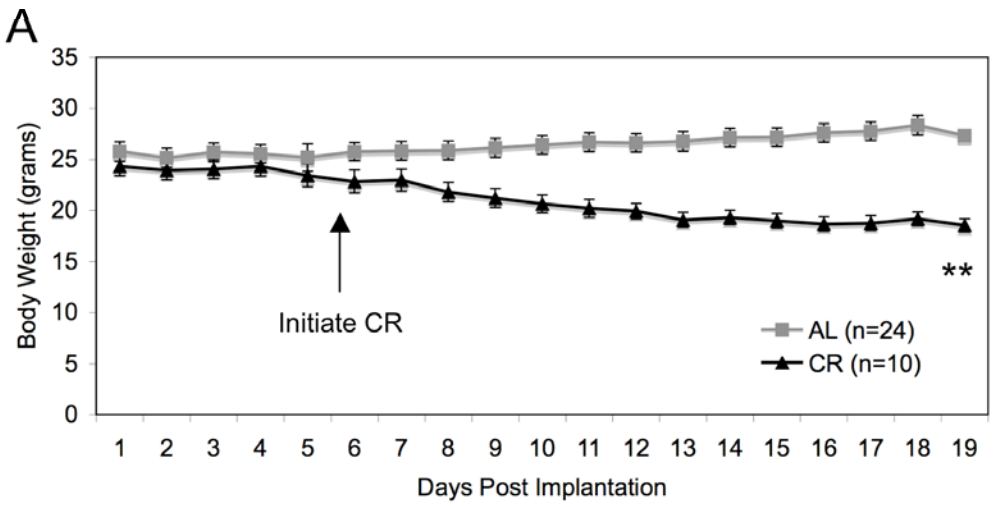
A
Body Weight (grams)
35
30
25
20
15
10
5
0
Initiate CR
**
AL (n=24)
CR (n=10)
1 2 3 4 5 6 7 8 9 10 11 12 13 14 15 16 17 18 19
Days Post Implantation

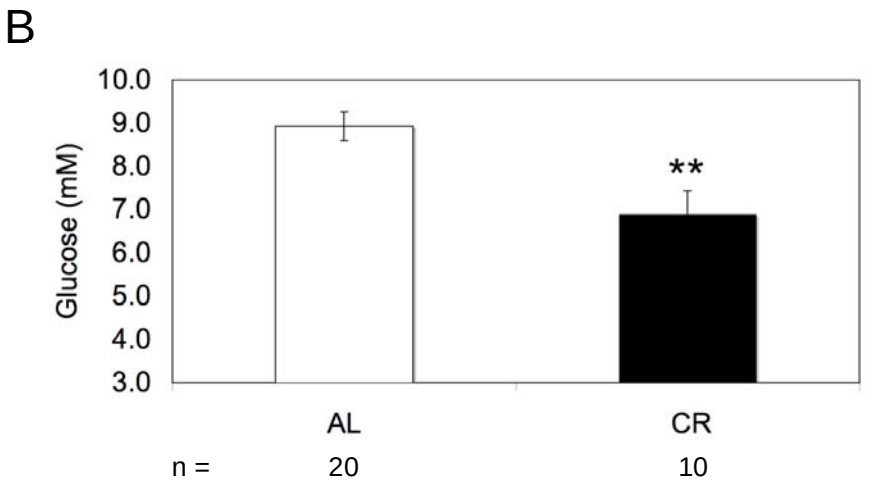
B
Glucose (mM)
10.0
9.0
8.0
7.0
6.0
5.0
4.0
3.0
**
AL
CR
n =
20
10

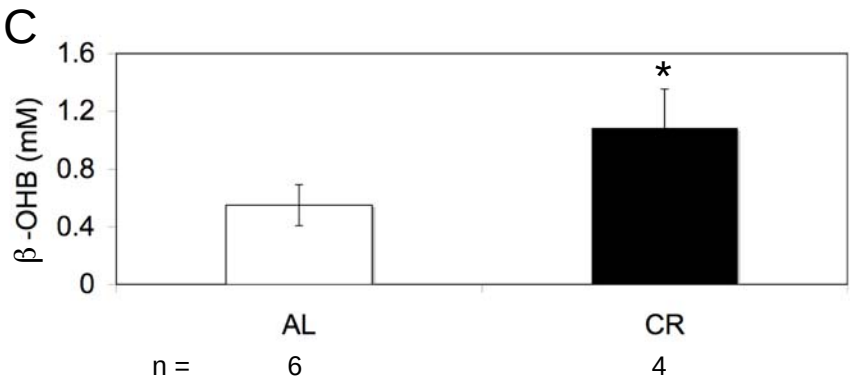
C
β-OHB (mM)
1.6
1.2
0.8
0.4
0
*
AL
CR
n =
6
4

Figure 22. Effect of calorie restriction on VM-M3/Fluc primary tumor size. VM mice were implanted with the VM-M3/Fluc tumor s.c. as described in Materials and Methods. Mice were sacrificed 15-19 days post implantation and the tumors removed and weighed. CR significantly reduced the size of the tumor by approximately half. All values represent the mean ± SEM of 10-24 mice per group. The asterisks indicate that the CR values differ significantly from the AL control group at $p < 0.01$.

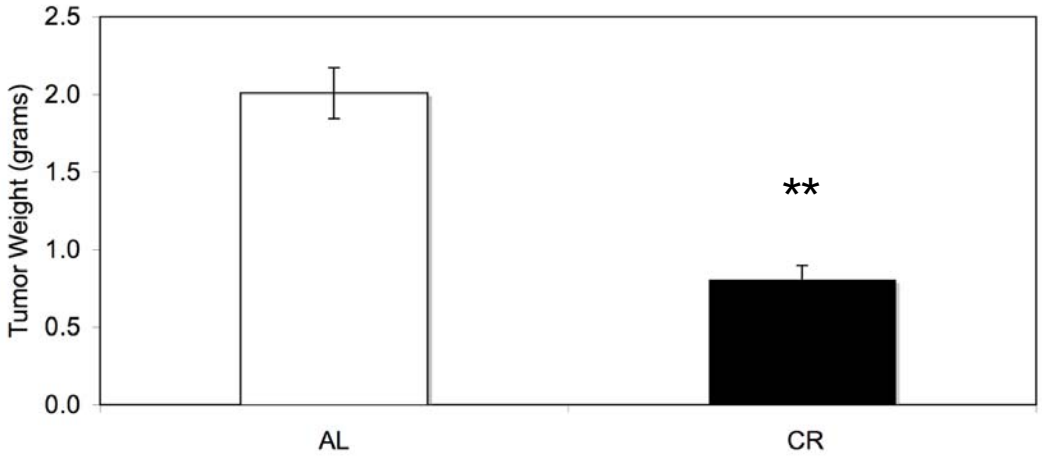

	AL	CR
n =	24	10

Figure 23. Effect of calorie restriction on VM-M3/Fluc tumor metastasis. VM mice were implanted with the VM-M3/Fluc tumor s.c. as described in Materials and Methods. Mice were sacrificed 15-19 days post implantation and the organs were removed and were imaged *ex vivo*. Bioluminescence values were plotted on a log scale. All values represent the mean ± SEM of 8-24 mice per group. There is no statistically significant difference between the AL and CR group for any organ.

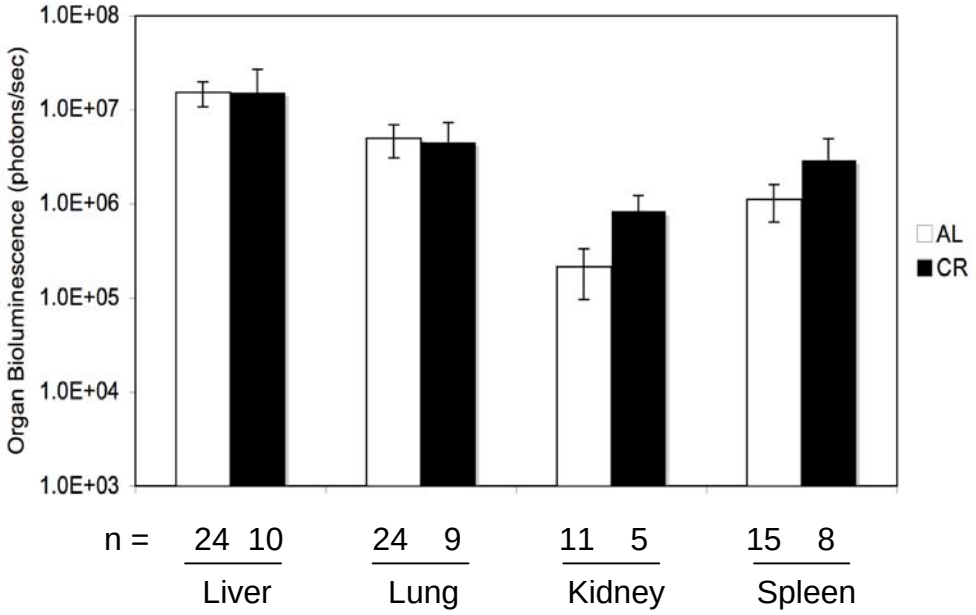
1.0E+08
1.0E+07
1.0E+06
1.0E+05
1.0E+04
1.0E+03
Organ Bioluminescence (photons/sec)
AL
CR
n = 24 10 24 9 11 5 15 8
Liver
Lung
Kidney
Spleen

Figure 24. A differential response to energy stress *in vitro* between CT-2A and VM-M3 tumor cell lines. Approximately 5 x 10^4 cells were seeded in 24 well plates. Cells were immediately imaged in order to obtain a 0 hr baseline bioluminescent value as described in Materials and Methods. Cells were allowed to settle for 6-9 hours before the addition of minimal DMEM media containing either 25 mM glucose or 4 mM glutamine. Cell viability was assessed 24 hours later via bioluminescent imaging. Results show that glucose is more important then glutamine for survival of CT-2A cells while glutamine is more important than glucose for survival of VM-M3 cells. Data are expressed as the mean percent increase in cell number relative to the 0 hr time point ± 95% C.I. of 3-4 independent samples per group. The asterisks indicate that the gln values differ significantly from the gluc values at a $p < 0.01$.

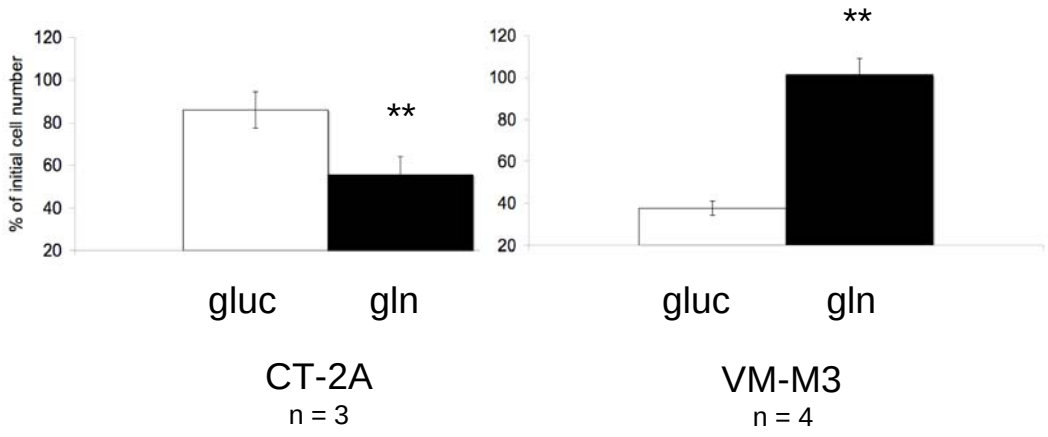
% of initial cell number
120
100
80
60
40
20
**
gluc
gln
CT-2A
n = 3
120
100
80
60
40
20
**
gluc
gln
VM-M3
n = 4

Figure 25. VM-M3 lactate production under energy stress. Cells were incubated in minimal DMEM media containing either 25mM glucose or 4mM glutamine for 24 hours as described in Materials and Methods. Media aliquots from each group were taken after 24 hours. Lactate accumulation was determined using an appropriate enzymatic assay. Results show that glutamine metabolism does not result in significant lactate production. Values represent the mean ± 95% C.I. of 3 independent samples per group. The asterisks indicate that the gln value differs significantly from the gluc value at a $p < 0.01$.

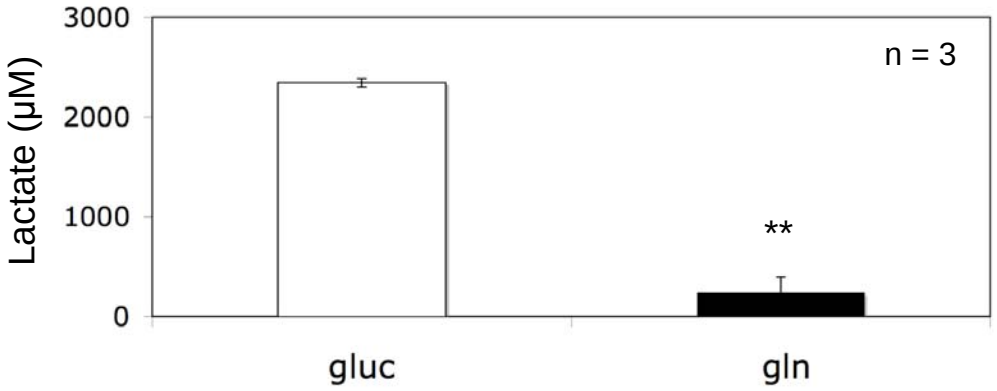
3000
2000
1000
0
Lactate (µM)
n = 3
**
gluc
gln

Figure 26. Effect of glucose and glutamine on VM-M3 viability. VM-M3 cells were seeded as described in Figure 24. After 24 hours, cell viability was assessed via bioluminescent imaging. Glucose and glutamine significantly enhanced cell growth compared to either metabolite alone. Data are expressed as the mean percent increase in cell number relative to the 0 hr time point ± 95% C.I. of 4 independent samples per group. The asterisks indicate that the gluc + gln values differ significantly from the gluc or gln values at a $p < 0.01$.

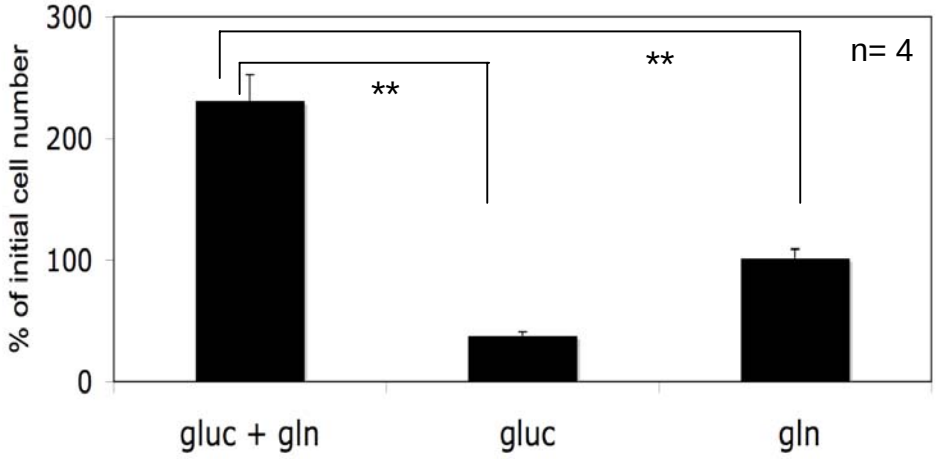
300
200
100
0
% of initial cell number
**
**
n= 4
gluc + gln
gluc
gln

Figure 27. VM-M3 lactate production in the presence of both glucose and glutamine. VM-M3 cells were incubated in minimal DMEM media containing both 25mM glucose and 4mM glutamine for 24 hours as described in Figure 24. Media aliquots from each group were taken after 24 hours. Lactate accumulation was determined using an appropriate enzymatic assay. Incubation in glucose and glutamine resulted in a significant increase in lactate production relative to either metabolite alone. Values represent the mean ± 95% C.I. of 3 independent samples per group. The asterisks indicate that the gluc + gln values differ significantly from the gluc or gln values at a $p < 0.01$.

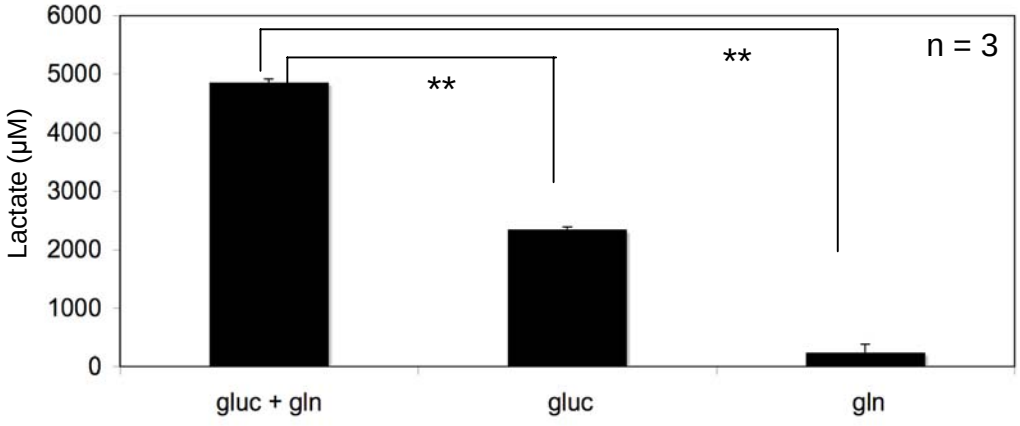
6000
5000
4000
3000
2000
1000
0
Lactate (µM)
n = 3
**
**
gluc + gln
gluc
gln

Figure 28. VM-M3 cell viability in varying glucose and glutamine concentrations. VM-M3 cells were seeded as described in Figure 24. After 24 hours, cell viability was assessed via bioluminescent imaging. Data are expressed as the mean percent increase in cell number relative to the 0 hr time point ± 95% C.I. of 4 independent samples per group.

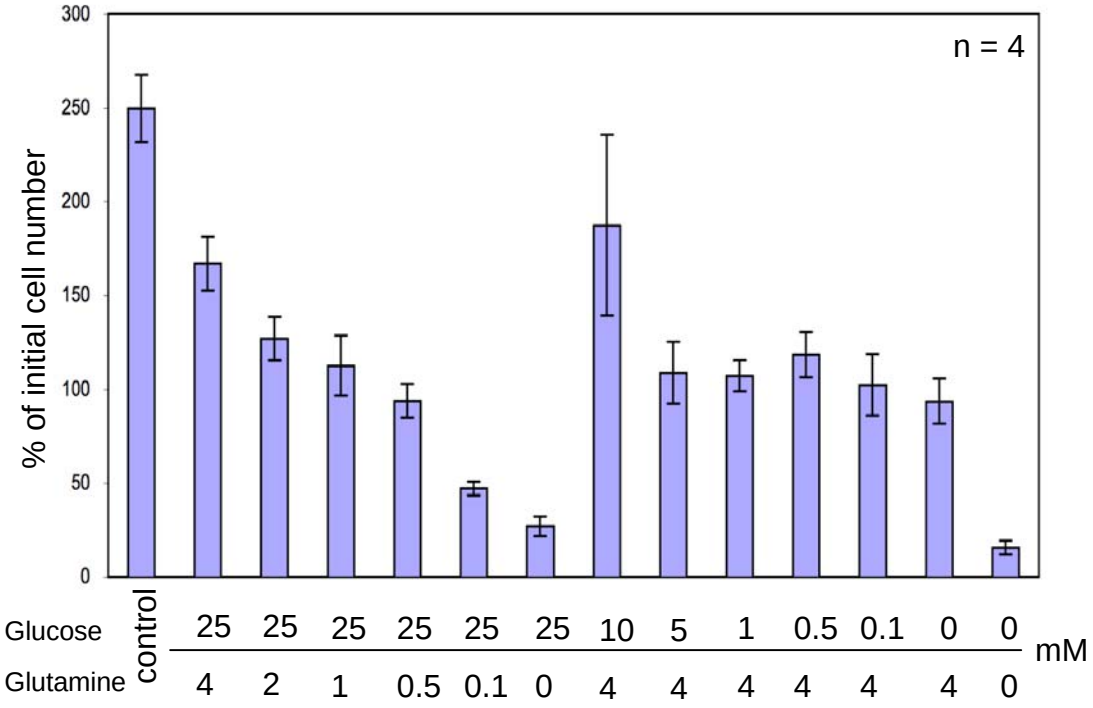
n = 4
% of initial cell number
300
250
200
150
100
50
0
Glucose
Glutamine
control
25 25 25 25 25 25 10 5 1 0.5 0.1 0 0
mM
4 2 1 0.5 0.1 0 4 4 4 4 4 4 0

Figure 29. Effect of *meso*-Tartrate on VM-M3 cell viability under energy stress. VM-M3 cells were seeded as described in Figure 24 in the presence or absence of 3mM *meso*-Tartrate. After 24 hours, cell viability was assessed via bioluminescent imaging. *Meso*-Tartrate significantly reduced cell viability in gluc + gln, but not in gln alone. Data are expressed as the mean percent increase in cell number relative to the 0 hr time point ± 95% C.I. of 4 independent samples per group. The asterisks indicate that the gluc + gln + meso-Tartrate values differ significantly from the gluc + gln values at a $p < 0.01$.

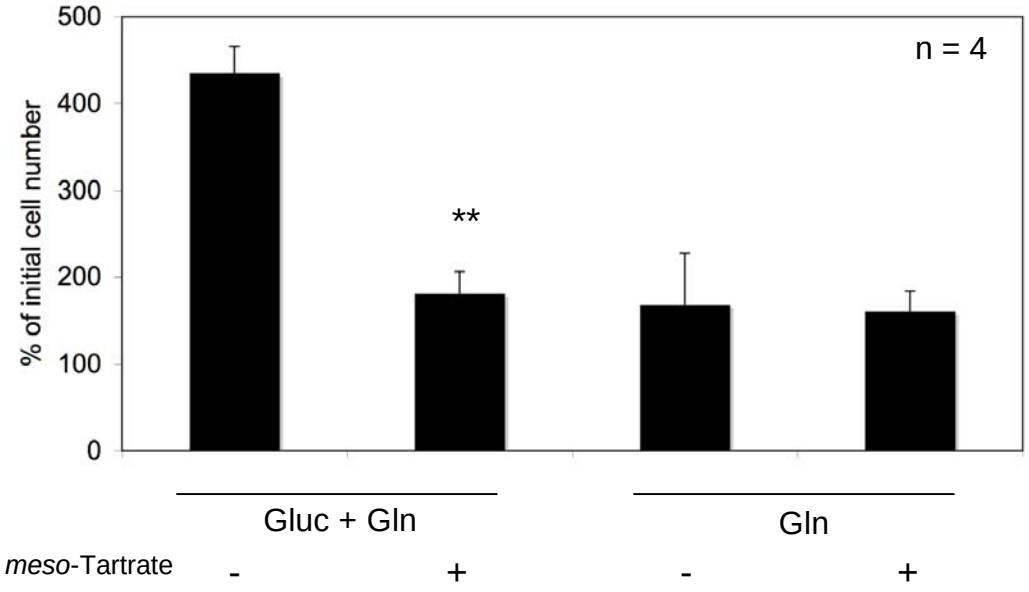

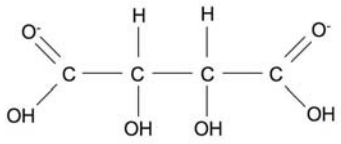

Meso-Tartrate

Figure 30. Effect of *meso*-Tartrate on VM-M3 lactate production. VM-M3 cells were seeded as described in Figure 24 in the presence or absence of 3mM *meso*-Tartrate. Media aliquots were taken after 24 hours. Lactate accumulation was determined using an appropriate enzymatic assay. *Meso*-Tartrate significantly reduced lactate production in gluc + gln, but not in gln alone. Values represent the mean ± 95% C.I. of 3-4 independent samples per group. The asterisks indicate that the gluc + gln + *meso*-Tartrate values differ significantly from the gluc + gln values at a $p < 0.01$.

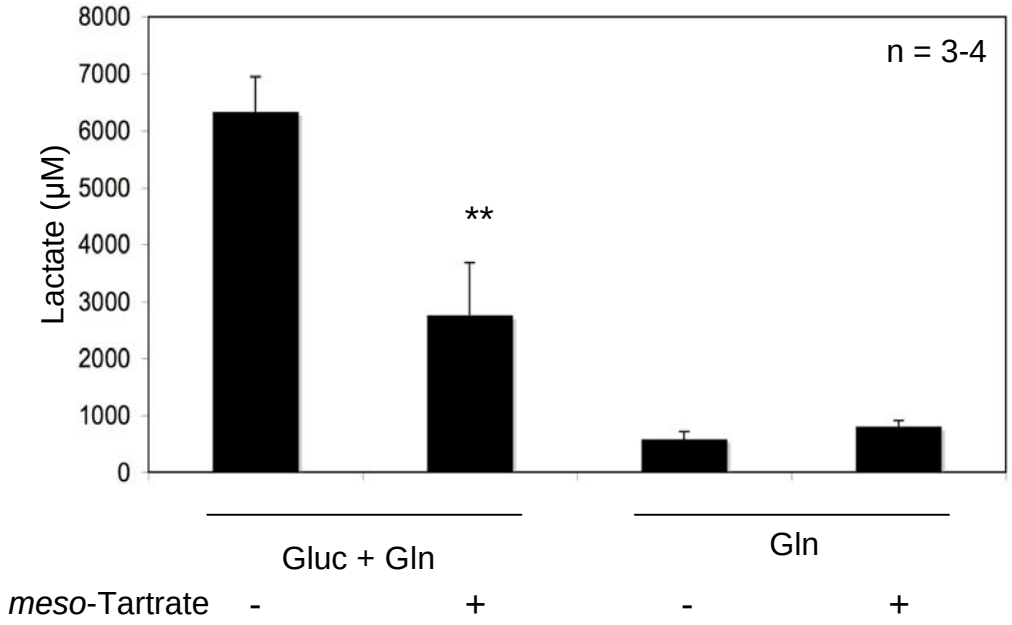
8000
7000
6000
5000
4000
3000
2000
1000
0
Lactate (µM)
n = 3-4
**
Gluc + Gln
Gln
meso-Tartrate - + - +

Figure 31. Effect of 3-Nitropropionic acid (3-NP) on VM-M3 cell viability under energy stress. VM-M3 cells were seeded as described in Figure 24 in the presence or absence of 2mM 3-NP. After 24 hours, cell viability was assessed via bioluminescent imaging. Data are expressed as the mean percent increase in cell number relative to the 0 hr time point ± 95% C.I. of 4 independent samples per group. The asterisks indicate that the 3-NP values differ significantly from the corresponding condition without 3-NP at a $p < 0.01$.

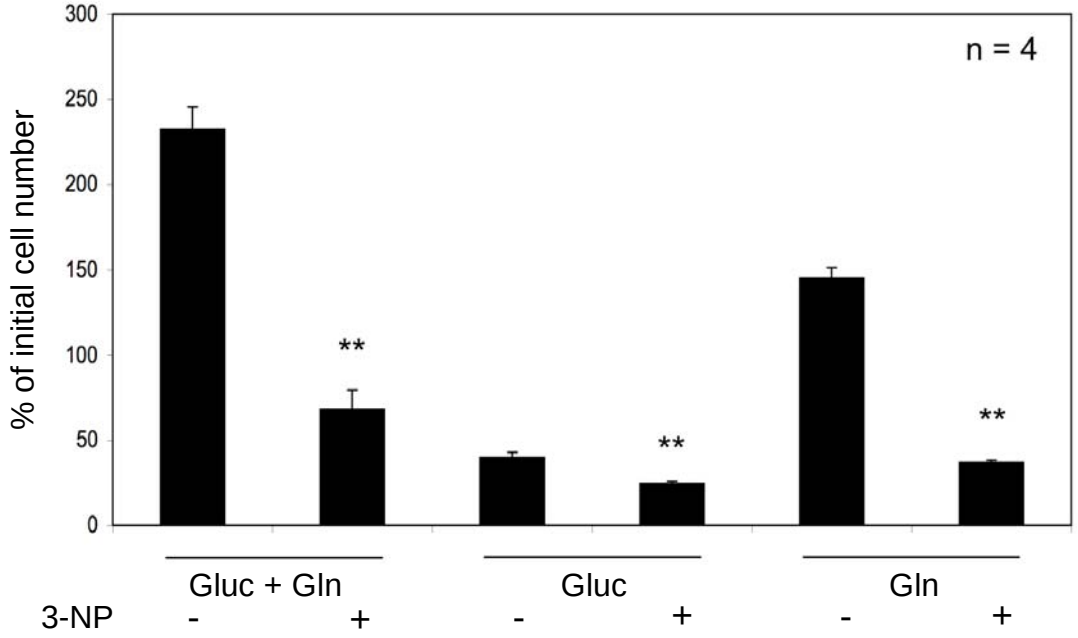
% of initial cell number
300
250
200
150
100
50
0
n = 4
**
**
**
Gluc + Gln
Gluc
Gln
3-NP
-
+
-
+
-
+

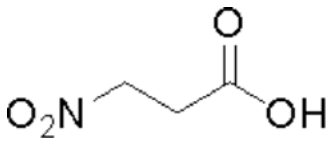
O
O2N
OH

3-NP

Figure 32. Effect of fatty acid metabolism on VM-M3 cell viability in glutamine. VM-M3 cells were seeded as described in Figure 24 in the presence or absence of 1mM heptanoic acid (HA) in 4mM glutamine (gln). After 24 hours, cell viability was assessed via bioluminescent imaging. VM-M3 cell viability was enhanced in gln + HA relative to either metabolite alone. Data are expressed as the mean percent increase in cell number relative to the 0 hr time point ± 95% C.I. of 3-4 independent samples per group. The asterisks indicate that the gln + HA values differ significantly from the gln or HA values at a $p < 0.01$.

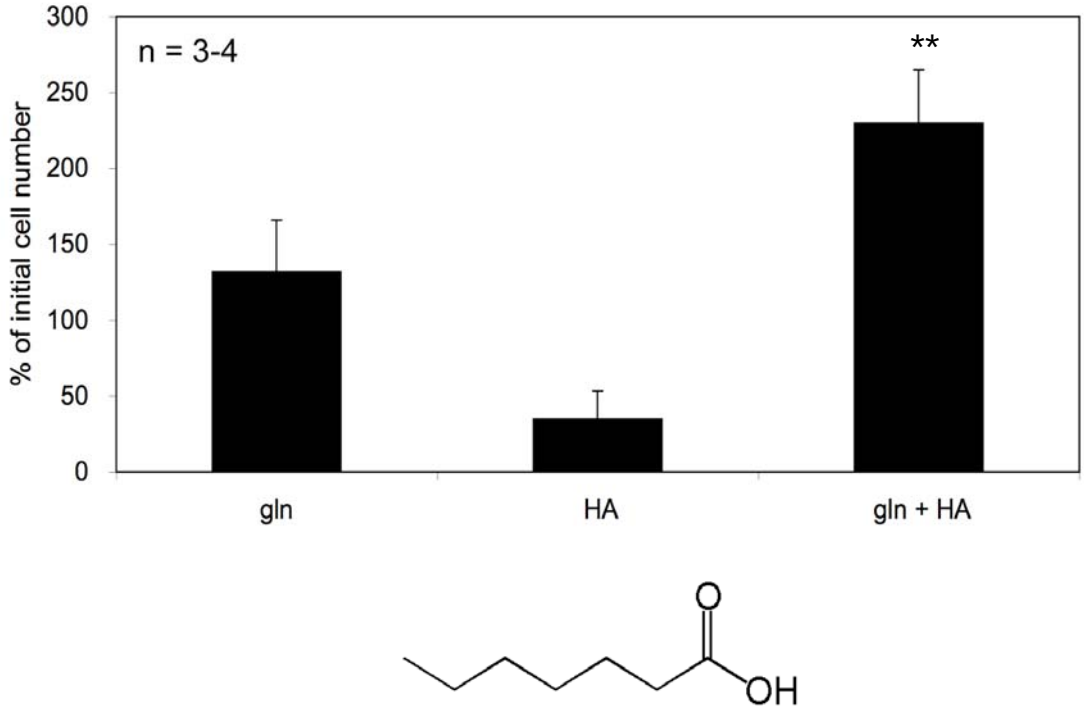

Heptanoic Acid

Figure 33. Effect of ketones on VM-M3 cell viability *in vitro*. VM-M3 cells were seeded as described in Figure 24 in the presence or absence of 10 mM β-hydroxybutyrate. After 24 hours cell viability was assessed via bioluminescent imaging. VM-M3 cell viability was unaffected by the presence of β-hydroxybutyrate in gluc + gln and in gluc alone. VM-M3 cell viability was slightly reduced in the presence of β-hydroxybutyrate in a gln media. Data are expressed as the mean percent increase in cell number relative to the 0 hr time point ± 95% C.I. of 3 independent samples per group. The asterisks indicate that gln + β-OHB was significantly less than gln at a $p < 0.01$.

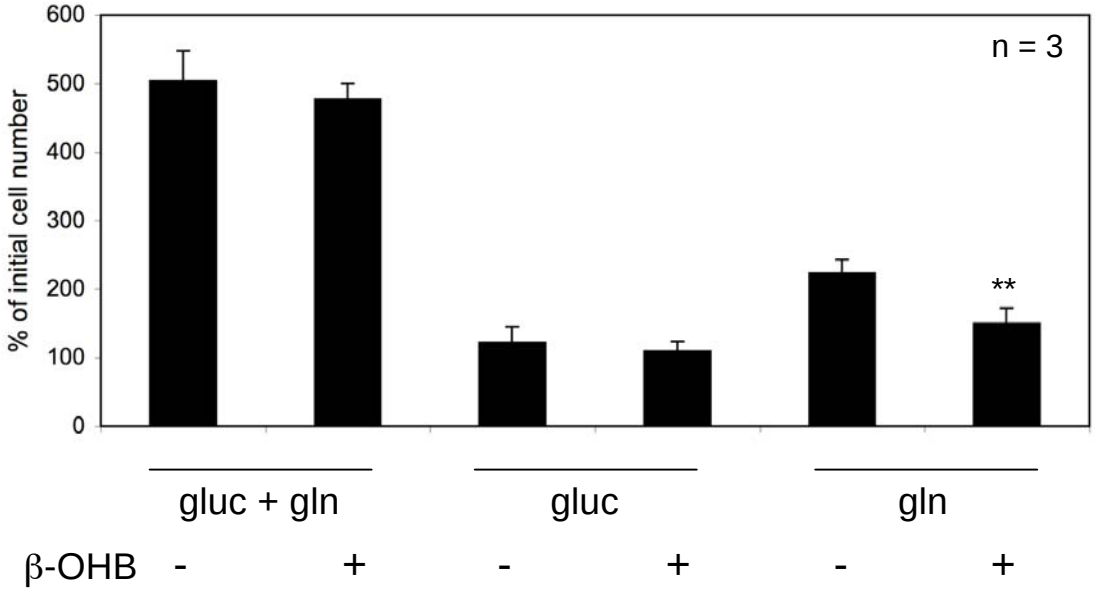
600
500
400
300
200
100
0
% of initial cell number
n = 3
**
gluc + gln
gluc
gln
β-OHB - + - + - +

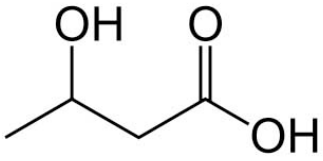
OH
O
OH

β-OHB

Figure 34. Effect of oligomycin on VM-M3 and CT-2A cell viability under energy stress. VM-M3 and CT-2A cells were seeded as described in the Materials and Methods in the presence or absence of 5μg/μl oligomycin in 4mM glutamine (VM-M3) or 25mM glucose (CT-2A). Cell viability was determined over 2 hours via bioluminescent imaging. Both cell lines maintained viability in the presence of the inhibitor. Data are expressed as the mean percent increase in cell number relative to the 0 hr time point ± 95% C.I. of 3- 4 independent samples per group.

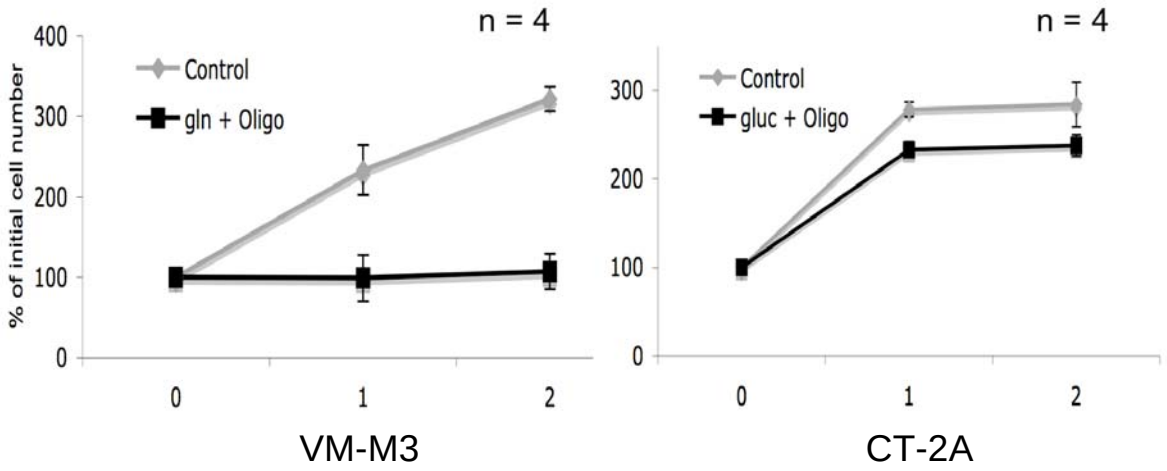

VM-M3 CT-2A

Hours

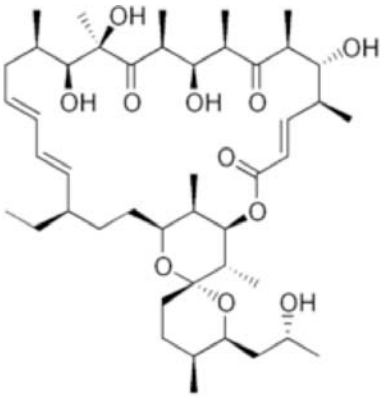

Oligomycin

Figure 35. Effect of oligomycin on CT-2A lactate production. CT-2A cells were seeded as described in the Materials and Methods in the presence or absence 5μg/μl oligomycin in 25mM glucose. Media aliquots were taken after each time point. Lactate accumulation was determined using an appropriate enzymatic assay. Lactate levels were increased in the presence of the F1-ATPase inhibitor. Values represent the mean ± 95% C.I. of 3-4 independent samples per group. The asterisk indicates that the gluc + oligo values differ significantly from the control values at a $p < 0.05$.

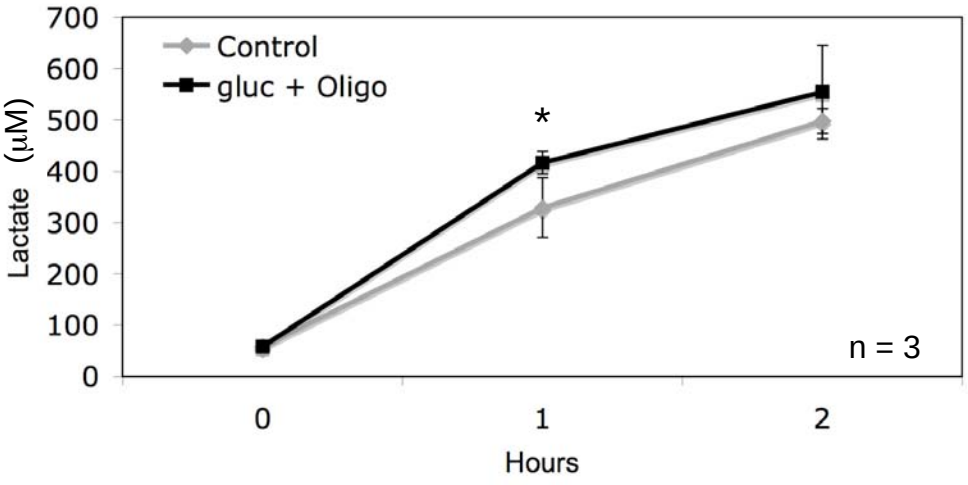
700
600
500
400
300
200
100
0
Lactate (μM)
Control
gluc + Oligo
*
n = 3
0
1
2
Hours

Figure 36. Effect of diadenosine pentaphosphate (Ap5A) on VM-M3 cell viability under energy stress. VM-M3 cells were seeded as described in Figure 24 in the presence or absence of 175μM Ap5A. After 24 hours, cell viability was assessed via bioluminescent imaging. VM-M3 cell viability was significantly reduced in the presence of Ap5A in gln. Ap5A did not significantly affect viability in gluc + gln or in gluc alone. Data are expressed as the mean percent increase in cell number relative to the 0 hr time point ± 95% C.I. of 4 independent samples per group. The asterisks indicate that the gln + Ap5A values differ significantly from the gln values at a $p < 0.01$.

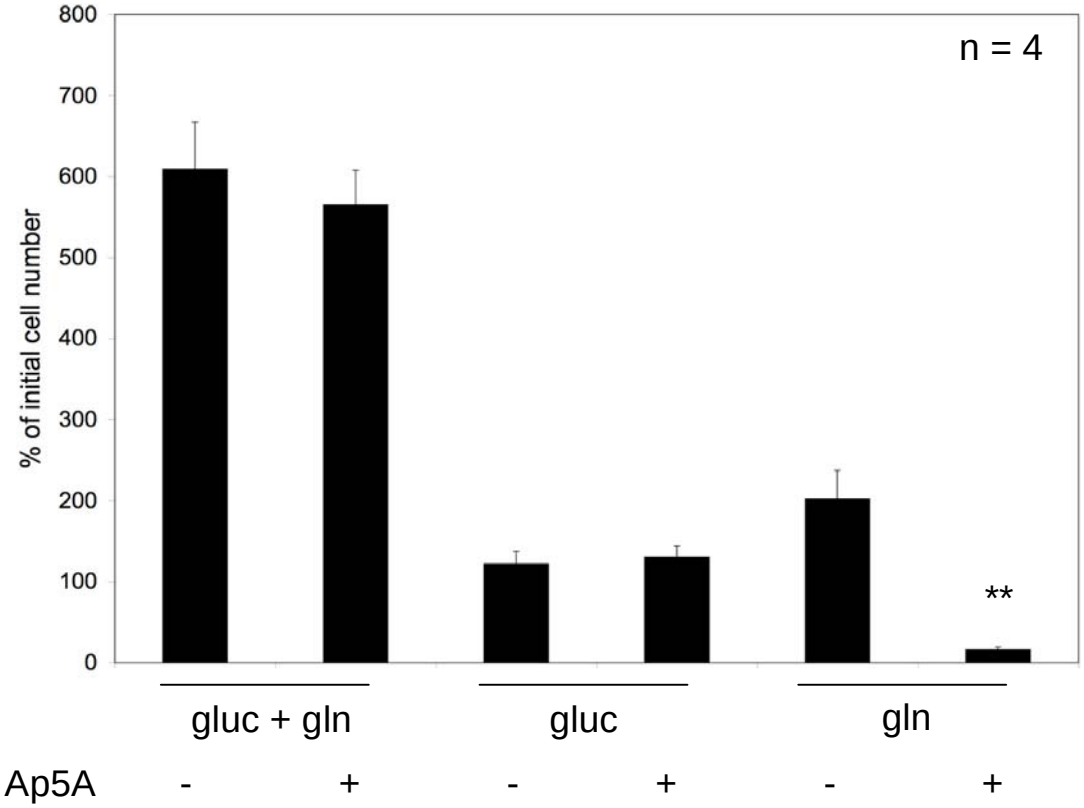
n = 4
% of initial cell number
800
700
600
500
400
300
200
100
0
**
gluc + gln
gluc
gln
Ap5A
-
+
-
+
-
+

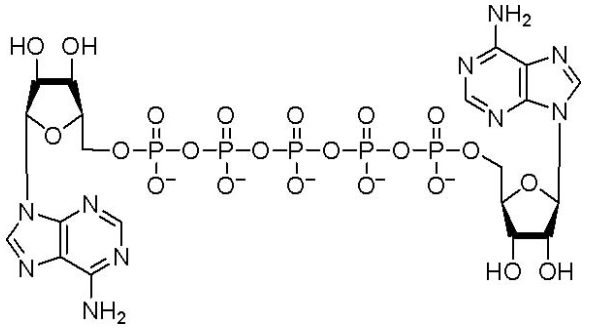

Ap5A

Figure 37. Effect of 6-diazo-5-oxo-L-norleucine (DON) on VM-M3 cell viability *in vitro*. VM-M3/Fluc cells were seeded in DMEM in 24 well plates as described in the Materials and Methods and treated with DON (50 and 250 μM). Cells were imaged every 24 hours using the Xenogen IVIS system. DON treatment significantly reduced cell growth over 48 hours. Data are expressed as the mean percent increase in cell number relative to the 0 hr time point ± 95% C.I. of 4 independent samples per concentration.

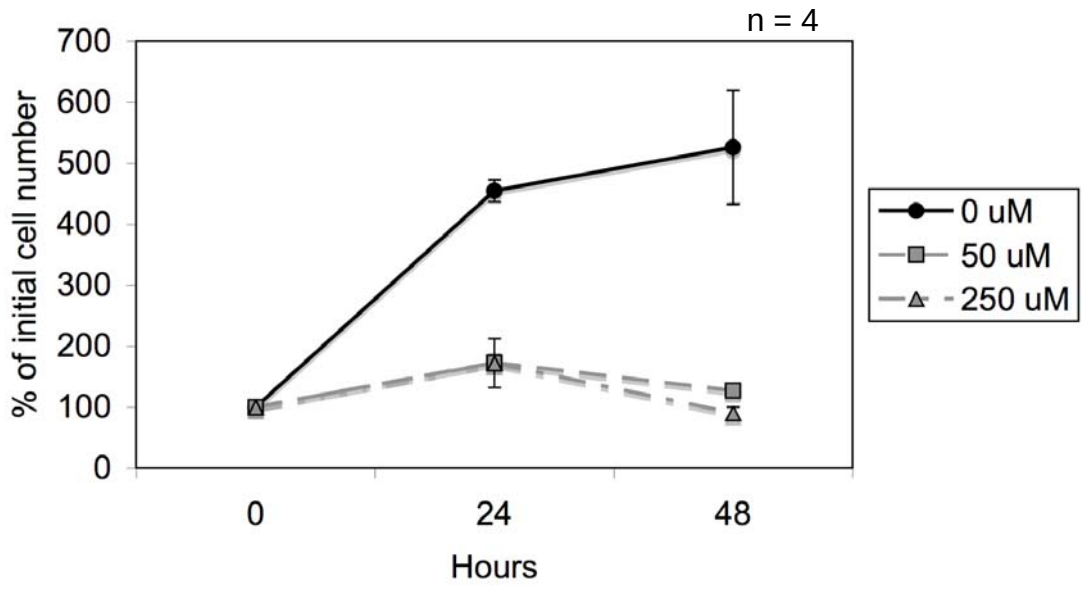
n = 4
700
600
500
400
300
200
100
0
% of initial cell number
0
24
48
Hours
0 uM
50 uM
250 uM

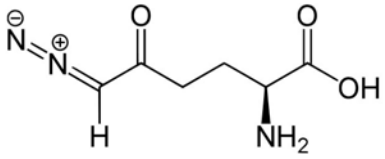
O
O
OH
H
NH2

DON

Figure 38. Experimental design. VM mice were implanted with the VM-M3/Fluc tumor tissue s.c. as described in Materials and Methods. DON administration began on day 5. Organs were removed 15-19 days post implantation and imaged *ex vivo.*

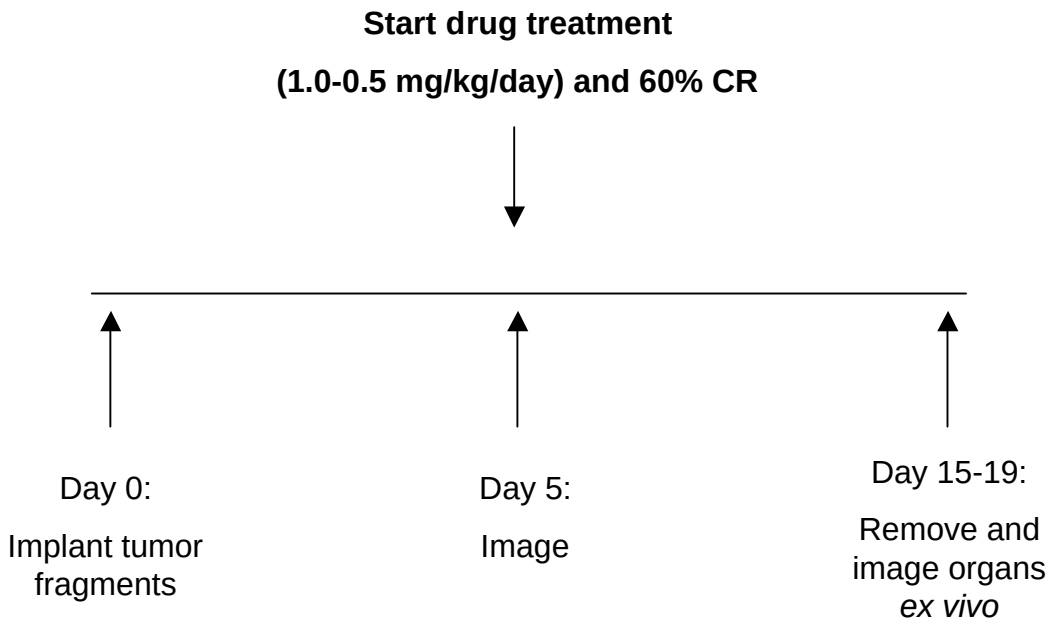
Start drug treatment
(1.0-0.5 mg/kg/day) and 60% CR
Day 0:
Implant tumor fragments
Day 5:
Image
Day 15-19:
Remove and image organs *ex vivo*

Figure 39. Effect of DON and DON + CR on VM-M3/Fluc tumor bearing mice. VM mice were implanted with the VM-M3/Fluc tumor s.c. as described in the Materials and Methods. **(A)** Body weights were monitored daily. Mice were sacrificed 15-19 days post implantation and blood was collected for the analysis of glucose **(B)** and ketone **(C)** levels as described in the Materials and Methods. All values represent the mean ± SEM. The DON + CR values differed significantly from the values of the AL control group at $*p < 0.05$, $**p < 0.01$. The ‡ indicates that the DON + CR values differed significantly from the values of the DON group at a $p < 0.01$.

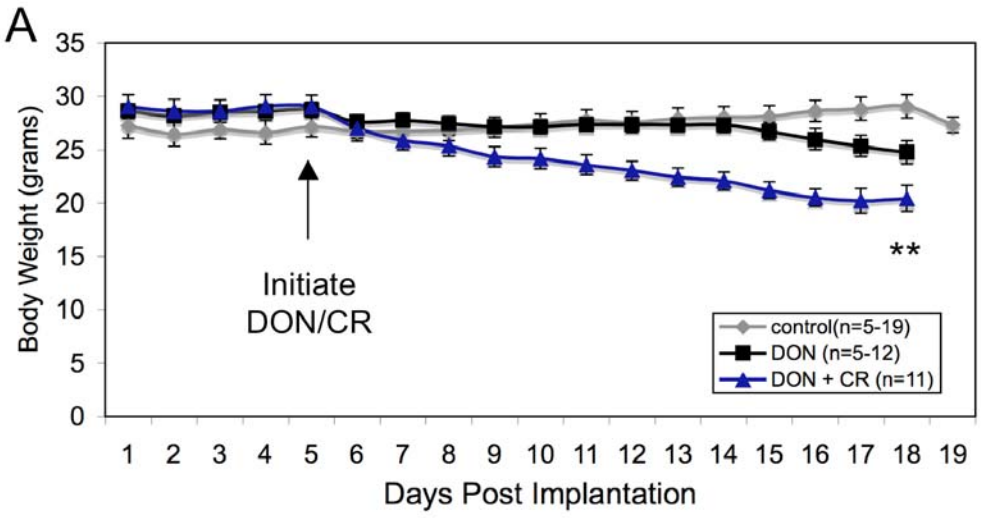
A
Body Weight (grams)
35
30
25
20
15
10
5
0
Initiate
DON/CR
**
control(n=5-19)
DON (n=5-12)
DON + CR (n=11)
1 2 3 4 5 6 7 8 9 10 11 12 13 14 15 16 17 18 19
Days Post Implantation

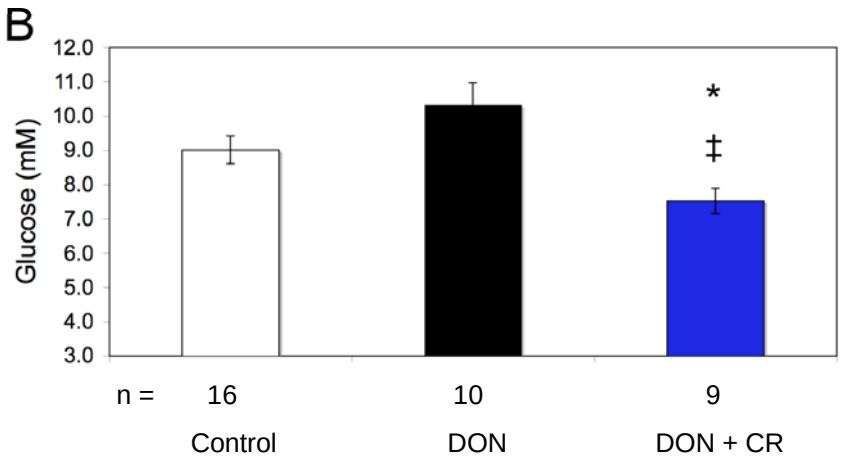
B
Glucose (mM)
12.0
11.0
10.0
9.0
8.0
7.0
6.0
5.0
4.0
3.0
*
‡
n = 16 10 9
Control
DON
DON + CR

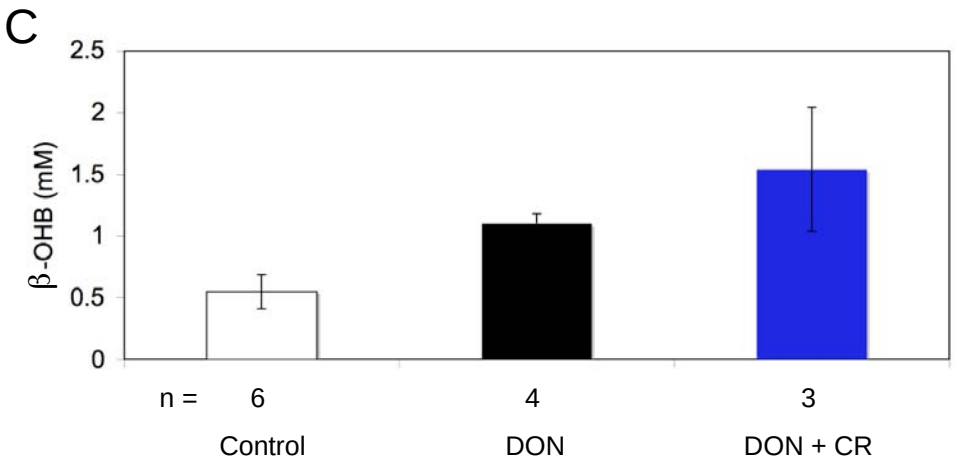
C
β-OHB (mM)
2.5
2
1.5
1
0.5
0
n = 6 4 3
Control
DON
DON + CR

Figure 40. Effect of DON and DON + CR on VM-M3/Fluc tumor growth. VM mice were implanted s.c. with the VM-M3/Fluc tumor as described in Materials and Methods. The mice were sacrificed 15-19 days post implantation and the tumors were removed and weighed. DON treatment in both groups resulted in an approximate 20-fold reduction in primary tumor size. The asterisks indicate that the DON or DON + CR values differ significantly from the AL control group at $p < 0.01$. Representative images are shown. The dotted line demarcates the tumor border.

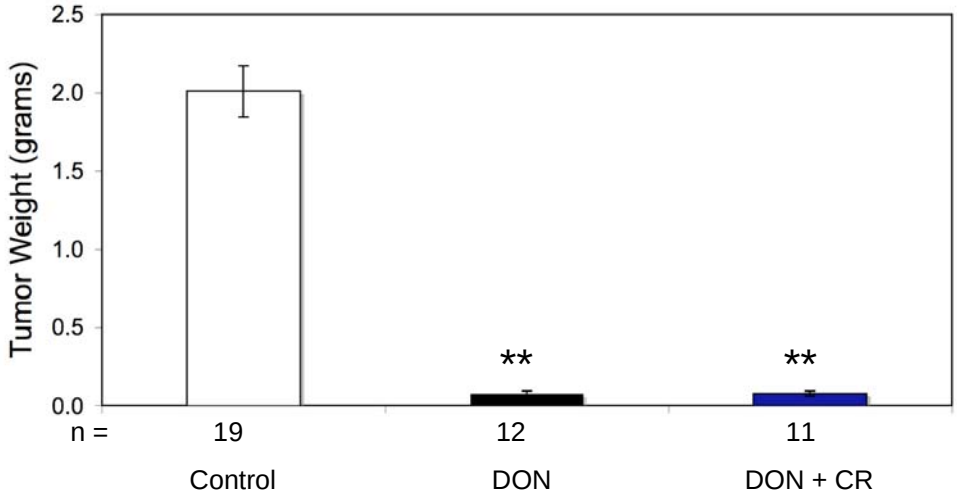

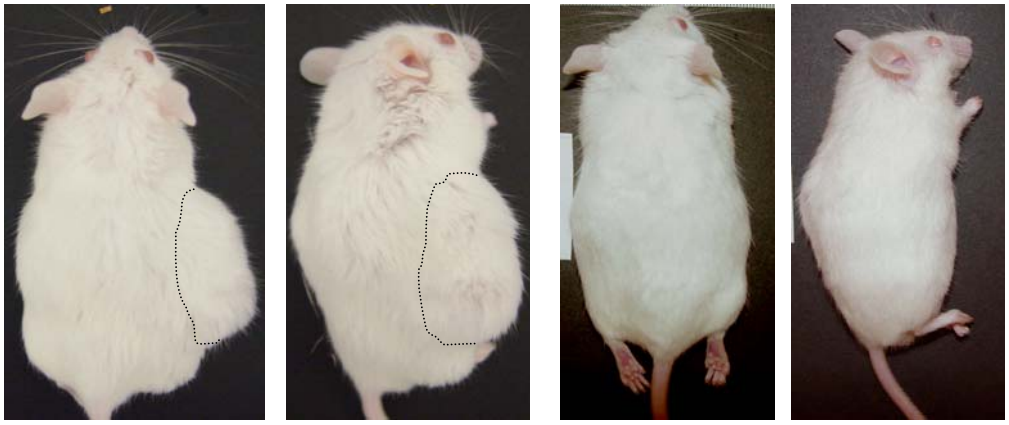

Control DON/DON + CR

Figure 41. Effect of DON and DON + CR on VM-M3/Fluc tumor metastasis. VM mice were implanted s.c. with the VM-M3/Fluc tumor as described in Materials and Methods. The organs were removed 15-19 days post implantation and imaged *ex vivo*. Bioluminescence values were plotted on a log scale. No detectable bioluminescence was found in the liver, lung, and kidney of mice treated with DON or DON + CR. All values represent the mean ± SEM.

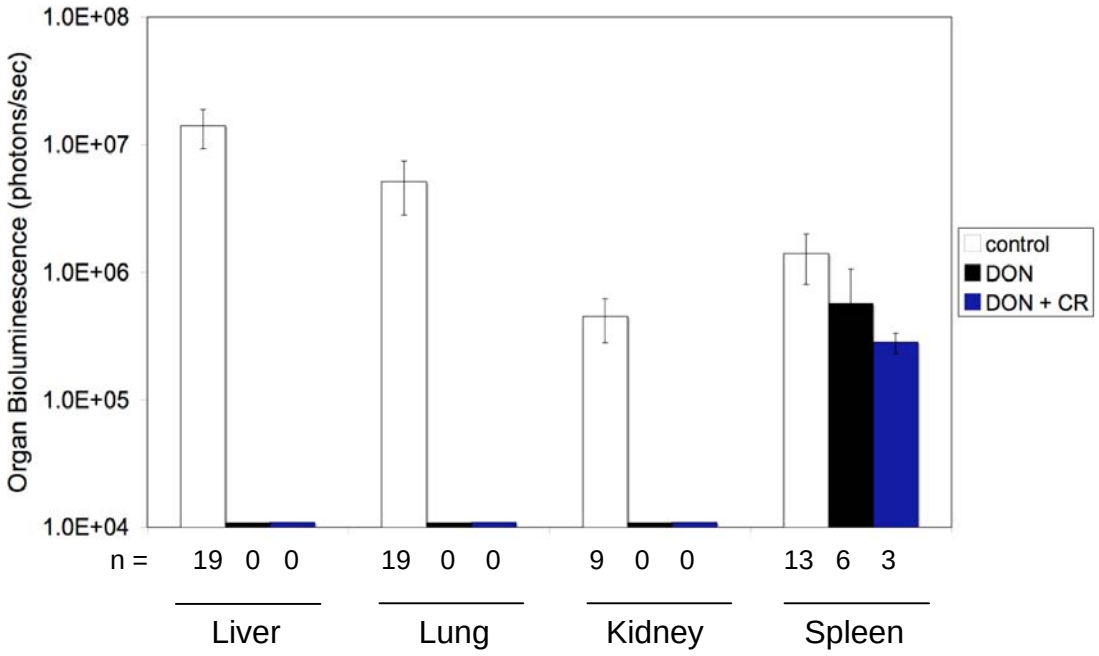
1.0E+08
1.0E+07
1.0E+06
1.0E+05
1.0E+04
Organ Bioluminescence (photons/sec)
control
DON
DON + CR
n = 19 0 0 19 0 0 9 0 0 13 6 3
Liver
Lung
Kidney
Spleen

Figure 42. Influence of DON and DON + CR on liver histology. VM mice were implanted s.c. with the VM-M3/Fluc tumor as described in Materials and Methods. Removed livers were stained with haematoxylin and eosin (H & E) as described in Materials and Methods. Arrows indicate secondary tumor lesions in the control untreated group only. Images are shown at 100X (top panel) and 200X (bottom panel). The liver from a non-tumor bearing mouse also served as a control.

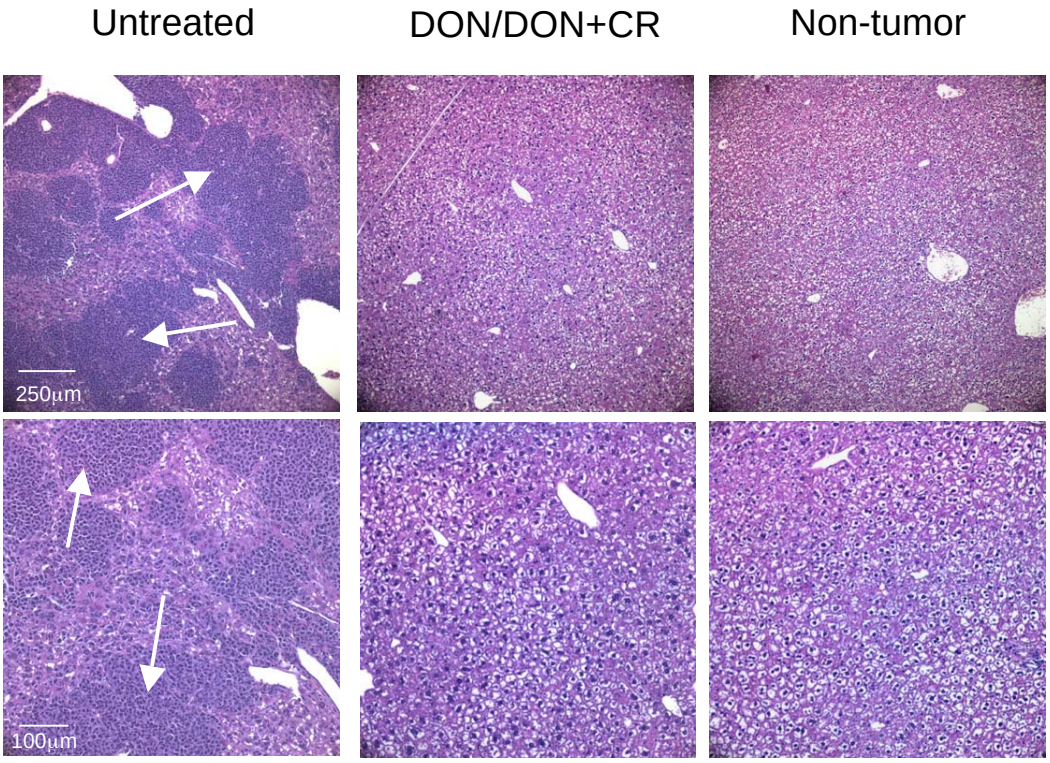
Untreated
DON/DON+CR
Non-tumor
250μm
100μm

Figure 43. Influence of DON and DON + CR on VM mouse survival. VM mice were implated s.c. with the VM-M3/Fluc tumor as described in Materials and Methods. All control mice reached morbidity 15-19 days post implantation. Both DON treated groups survived significantly longer than the controls. Survival was also significantly longer in mice treated with DON + CR than those treated with DON alone at a $p < 0.01$.

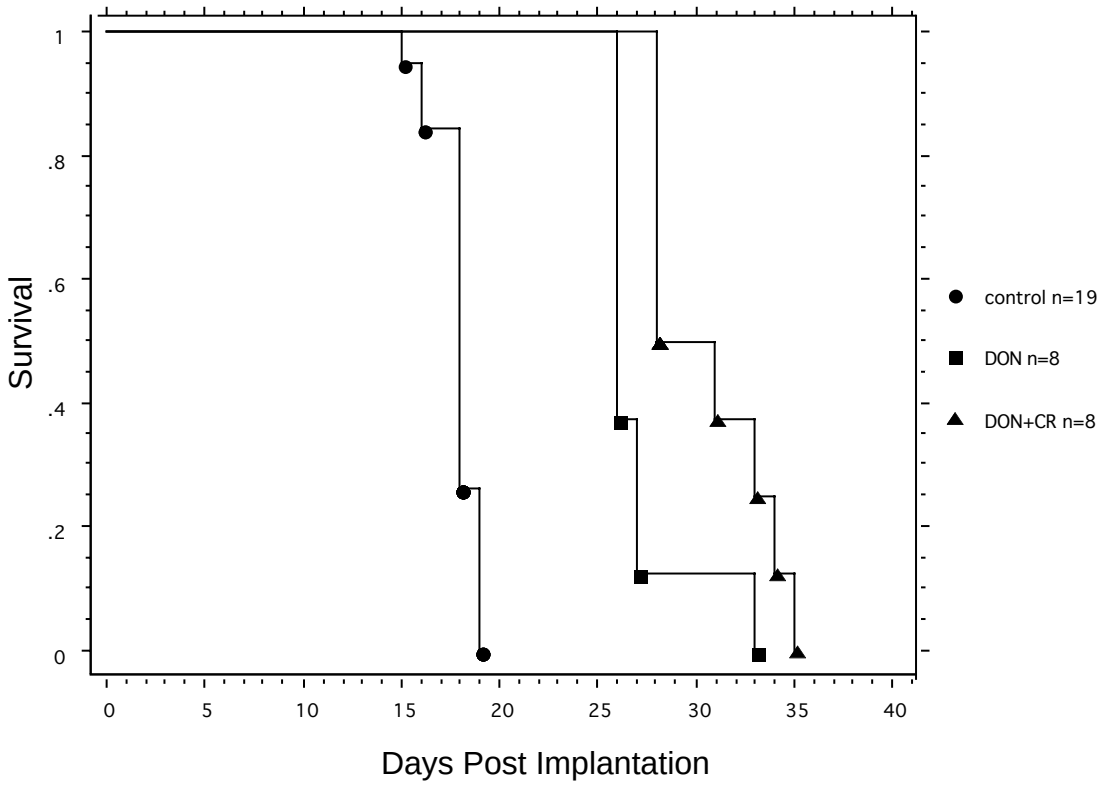
Survival
1
.8
.6
.4
.2
0
0
5
10
15
20
25
30
35
40
Days Post Implantation
control n=19
DON n=8
DON+CR n=8

Figure 44. Effect of Chloroquine (CQ) on VM-M3 and CT-2A cell viability *in vitro*. VM-M3/Fluc and CT-2A/Fluc cells were seeded in DMEM in 24 well plates as described in the Materials and Methods and treated with CQ (0-20 μM). Cells were imaged after 24 hours using the Xenogen IVIS system. VM-M3 cell viability was more sensitive to CQ treatment than were the CT-2A cells. Data are expressed as the mean percent increase in cell number relative to the non-drug control ± 95% C.I. of 4 independent samples per concentration.

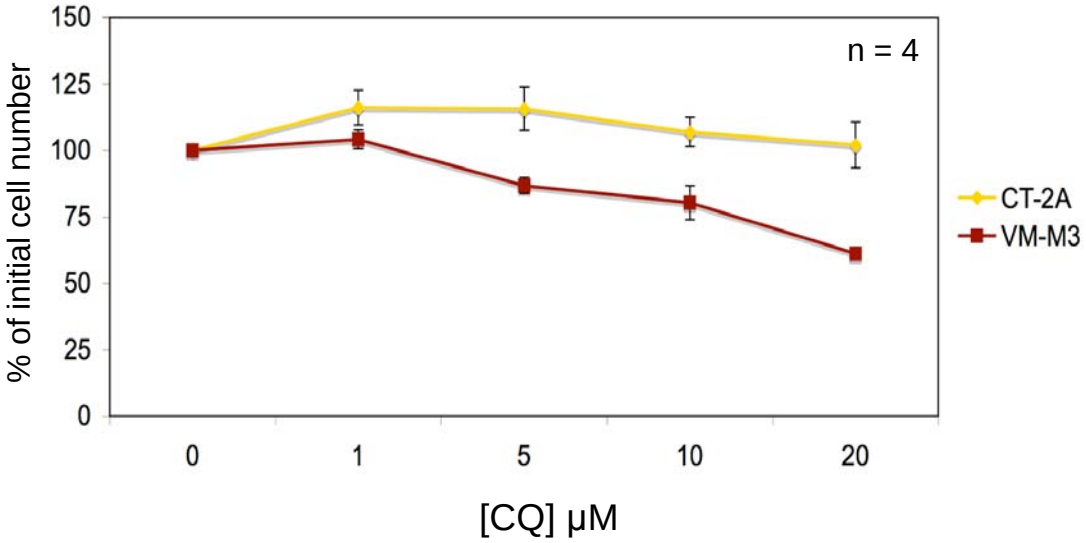

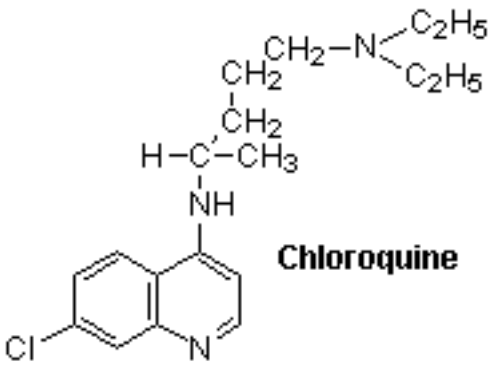

Chloroquine

Figure 45. ***In vitro*** **effect of Chloroquine on VM-M3 cell viability in Matrigel™ Matrix. (A)** VM-M3 cells were seeded in 24 well plates as described in Materials and Methods in the presence or absence of Matrigel™ Matrix (MG) ± 20 μM CQ in complete DMEM. Cell viability was assessed 24 hours later via bioluminescent imaging. VM-M3 cell viability was unaffected by CQ when in a complete media. Data are expressed as the mean percent increase in cell number relative to the 0 hr time point ± 95% C.I. of 3-6 independent samples per group. **(B)** Reduction in viability in VM-M3 cells when seeded in 5 mM glucose compared to complete DMEM (comp). Data are expressed as the mean percent increase in cell number relative to the 0 hr time point ± 95% C.I. of 6 independent samples per group. The asterisks indicate that viability in the glucose group differs significantly from the complete DMEM control group at $p < 0.01$.

A

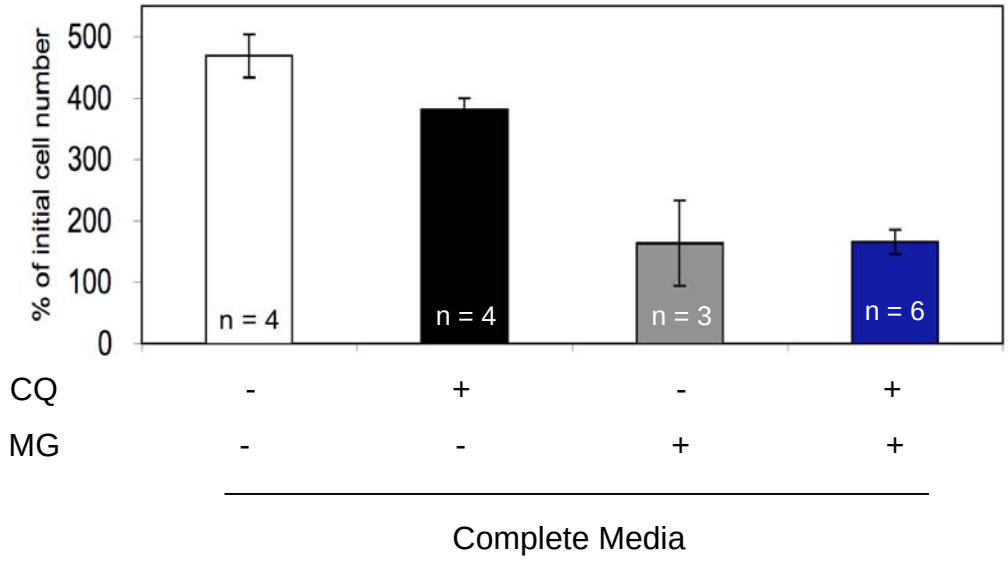
% of initial cell number
500
400
300
200
100
0
n = 4
n = 4
n = 3
n = 6
CQ - + - +
MG - - + +
Complete Media

B

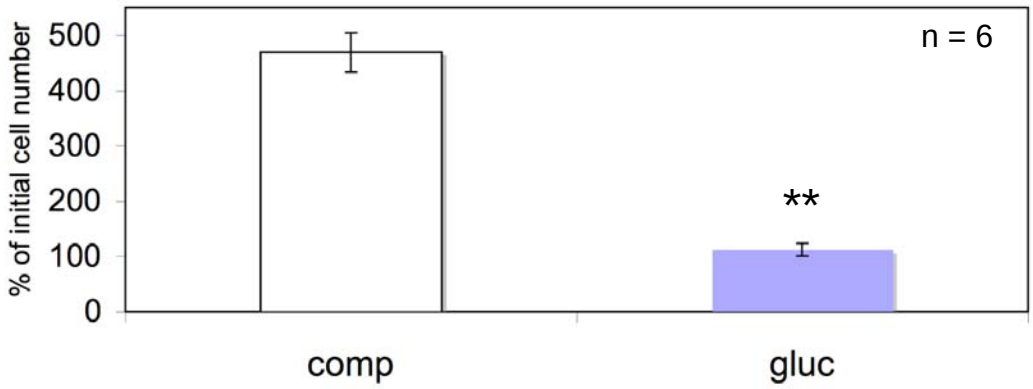
% of initial cell number
500
400
300
200
100
0
n = 6
**
comp
gluc

Figure 46. *In vitro* effect of Chloroquine and Matrigel™ Matrix on VM-M3 cell viability while under energy stress. VM-M3 cells were seeded in 24 well plates as described in Materials and Methods in the presence or absence of Matrigel™ Matrix ± 20 μM CQ in 5 mM glucose. Cell viability was assessed 24 hours later via bioluminescent imaging. VM-M3 cell viability was significantly enhanced by the presence of the Matrigel™ Matrix. CQ treatment resulted in near complete VM-M3 cell death. Data are expressed as the mean percent increase in cell number relative to the 0 hr time point ± 95% C.I. of 6 independent samples per group. The asterisk indicates that the Matrigel™ values differ significantly from the non-matrigel™ control group at $p < 0.05$.

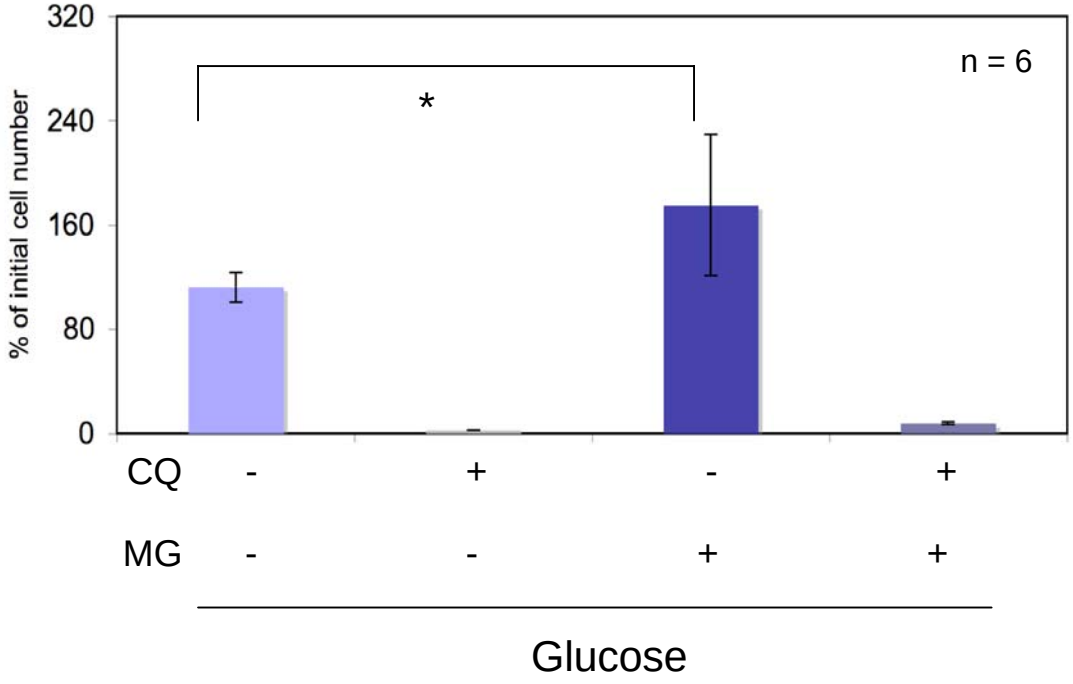
320
240
160
80
0
% of initial cell number
n = 6
*
CQ - + - +
MG - - + +
Glucose

Figure 47. Effect of Matrigel™ Matrix on VM-M3 lactate production under energy stress. VM-M3 cells were seeded as described in Figure 45. Media aliquots from each group were taken after 24 hours. Lactate accumulation was determined using an appropriate enzymatic assay. VM-M3 cells produced more lactate in the presence of the Matrigel™ Matrix. Values represent the mean ± 95% C.I. of 3 independent samples per group. The asterisk indicates that the gluc + Matrigel™ values differ significantly from the non-Matrigel™ gluc control group at $p < 0.05$.

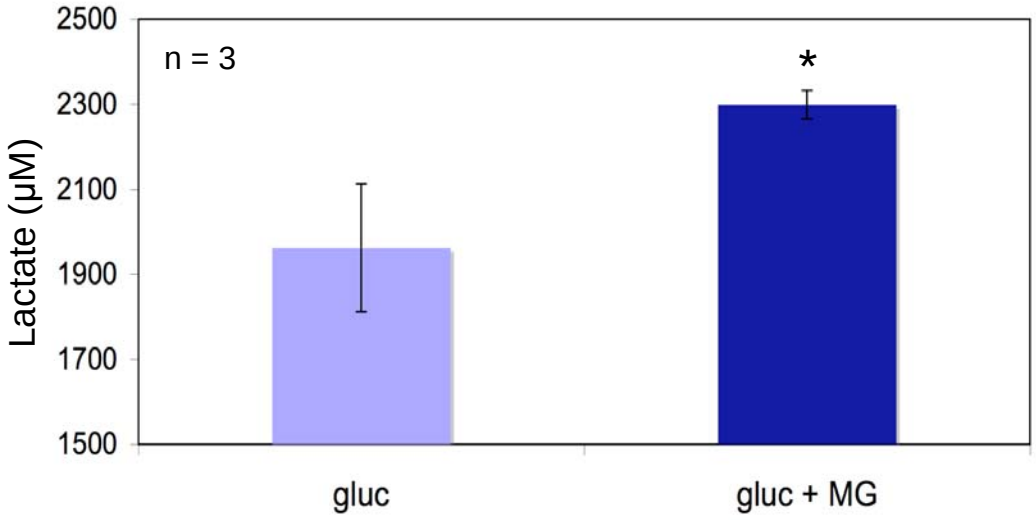
2500
2300
2100
1900
1700
1500
Lactate (µM)
n = 3
*
gluc
gluc + MG

Figure 48. ***In vitro*** **effect of Chloroquine on CT-2A cell viability in Matrigel™ Matrix. (A)** CT-2A cells were seeded in 24 well plates as described in Materials and Methods in the presence or absence of Matrigel™ Matrix ± 20 μM CQ in complete DMEM. Cell viability was assessed 24 hours later via bioluminescent imaging. CT-2A cell viability was unaffected by CQ treatment in complete media. Data are expressed as the mean percent increase in cell number relative to the 0 hr time point ± 95% C.I. of 3-6 independent samples per group. **(B)** Reduction in viability in CT-2A cells when seeded in 0.8 mM glutamine compared to complete DMEM (comp). Data are expressed as the mean percent increase in cell number relative to the 0 hr time point ± 95% C.I. of 6 independent samples per group. The asterisks indicate that viability in the glutamine group differs significantly from the complete DMEM control group at a $p < 0.01$.

A

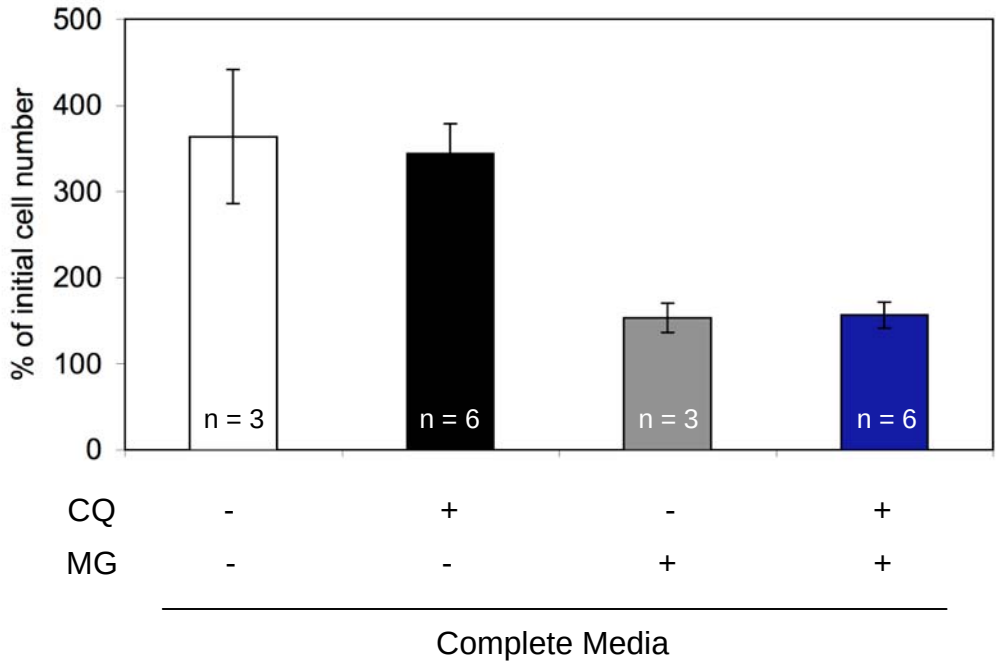
500
400
300
200
100
0
% of initial cell number
n = 3
n = 6
n = 3
n = 6
CQ - + - +
MG - - + +
Complete Media

B

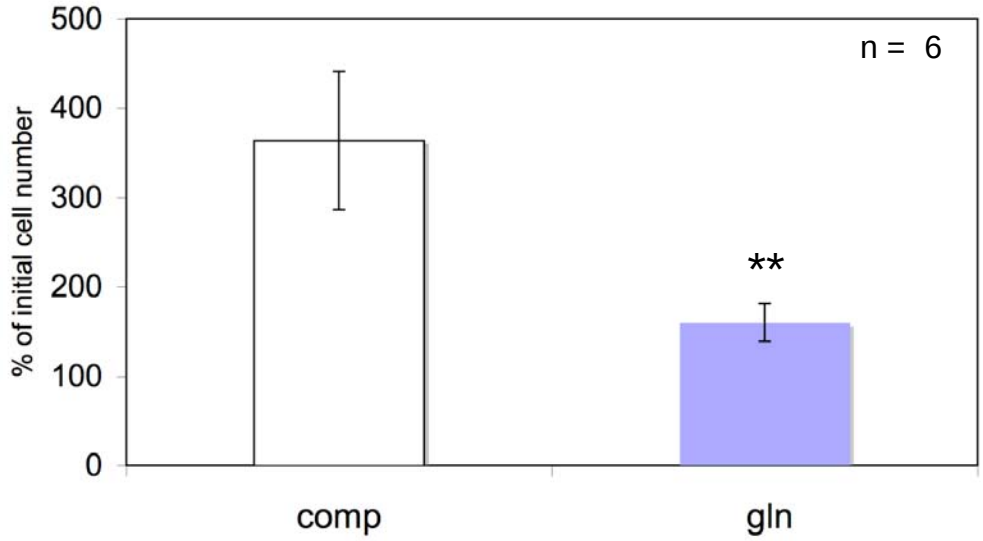
500
400
300
200
100
0
% of initial cell number
n = 6
**
comp
gln

Figure 49. *In vitro* effect of Chloroquine and Matrigel™ Matrix on CT-2A cell viability while under energy stress. CT-2A cells were seeded in 24 well plates as described in Materials and Methods in the presence or absence of Matrigel™ Matrix ± 20 μM CQ in 0.8 mM glutamine. Cell viability was assessed 24 hours later via bioluminescent imaging. CT-2A cell viability was not enhanced by the presence of the Matrigel™ Matrix. Data are expressed as the mean percent increase in cell number relative to the 0 hr time point ± 95% C.I. of 6 independent samples per group.

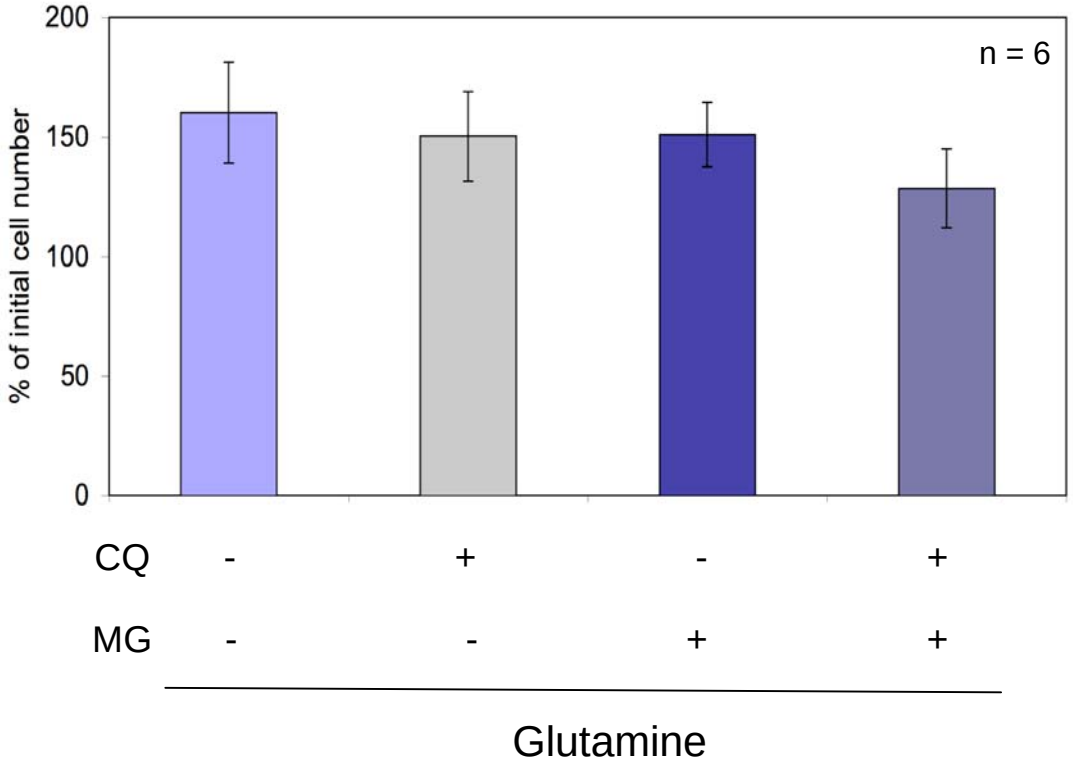
200
150
100
50
0
% of initial cell number
n = 6
CQ - + - +
MG - - + +
Glutamine

Figure 50. Phagocytic behavior of the VM-M3 cell line. Phagocytosis was determined as described in the Materials and Methods. Phagocytic behavior was assessed from merging (Merge) the fluorescence (GFP) and the differential interference contrast (DIC) images. The non-opsonized fluorescent beads were engulfed (phagocytosed) by the VM-M3 cells.

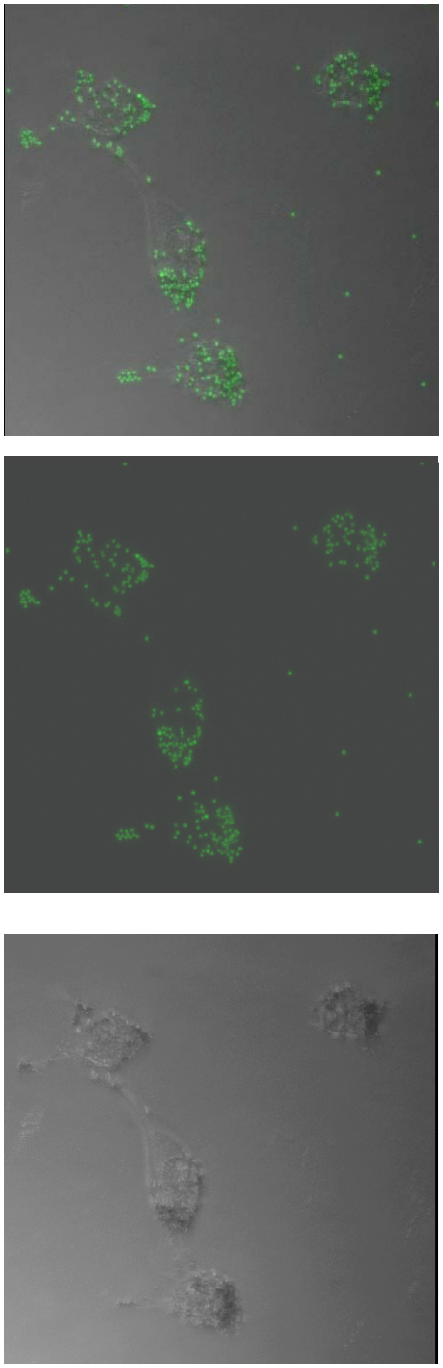
Merge
GFP
DIC

Figure 51. Effect of collagen coated latex beads on VM-M3 viability under energy stress. VM-M3 cells were seeded as described in the Materials and Methods in the presence of non-coated (LB) or collagen coated (LB + Col) latex beads in 5 mM glucose. After 24 hours cell viability was assessed via bioluminescent imaging. VM-M3 cell viability was enhanced in the presence of the collagen coated latex beads. Data are expressed as the mean percent increase in cell number relative to the 0hr time point ± 95% C.I. of 4 independent samples. The asterisks indicate that viability in the collagen-coated group differs significantly from the non-coated control group at $p < 0.01$.

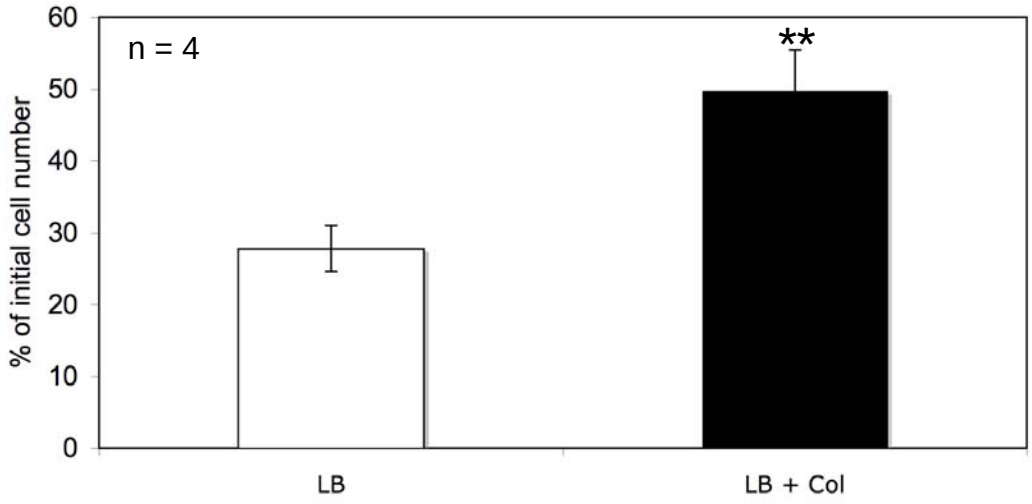
n = 4
**
% of initial cell number
60
50
40
30
20
10
0
LB
LB + Col

Figure 52. Effect of collagen coated latex beads on VM-M3 lactate and ammonia production under energy stress. VM-M3 cells were seeded as described in Figure 50. Media aliquots from each group were taken after 24 hours. Lactate and ammonia accumulation was determined using an appropriate enzymatic assay. Values represent the mean ± 95% C.I. of 3 independent samples per group. There is no statistically significant difference between the two groups for either lactate or ammonia values.

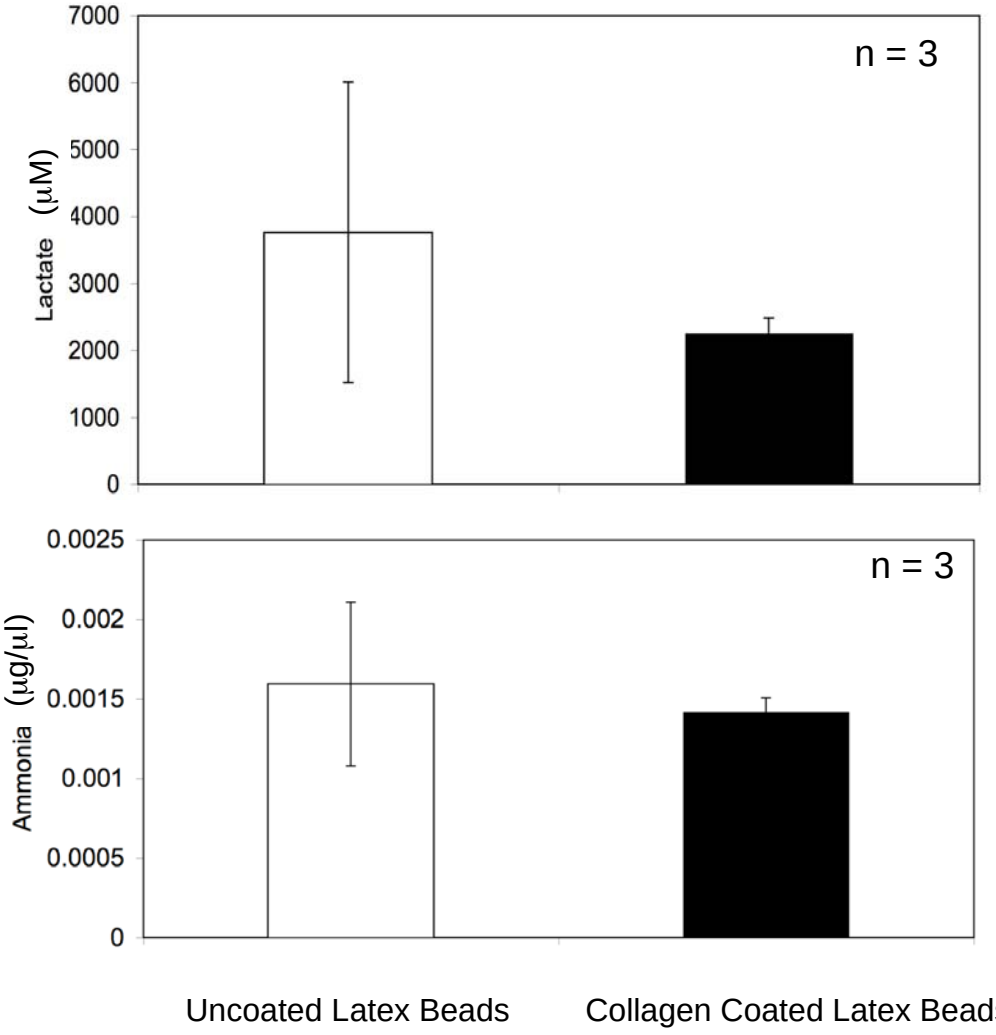
7000
6000
5000
4000
3000
2000
1000
0
Lactate (μM)
n = 3
0.0025
0.002
0.0015
0.001
0.0005
0
Ammonia (μg/μl)
n = 3
Uncoated Latex Beads
Collagen Coated Latex Beads

Figure 53. Experimental design. VM mice were implanted with VM-M3/Fluc tumor tissue s.c. as described in Materials and Methods. Chloroquine (CQ) administration, with or without a 60% calorie restriction (CR), began on day 4-6. Organs were removed 18-20 days post implantation and imaged *ex vivo*.

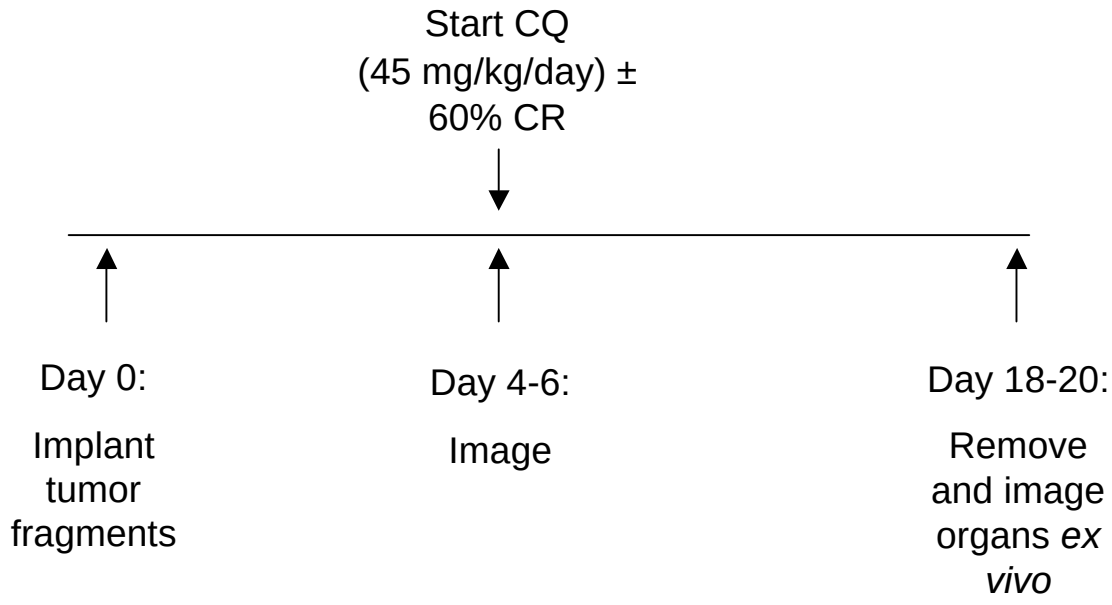
Start CQ
(45 mg/kg/day) ±
60% CR
Day 0:
Implant tumor fragments
Day 4-6:
Image
Day 18-20:
Remove and image organs *ex vivo*

Figure 54. Effect of Chloroquine on VM-M3/Fluc primary tumor size. VM mice were implanted s.c. with VM-M3/Fluc tumor tissue as described in Materials and Methods. Mice were sacrificed 18-20 days post implantation and the tumor was removed and weighed. Values represent the mean ± SEM of 6 mice per group. There is no statistically significant difference between the two groups.

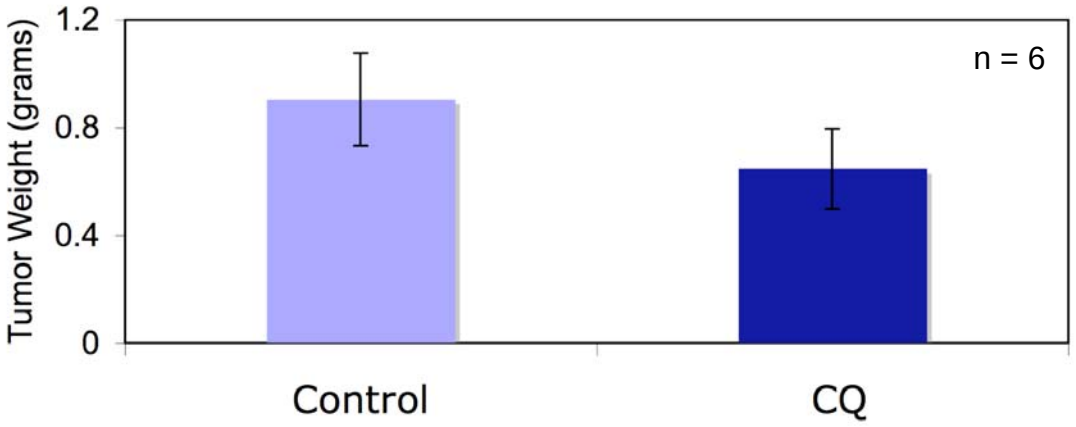
Tumor Weight (grams)
1.2
0.8
0.4
0
n = 6
Control
CQ

Figure 55. Effect of Chloroquine on VM-M3/Fluc tumor metastasis. VM mice were implanted s.c. with VM-M3/Fluc tumor tissue as described in Materials and Methods. Organs were removed 18-20 days post implantation and imaged *ex vivo.* Bioluminescence values were plotted on a log scale. Values represent the mean ± SEM of 6 mice per group. There is no statistically significant difference between the two groups.

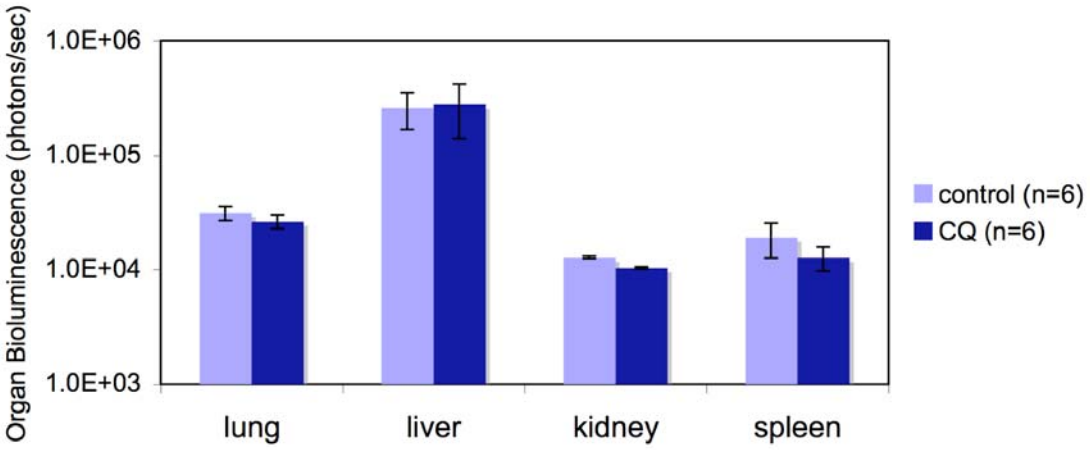
Organ Bioluminescence (photons/sec)
1.0E+06
1.0E+05
1.0E+04
1.0E+03
lung
liver
kidney
spleen
control (n=6)
CQ (n=6)

Figure 56. Effect of Chloroquine and CR on VM-M3/Fluc primary tumor size. VM mice were implanted s.c. with VM-M3/Fluc tumor tissue as described in Materials and Methods. Mice were sacrificed 18-20 days post implantation and the tumor was removed and weighed. Values represent the mean ± SEM of 5-6 mice per group. There is no statistically significant difference between the CR and CR + CQ groups.

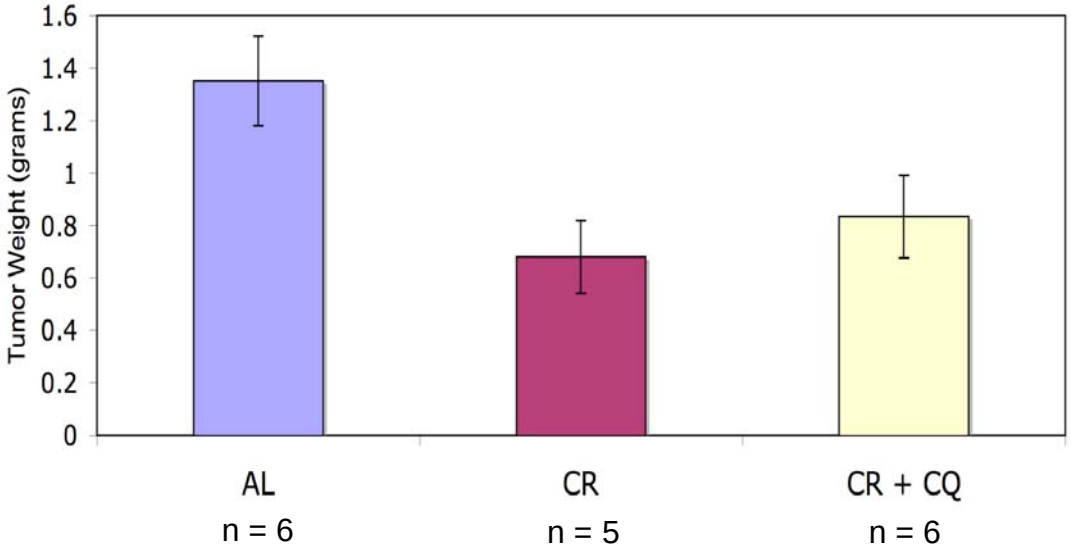
Tumor Weight (grams)
1.6
1.4
1.2
1
0.8
0.6
0.4
0.2
0
AL
n = 6
CR
n = 5
CR + CQ
n = 6

Figure 57. Effect of Chloroquine and CR on VM-M3/Fluc tumor metastasis. VM mice were implanted s.c. with VM-M3/Fluc tumor tissue as described in Materials and Methods. Organs were removed 18-20 days post implantation and imaged *ex vivo.* Bioluminescence values were plotted on a log scale. Values represent the mean ± SEM of 5-6 mice per group. There is no statistically significant difference between the CR and CR + CQ groups.

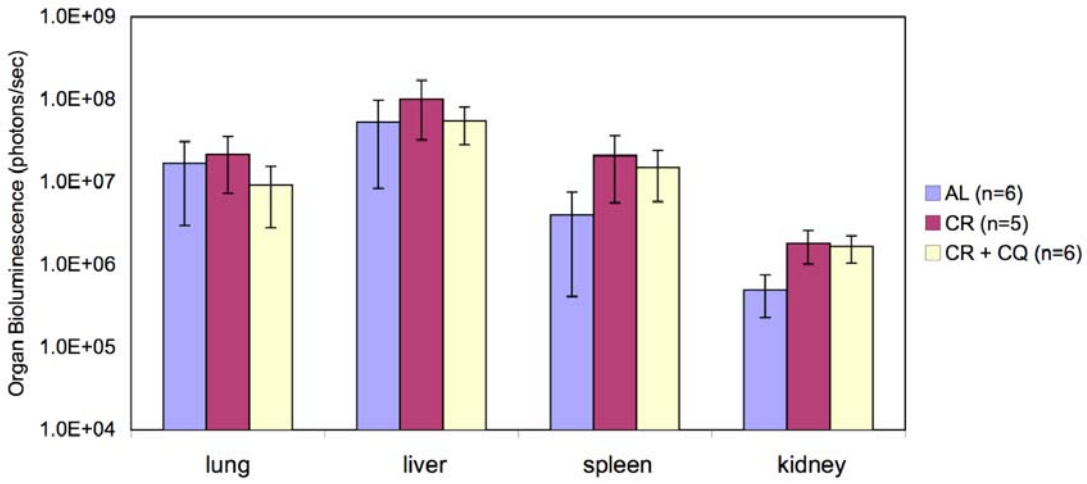
1.0E+09
1.0E+08
1.0E+07
1.0E+06
1.0E+05
1.0E+04
Organ Bioluminescence (photons/sec)
lung
liver
spleen
kidney
AL (n=6)
CR (n=5)
CR + CQ (n=6)

Figure 58. Experimental Design. VM mice were implanted with VM-M3/Fluc tumor tissue i.c. as described in Materials and Methods. Chloroquine (CQ) administration, with or without a 60% calorie restriction (CR), began on day 4-6. Brains were removed 12-15 days post implantation and imaged *ex vivo*.

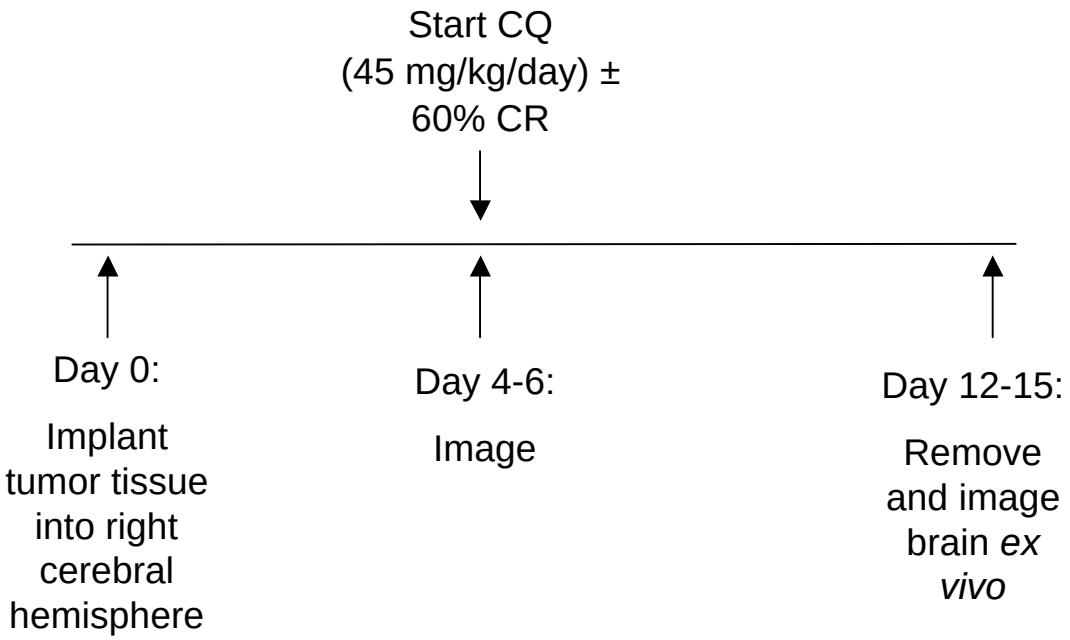
Start CQ
(45 mg/kg/day) ±
60% CR
Day 0:
Implant tumor tissue into right cerebral hemisphere
Day 4-6:
Image
Day 12-15:
Remove and image brain *ex vivo*

Figure 59. Effect of Chloroquine on VM-M3/Fluc brain tumor growth and invasion. VM mice were implanted with VM-M3/Fluc tumor tissue i.c. as described in Materials and Methods. Brains were removed 12-15 days post implantation and sectioned down the midline. Ipsilateral and contralateral hemispheres were imaged *ex vivo*. Bioluminescence was plotted on a log scale. Values represent the mean ± SEM of 4-5 mice per group. There is no statistically significant difference between the two groups for either hemisphere.

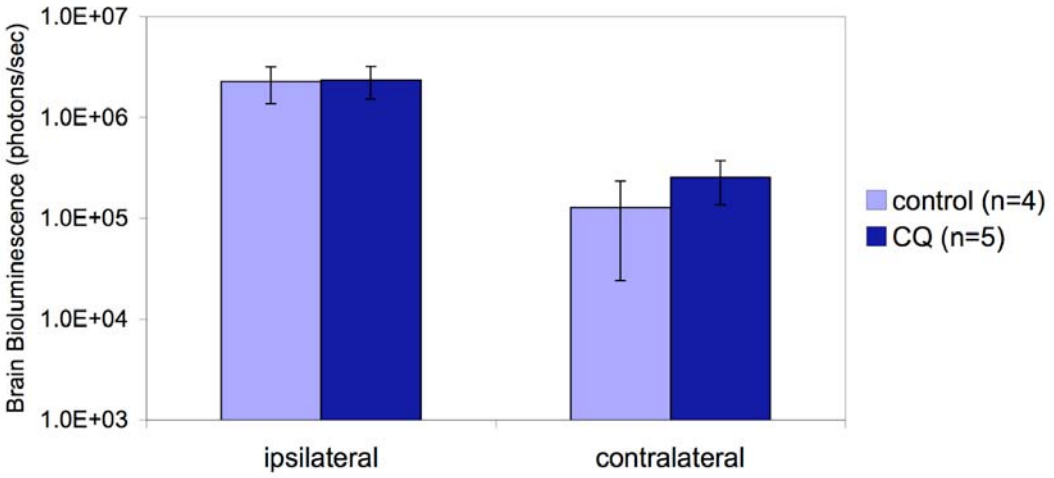
Brain Bioluminescence (photons/sec)
1.0E+07
1.0E+06
1.0E+05
1.0E+04
1.0E+03
ipsilateral
contralateral
control (n=4)
CQ (n=5)

Figure 60. Effect of Chloroquine and CR on VM-M3/Fluc brain tumor growth and invasion. VM mice were implanted with VM-M3/Fluc tumor tissue i.c. as described in Materials and Methods. Brains were removed 12-15 days post implantation and sectioned down the midline. Ipsilateral and contralateral hemispheres were imaged *ex vivo*. Bioluminescence was plotted on a log scale. Values represent the mean ± SEM of 4-7 mice per group. There is no statistically significant difference between the CR and CR + CQ groups for either hemisphere. The asterisk indicates that the values for the contralateral hemisphere from the CR + CQ group differs from the AL control group at a $p < 0.05$.

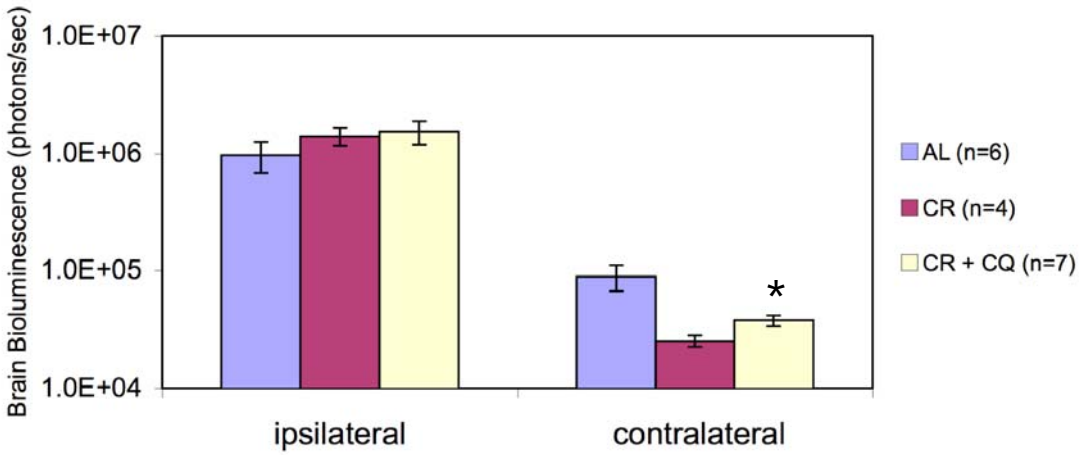
Brain Bioluminescence (photons/sec)
1.0E+07
1.0E+06
1.0E+05
1.0E+04
ipsilateral
contralateral
*
AL (n=6)
CR (n=4)
CR + CQ (n=7)

Table 1: Percentage of animals with metastasis to organs[a]

Group (n)	liver	lung	kidney	spleen
AL (24)	100	100	46	63
CR (10)	100	90	50	80

[a] The presence of metastasis was detected with bioluminescence imaging.

Table 2: Percentage of animals with metastasis to organs[a]

Group (n)	liver	lung	kidney	spleen
control (19)	100	100	47	68
DON (12)	0 *	0 *	0 *	50
DON + CR (11)	0 *	0 *	0 *	27 *

[a] The presence of metastasis was detected with bioluminescence imaging.

* The asterisk indicates that the DON or DON + CR group is significantly less than the control group as calculated by chi square analysis at the $p<0.01$ level.

Supplemental Figure 1. Ketone transitioned astrocytes in culture. Astrocytes were transitioned to a low glucose high ketone media as described in the Materials and Methods. Images were taken approximately 30 days after the start of ketone transitioning. Images are taken at 200X.

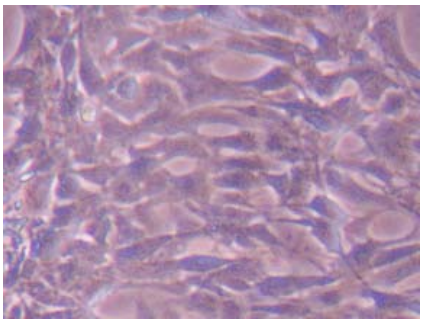

+ β-OHB

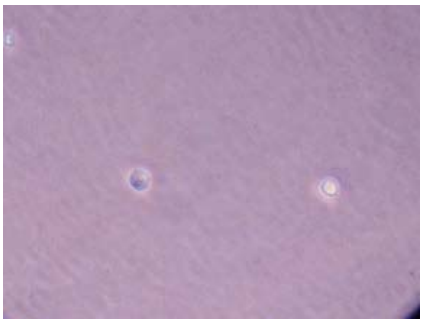

- β-OHB

Supplemental Figure 2. Effect of Phenylbutyrate (PBA) on VM-M3 cell viability *in vitro*. VM-M3/Fluc cells were seeded in DMEM in 24 well plates as described in the Materials and Methods and treated with PBA (0-100 mM). Cells were imaged after 24 hours using the Xenogen IVIS system. VM-M3 cell viability was inhibited in a dose dependent manner. Data are expressed as the mean percent increase in cell number relative to the non-drug control ± 95% C.I. of 4 independent samples per concentration.

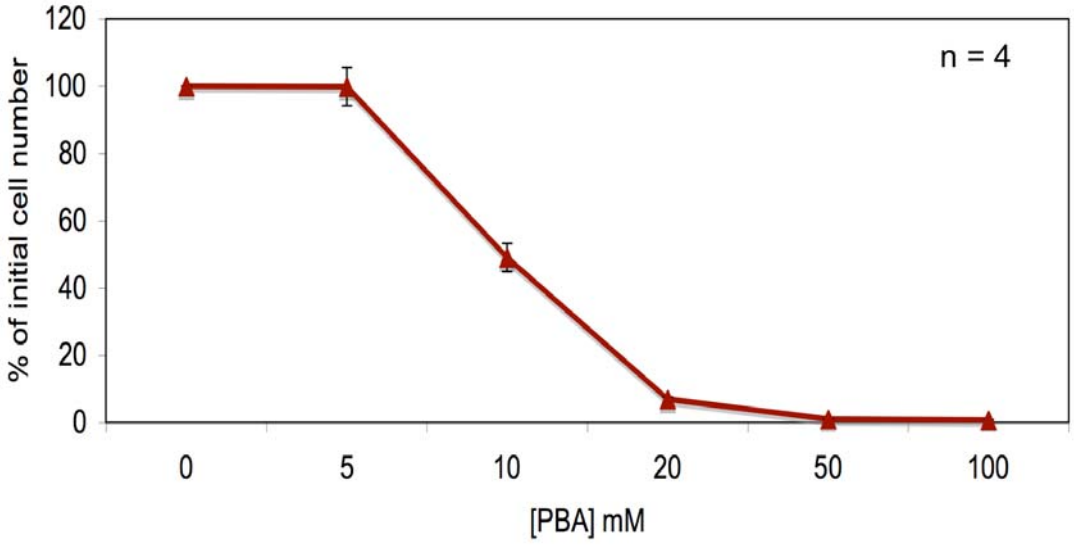
120
100
80
60
40
20
0
% of initial cell number
n = 4
0
5
10
20
50
100
[PBA] mM

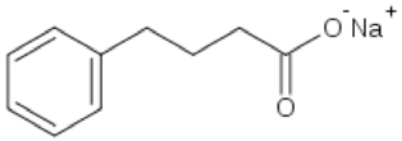
O
Na
O

PBA

Supplemental Figure 3. Schematic representation of metabolic pathways. Illustrated are the glucose and glutamine utilizing metabolic pathways of glycolysis and glutaminolysis respectively. Reactions of the TCA cycle take place in the mitochondrial matrix while reactions of the ETC take place in the inner mitochondrial membrane. Various metabolic inhibitors and their sites of inhibition are illustrated. Abbreviations; 3-NP; 3-Nitropropionic acid; ATP, adenosine tri-phosphate; ETC, electron transport chain, $FADH_2$, flavin adenine dinucleotide (reduced form); GTP, guanosine tri-phosphate; *meso, meso*-Tartrate; NADH, nicotinamide adenine dinucleotide (reduced form); Oligo, Oligomycin; TCA, tri-carboxylic acid cycle.

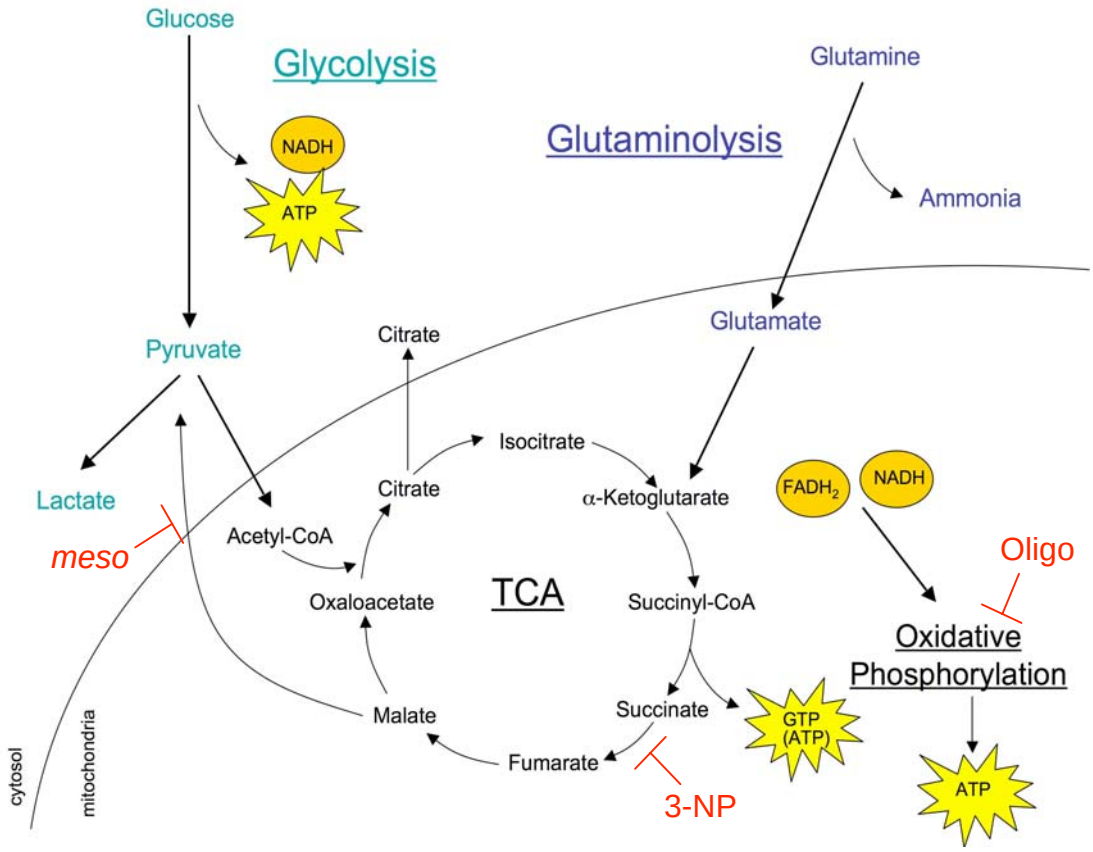
Glucose
Glycolysis
NADH
ATP
Glutamine
Glutaminolysis
Ammonia
Pyruvate
Citrate
Glutamate
Isocitrate
Lactate
Citrate
α-Ketoglutarate
FADH2
NADH
meso
Acetyl-CoA
Oligo
Oxaloacetate
TCA
Succinyl-CoA
Oxidative
Phosphorylation
Succinate
GTP
(ATP)
Malate
Fumarate
3-NP
ATP
cytosol
mitochondria

Supplemental Figure 4. Proposed mechanism by which glutamine maintains viability in the VM-M3 cell line. Glutamine enters the TCA cycle as α-ketoglutarate generating energy from substrate level phosphorylation from the conversion of succinyl-CoA to succinate. Citrate from the TCA cycle is extruded from the mitochondria to the cytosol whereby it is converted to oxaloacetate (OAA) and acetyl-CoA. Acetyl-CoA is further used in fatty acid synthesis. OAA is converted to malate, which re-enters the mitochondria. Once in the mitochondria, mitochondrial malic enzyme (ME) converts malate to pyruvate, which is further converted to acetyl-CoA. Acetyl-CoA can now re-enter the TCA to allow for continued TCA cycling.

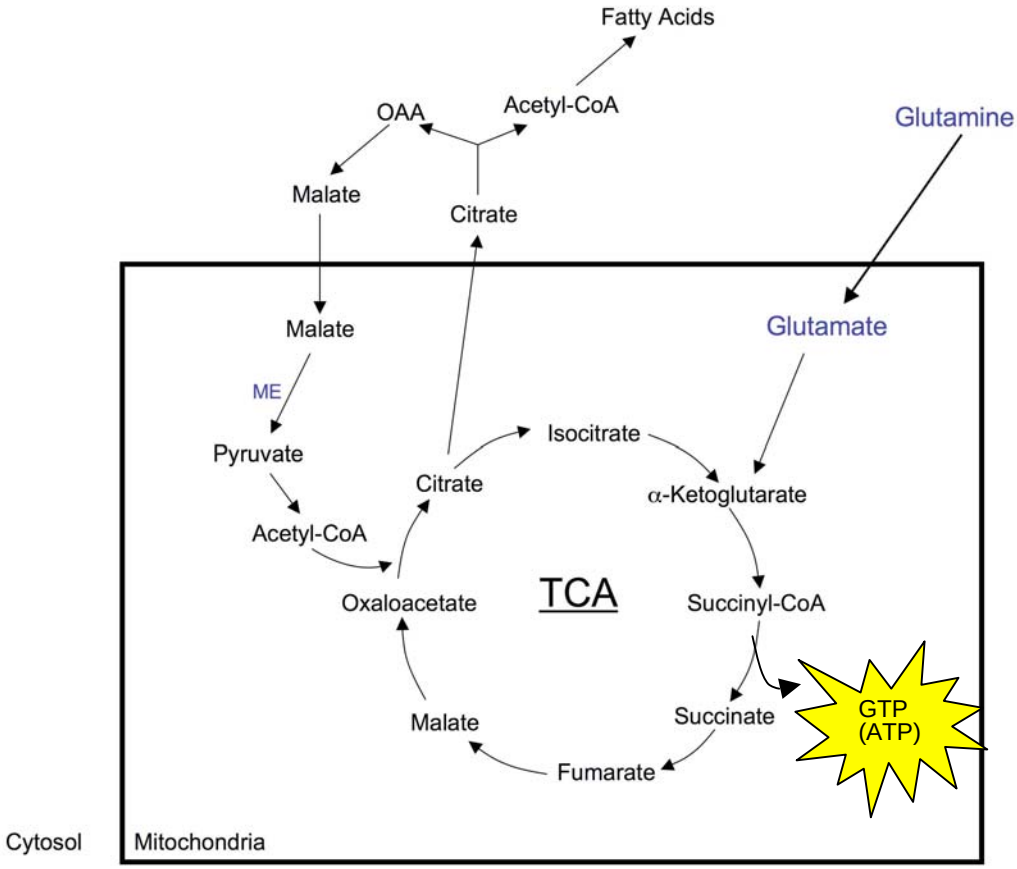
Fatty Acids
OAA
Acetyl-CoA
Glutamine
Malate
Citrate
Malate
Glutamate
ME
Pyruvate
Isocitrate
Citrate
α-Ketoglutarate
Acetyl-CoA
TCA
Oxaloacetate
Succinyl-CoA
GTP
(ATP)
Succinate
Malate
Fumarate
Cytosol
Mitochondria

Supplemental Figure 5. Correlation between ATP concentration, VM-M3 cell number and bioluminescence. ATP **(A)** and VM-M3 cells **(B)** were assayed for bioluminescence as described in the Materials and Methods.

A

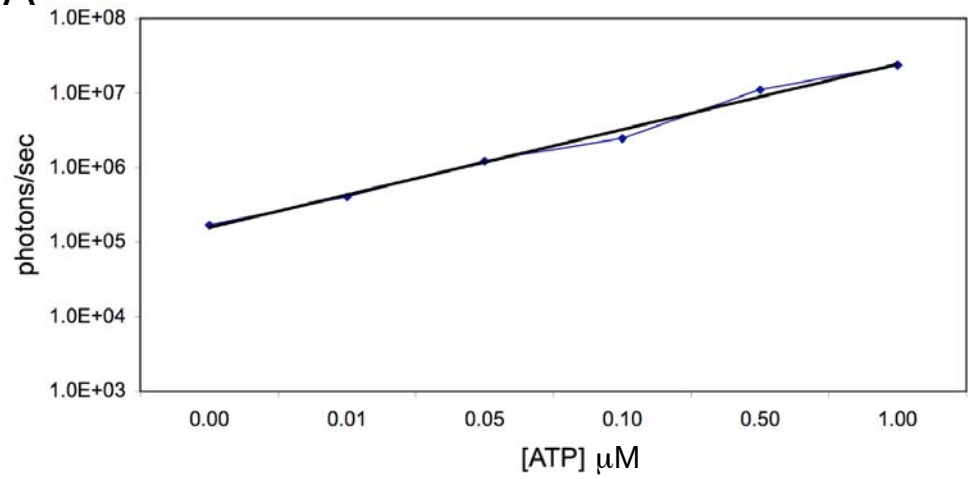
1.0E+08
1.0E+07
1.0E+06
1.0E+05
1.0E+04
1.0E+03
photons/sec
0.00
0.01
0.05
0.10
0.50
1.00
[ATP] μM

B

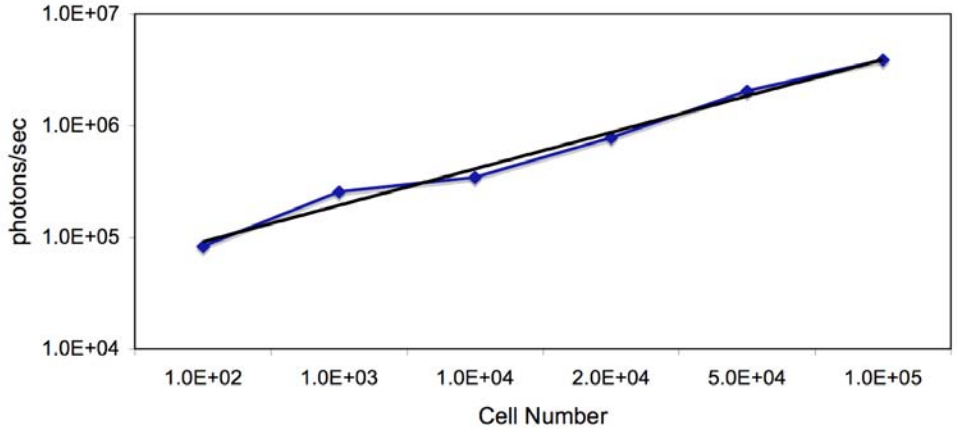
1.0E+07
1.0E+06
1.0E+05
1.0E+04
photons/sec
1.0E+02
1.0E+03
1.0E+04
2.0E+04
5.0E+04
1.0E+05
Cell Number

DISCUSSION

First, I present a novel *in vivo* model for brain tumor growth and invasion. Most available brain tumor models fall short of fully recapitulating all major characteristics of human GBM. An accurate *in vivo* model is necessary for the development of therapies that can target both local and distant tumor cell invasion. To date, no xenograft model or chemically induced rodent model displays the invasive characteristics of the VM-M3 model, to include sub-pial and ventricular spread, perivascular, perineuronal, peri- and intra-fascicular growth, and inter-hemispheric invasion. These routes of invasion have been referred to as the Secondary Structures of Scherer (Scherer 1938; Rubinstein 1972). These structures were identified in highly invasive human brain tumors to include GBM, astrocytoma, and oligodendroglioma (Scherer 1938, 1940a). The secondary structures described the growth of invasive tumor cells along the pre-existing structures of the nervous system and were independent of histological grade or classification (Scherer 1938, 1940a). This is important as histological classification of brain tumors can be ambiguous at best (Scherer 1940b).

Although the murine GL261 glioma model also displays several invasive qualities of the VM-M3 brain tumor model, it does not express ventricular and inter-hemispheric spread and the invasive phenotype is limited to the invading edge of the tumor (Zagzag et al. 2008). Additional advantages of the VM-M3 model include rapid and consistent growth patterns both *in vivo* and *in vitro,* a syngeneic host, and low immunogenicity as illustrated by robust growth at subcutaneous implantation sites (Huysentruyt et al. 2008;

Huysentruyt et al. 2010). *In vitro,* the cells express two primary morphologies, which are cell cycle dependent. During division, the cells are small and round, but become flat and pancake shaped during the resting state as we previously described (Huysentruyt et al. 2008; Huysentruyt et al. 2010). Though the VM-M3 cells predominately display the small and round morphology *in vivo*, additional pleomorphic cells are found throughout the tumor consistent with the cellular morphologies seen human GBM (Rubinstein 1972). VM-M3 cell growth and morphology is also consistent over multiple passages both *in vivo* and *in vitro*. The VM-M3 model is therefore unique in its ability to fully replicate the growth and invasive patterns of human GBM.

In addition to the similarities in growth, cell morphology, and invasion, the VM-M3 tumor also had genetic similarities with human GBM. Along with CXCR4 and Ki-67, a number of genetic markers have been linked to the invasive and aggressive phenotype of human GBM (Hoelzinger et al. 2005; Li et al. 2009). Interestingly, insulin-like growth factor binding protein 2 (IGFBP-2) is known to be upregulated in human GBM (Fuller et al. 1999; Rickman et al. 2001). However, a more specific analysis revealed that IGFPB-2 is highly expressed in the cells of the tumor core, but is significantly down regulated in the cells along the invasive edge, suggesting that there is a distinct molecular signature in the invasive versus non-invasive cells within the same tumor (Hoelzinger et al. 2005). I showed that the IGFBP-2 gene was highly expressed in the cells of the VM-NM1 tumor, which grows more rapidly but is less invasive than the VM-M3 tumor (Huysentruyt et al. 2008). Our findings are consistent with those of a previous study showing IGFBP-2

expression in the core tumor cells of a GBM (Hoelzinger et al. 2005). However, expression of IGFBP-2 was low in the VM-M3 invasive tumor cells, consistent with the expression profile of the invasive rim of human GBM (Hoelzinger et al. 2005).

The VM-M3 tumor is labeled with the firefly luciferase gene allowing for non-invasive detection of tumor growth and invasion via bioluminescent imaging. Bioluminescent imaging has been established as an accurate tool for measuring tumor growth over time (Deroose et al. 2006; Szentirmai et al. 2006; Maes et al. 2008). As the VM-M3 tumor cells are invasive to all brain regions, I developed a novel bioluminescent-based quantitative assay for evaluating the extent of tumor invasion into the cortex, hippocampus, brain stem, and cerebellum. I showed that bioluminescence could be correlated with histological data on tumor growth and invasion. In contrast to histology, bioluminescent imaging is a more accurate measure of distal tumor cell invasion to multiple brain regions. This feature will allow for the quantitative assessment of potential therapies that target brain tumor invasion.

Calorie restriction has not been evaluated as an anti-invasive brain cancer therapy due to the lack of an invasive brain tumor model. I show that calorie restriction, which significantly reduces tumor growth and angiogenesis in the non-invasive murine CT-2A, EPEN, and human U87 experimental models (Mukherjee et al. 2002; Mukherjee et al. 2004; Zhou et al. 2007), is also capable of reducing tumor growth and invasion of our highly invasive VM-M3 tumor model. Studies in humans have since linked high

circulating glucose levels with a poor prognosis in patients diagnosed with GBM (McGirt et al. 2008; Derr et al. 2009). Additionally, a restricted ketogenic diet has been introduced into the clinical setting with positive results (Nebeling et al. 1995). Because most brain tumors are highly glycolytic, they rely heavily on glucose as a major energy source (Warburg 1956; Seyfried and Mukherjee 2005). Calorie restriction lowers circulating plasma glucose and targets those pathways associated with tumor glycolysis (Seyfried et al. 2003; Seyfried and Mukherjee 2005; Marsh et al. 2008b). In addition to reducing glucose, calorie restriction also elevates circulating ketone bodies that are metabolized by normal brain tissue (Seyfried and Mukherjee 2005; Zhou et al. 2007). Ketone body metabolism takes place in the mitochondria and provides non-glucose derived reducing equivalents for oxidative phosphorylation. The VM-M3 cell line however has alterations in both mitochondrial lipid composition and electron transport chain enzyme activities, which would compromise normal mitochondrial function (Kiebish et al. 2008b). In addition, the VM-M3 cell line was unable to transition to ketones under low glucose conditions *in vitro,* while normal astrocytes successfully grew under low glucose, high ketone conditions (Supplemental Figure 1). Ketones however were not toxic to the VM-M3 cell line *in vitro* and therefore, the increase in circulating ketones did not likely contribute to VM-M3 cell death under CR. We have also shown that a restricted ketogenic diet reduced HIF-1α and IGF-1 gene expression (Marsh et al. 2008b). Reductions in these signaling pathways as a result of calorie restriction also result in decreases in Akt and mTOR signaling, both of which are involved in tumor cell growth and metabolism (Marsh et al. 2008b; Moore et al. 2008). Here I show that calorie

restriction also significantly reduced the percentage of Ki-67 (+) tumor cells, an indicator of cell proliferation (Li et al. 2009). High Ki-67 expression has been shown to be a negative prognostic factor for patients with Glioblastoma multiforme (Persson and Englund 2008; Li et al. 2009). This suggests that the anti-invasive properties of CR are due in part to a reduction of proliferative, glycolytic and angiogenic factors. Additional experiments are required to test this hypothesis in the VM-M3 brain tumor model.

Calorie restriction significantly reduced tumor invasion into the contralateral hemisphere but did not completely inhibit all invasion. It has been previously shown that a restricted ketogenic diet used in combination with low dose 2-deoxy-D-glucose (2DG), a potent glycolysis inhibitor, achieved synergy with regard to reductions in tumor size (Marsh et al. 2008a). We therefore consider that calorie restriction or restricted ketogenic diets can be used in conjunction with low dose chemotherapeutic agents to reduce overall toxicity.

I also provide evidence of an increased dependence on glutamine for energy and survival in the VM-M3 brain tumor cell line. It is known that rapidly dividing cells and tumor cells are heavily dependent on glutamine for macromolecular synthesis and anaplerosis (McKeehan 1982; Kovacevic and McGivan 1983; Newsholme et al. 1985; Newsholme et al. 2003b; Deberardinis et al. 2008). However, few have suggested a potential role for glutamine specifically in energy production in the TCA cycle (Reitzer et al. 1979; McKeehan 1982; Pisarenko et al. 1985; Weinberg et al. 2000; Schwimmer et al. 2005; Phillips et al. 2009). I suggest that glutamine, as opposed to glucose, is the preferred

energy substrate for the invasive and metastatic VM-M3 cell line. I show that glutamine alone is able to maintain a sufficient ATP supply whereas glucose is not. Bioluminescence can be directly correlated to ATP concentration (Supplemental Figure 5A). In addition, because we use a clonally selected cell population, the amount of bioluminescence emitted per cell is standardized, and therefore we can also directly correlate bioluminescence with cell number (Supplemental Figure 5B). Reitzer et al. provided evidence that glutamine was the primary fuel used by HeLa cells, and glucose was used to generate intermediates for biosynthetic reactions (Reitzer et al. 1979). These findings are in opposition to the idea that glutamine derived malate is converted to pyruvate in order to generate reducing equivalents for macromolecular synthetic and anaplerotic reactions (Newsholme et al. 2003b; DeBerardinis et al. 2007; DeBerardinis 2008). In this model, NADPH is generated by the conversion of malate to pyruvate via cytosolic malic enzyme. As a result, pyruvate, derived from glutamine metabolism, is thought to be primarily converted to lactate or alanine (Supplemental Figure 3) (DeBerardinis et al. 2007; DeBerardinis 2008; Vander Heiden et al. 2009). However, I show that in a glutamine only media, the VM-M3 cells produce very little lactate, which is in agreement with the findings of Reitzer et al. (Reitzer et al. 1979). I also show that the inhibition of malic enzyme with *meso*-Tartrate reduced lactate production in the presence of glucose and glutamine, but had no effect on VM-M3 survival or lactate production in a glutamine only media. Interestingly, there are multiple isoforms of malic enzyme, two of which are mitochondrial and one is cytosolic (Moreadith and Lehninger 1984; Teller et al. 1992; Pongratz et al. 2007). Additionally, the inhibition of malic

enzyme via *meso*-Tartrate also stimulates the reaction in the reverse direction (Do Nascimento et al. 1975). By stimulating the conversion of pyruvate to malate in the cytosol, glycolytic flux through lactate dehydrogenase would be reduced. This could explain the reduction in viability and lactate production when the VM-M3 cells are incubated with *meso*-Tartrate only in the presence of glucose. This perhaps indicates that *meso*-Tartrate is active against cytosolic malic enzyme and not against mitochondrial malic enzyme or that the inhibitor is not transported into the mitochondria. I therefore posited that glutamine usage in the VM-M3 cell line is independent of cytosolic malic enzyme, and not primarily used for macromolecular synthesis or anaplerosis. Because *meso*-Tartrate is an analog of malate (Do Nascimento et al. 1975), it seems unlikely that the inhibitor would have additional non-specific effects in the cytoplasm. However, specific enzyme assays would be necessary to fully determine the inhibitory effects of *meso*-Tartrate on malic enzyme and on other enzymes involved in glutamine metabolism within the mitochondria, as *meso*-Tartrate has been shown to also inhibit malate dehydrogenase and fumarase (Do Nascimento et al. 1975).

Instead of the hypothesis that glutamine derived malate exits the TCA and mitochondria, I suggest that glutamine derived TCA citrate is responsible for the generation of extramitochondrial malate as previously suggested (Supplemental Figure 4) (Sauer and Dauchy 1978; Moreadith and Lehninger 1984). Malate from the cytoplasm can re-enter the mitochondria where mitochondrial malic enzyme can then convert malate to pyruvate. This would generate a separate mitochondrial pool of pyruvate (Sauer and Dauchy 1978;

McKeehan 1982; Kovacevic and McGivan 1983; Moreadith and Lehninger 1984; Baggetto 1992; Board and Newsholme 1996). In a glutamine only media, this allows for the regeneration of acetyl-CoA for continued carbon cycling around the TCA (Pongratz et al. 2007). In support of this, Reitzer et al. found that in a glutamine only media, no TCA cycle intermediates were depleted with the exception of isocitrate, which is downstream of citrate (Reitzer et al. 1979). Preliminary NMR data indicate that citrate is being isotopically labeled as a result of added ^{13}C glutamine, further supporting the idea that malate remains in the TCA cycle (C. Strelko, unpublished data). Glutamine derived malate that exits the TCA can also result in ^{13}C labeled pyruvate and subsequently citrate, if pyruvate re-enters the mitochondria. However, it has been shown that little cytosolic pyruvate enters the mitochondria, presumably due to very high activities of lactate dehydrogenase and pyruvate dehydrogenase kinase, which inhibits the conversion of pyruvate to acetyl-CoA via pyruvate dehydrogenase (Reitzer et al. 1979; Feron 2009; Jones and Thompson 2009).

In addition, I show that in the presence of the short chain fatty acid, heptanoic acid, survival in glutamine is greatly enhanced relative to either metabolite alone, indicating that a source of acetyl-CoA is essential for survival and TCA cycling when glutamine is present (Kovacevic and McGivan 1983). Heptanoic acid is a 7-carbon odd chain fatty acid resulting in two units of acetyl-CoA and one unit of propionyl CoA (Nelson and Cox 2005). Propionyl CoA can subsequently be converted to succinyl-CoA, which will increase the amount of substrates entering the TCA upstream of the energy-generating

step (Nelson and Cox 2005). It is interesting that heptanoic acid is unable to maintain a similar level of viability as glutamine alone. However, recent evidence has shown that glioma cell lines contain isocitrate dehydrogenase mutations (IDH1 and IDH2), which could affect the level of TCA cycle intermediates such as α-ketoglutarate (Dang et al. 2009). Additionally, if acetyl-CoA were present without glutamine, it would continue to cycle with citrate as described above in a potential futile cycle. Although propionyl-CoA can be converted to succinyl-CoA, this requires ATP input, essentially negating the production of GTP from the TCA cycle (Nelson and Cox 2005). Heptanoic acid however can enhance survival in glutamine due to the continued entry of glutamine carbons and subsequently α-ketoglutarate into the TCA cycle. In the presence of additional sources of acetyl-CoA, a portion of the glutamine carbons could potentially be utilized for other biosynthetic reactions allowing for cell growth (DeBerardinis et al. 2007; Vander Heiden et al. 2009). Further ^{13}C NMR studies are required that would confirm the metabolism of both glutamine and fatty acid carbons when combined.

β-hydroxybutyrate, traditionally considered a ketone body, which is also metabolized to acetyl-CoA, did not enhance VM-M3 cell survival in a glutamine only media. The enzymes necessary for ketone metabolism are found in strong association with the inner mitochondrial membrane, which relies on cardiolipin for structural integrity (Sato et al. 1995; Kiebish et al. 2008a). However, as previously stated, the VM-M3 cells have an abnormal cardiolipin profile, perhaps negatively affecting the cell's ability to metabolize ketones (Kiebish et al. 2008a). A number of tumor cell lines have also been found to be

deficient in expression or activity of the key enzymes involved in ketone metabolism (BDH and SCOT) (Fredericks and Ramsey 1978; Tisdale 1984; Zhou et al. 2007). Therefore, further studies are necessary to determine if the VM-M3 cells express abnormal levels of BDH and SCOT or if enzyme activity is impaired. Additionally, SCOT enzyme activity is dependent on succinyl-CoA, and could potentially compete with succinyl-CoA synthetase, the energy generating enzyme of the TCA (Phillips et al. 2009). Interestingly, we did see a slight but significant reduction in cell viability when the VM-M3 cells were incubated in glutamine in the presence of β-OHB. This suggests that high ketone levels could inhibit VM-M3 cell growth and survival.

In addition, the inhibition of succinate dehydrogenase with 3-nitropropionic acid (3-NP) (Supplemental Figure 3) resulted in a significant reduction in cell survival relative to the non-drug control when glutamine was present in the media either as the sole energy substrate or in the presence of glucose. However, cell survival in a glucose only media was nearly the same in the presence or absence of the TCA cycle inhibitor. This indicates that the inhibitory action of 3NP is specific to the TCA cycle and glutamine metabolism as has been previously illustrated due to its structural similarity with succinate (Scallet et al. 2003; Huang et al. 2006). Because, as previously illustrated, bioluminescence imaging can be directly correlated to ATP concentration (Supplemental Figure 5A), I suggest that in a glutamine only media, the majority of ATP comes from substrate level phosphorylation in the TCA cycle. However, due to the fact that the succinate dehydrogenase complex is also part of the electron transport chain, strict

inhibition of the TCA cannot be assumed. 3-NP would also inhibit electron transfer from $FADH_2$ to complex II, which could also have an inhibitory effect on glutamine metabolism due to a reduction in reducing equivalents. Because 3-NP resulted in significant reductions in cell viability in all conditions tested, though not to the same extent, it is possible that at the concentration used, reductions in cell viability could be due to non-specific toxicities. It is unclear if the VM-M3 cells become more vulnerable to inhibition when incubated in glutamine compared to glucose. It would be interesting to test a non-metabolic inhibitor in the various metabolites to determine if the metabolite present significantly effects drug toxicity.

Interestingly, the inhibition of adenylate kinases by diamino pentaphosphate (Ap5A) significantly reduced VM-M3 cell viability when in a glutamine only media but had no effect on VM-M3 cell viability when in both glucose + glutamine or glucose alone. The adenylate kinases serve a variety of functions to include phosphate transfer between ADP and ATP (Dzeja et al. 2002). In addition, the adenylate kinases have also been shown to be important in the transfer of ATP out of the mitochondria (Janssen et al. 2000; Dzeja et al. 2002; Dzeja and Terzic 2003). Also, these enzymes have been shown to participate in the transfer of phosphates from GTP to ATP (Dzeja et al. 2002). Energy from substrate level phosphorylation in the TCA primarily produces GTP (Kibbey et al. 2007; Phillips et al. 2009), requiring a phosphate transfer to ATP. Inhibition of these kinases with Ap5A would therefore inhibit both phosphate transfer from GTP to ATP and subsequent transfer of the mitochondrial ATP to the cytosol, if the majority of energy were generated

from substrate level phosphorylation in the TCA. Additionally, the addition of ^{13}C labeled glutamine in culture resulted in ^{13}C labeled succinate, further confirming that glutamine carbons are entering a highly active TCA (C. Strelko, unpublished data). ^{13}C NMR studies in the presence of the various metabolic inhibitors could further illustrate the pathways utilized by glutamine and the specificity of the selected inhibitors, as many inhibitors can become toxic via non-specific mechanisms at high concentrations. Another thing to consider is that at low concentrations the impact of the inhibitor may be diminished, potentially masking important differences between the response of the VM-M3 cells in the various metabolites. Therefore, additional studies using a range of concentrations could identify an optimal concentration that allows for specific effects to be maximized while toxic effects moderated.

Numerous studies suggest that oxidative phosphorylation is functional in tumor cells and can therefore be responsible for energy production (Reitzer et al. 1979; Guppy et al. 2002; Fantin et al. 2006; Feron 2009). However, in the VM-M3 cells, the continued production of ATP in the presence of oligomycin, the F1-ATPase inhibitor (Supplemental Figure 3), supports the Warburg hypothesis that there is a mitochondrial impairment preventing the generation of energy via oxidative phosphorylation (Warburg 1956). Also, as previously stated, we have shown that electron transport chain enzyme activities are reduced in the VM-M3 tumor compared to the VM brain, and mitochondrial lipid abnormalities could be the cause (Kiebish et al. 2008a). This further suggests that the VM-M3 cells suffer from a mitochondrial impairment and that the majority of ATP is

generated from substrate level phosphorylation from both glycolysis and the TCA cycle. Further studies utilizing the uncoupler FCCP could support these findings.

ATP from substrate level phosphorylation specifically in the TCA cycle has been demonstrated in both heart and kidney cells in hypoxia (Pisarenko et al. 1985; Weinberg et al. 2000). In a hypoxic environment, ATP from oxidative phosphorylation would be inhibited. However, ATP from substrate level phosphorylation in the TCA cycle, as an alternative to glycolysis or oxidative phosphorylation, has never before been demonstrated in cancer cells. I therefore have the first evidence of energy generation from the TCA in the highly metastatic VM-M3 cell line.

Glutamine is in fact the highest concentrated amino acid in circulation (Darmaun et al. 1986; Bode 2001; Newsholme et al. 2003a). My data suggest that the VM-M3 cells are capable of generating enough energy from glutamine alone to maintain survival. Hence, this may be why calorie restriction is largely ineffective in reducing metastatic spread. Though calorie restriction acts by reducing circulating plasma glucose levels, evidence shows that circulating glutamine levels are increased in mice during calorie restriction (Selman et al. 2006). Additionally, plasma glutamine levels have been shown to rise in rats implanted with tumors as a result of net release from muscle and liver tissues (Quesada et al. 1988; Souba 1993). I show that only small amounts of glucose in the presence of glutamine are necessary to maintain cell growth and survival *in vitro*. CR however, had some inhibitory effect on the VM-M3 primary tumor grown

subcutaneously. Previous studies have shown CR to be anti-angiogenic and anti-inflammatory mediated in part by an elevation in ketone levels (Mukherjee et al. 2002; Mukherjee et al. 2004; Veech 2004). Therefore, the anti-angiogenic and anti-inflammatory action of CR could be responsible for the reduction in primary tumor size. As glutamine promotes VM-M3 cell growth and survival, the failure of CR to target glutamine levels could be responsible for the failure of CR to inhibit VM-M3 tumor metastasis.

The brain however may be more responsive to CR because high plasma levels of glutamate, the metabolic product of glutamine, and glutamine itself, are not reflected in the brain due to saturation of the transporter in the blood brain barrier (Smith 1991). Glutamine can also be synthesized from precursors within the brain. The concentrations of these "dispensable" amino acids are therefore not affected by changes in plasma concentrations (Smith 1991). Within the brain, glutamate is a neurotransmitter and thus glutamine/glutamate cycles are under tight control by the surrounding astrocytes (Daikhin and Yudkoff 2000). Therefore, in the brain, the VM-M3 cells may have to rely more on glucose availability than glutamine.

In addition, I show that the glutamine analog, 6-diazo-5-oxo-L-norleucine (DON), had a significant inhibitory effect on VM-M3 growth *in vitro* and on VM-M3 tumor growth and metastasis *in vivo*. Previous reports have suggested that the inhibitory effect of DON was due to its inhibition of purine and pyrimidine synthesis (Livingston et al. 1970;

Ovejera et al. 1979; Lyons et al. 1990; Griffiths et al. 1993). However, I am suggesting that the principle inhibitory action of DON is through the inhibition of ATP synthesis via substrate level phosphorylation in the TCA as a result of reduced glutamine metabolism. It has previously been determined that in mouse leukemia cells, DON induced a significant reduction of both ATP and GTP (Lyons et al. 1990). Therefore, it is unclear if a reduction in ATP is a cause or effect of reduced purine and pyrimidine synthesis. Presently, we know that glutamine is sufficient to maintain VM-M3 cell survival *in vitro*. Because survival is enhanced in both glucose and glutamine, it is possible that glutamine stimulates glycolysis in VM-M3 cells as has been previously demonstrated in C6 glioma cells (Portais et al. 1996). As a result, a significant fraction of ATP could be generated from glycolysis while glutamine metabolism could be used for nucleotide biosynthesis.

It is interesting to note that although DON inhibited metastasis to the liver, lung, and kidneys, DON treatment alone had no effect on metastasis to the spleen. The spleen has been determined to be a large reservoir of monocytes, and may represent a sanctuary for the myeloid-like metastatic cells (Swirski et al. 2009). Interestingly, studies have shown increases in glutaminase activity in the spleens of tumor bearing mice (Aledo et al. 1998). Glutaminase is the first enzyme involved in glutamine metabolism. This perhaps indicates that the spleen could support tumor growth due to an influx of glutamine originally intended to support immune function (Medina 2001). Further studies are required in order to determine the factors involved in tumor cell metastasis to the spleen.

We showed that DON administration *in vitro* primarily resulted in an inhibition of cell growth, but was not cytotoxic. Additionally, *in vivo,* whole body bioluminescence was nearly unchanged over the course of DON treatment with the exception of spleen metastasis (data not shown). This indicates that both *in vivo* and *in vitro*, DON is acting to inhibit cell growth, consistent with previous reports in human studies (Magill et al. 1957). However, there have been reports of tumor regression indicating that DON can be useful in both early and late stage tumor management (Magill et al. 1957; Livingston et al. 1970).

Because glucose and glutamine acted synergistically *in vitro,* I developed a diet/drug combination that targeted both glucose and glutamine *in vivo.* Previous studies have found that calorie restriction administered together with low doses of 2-deoxyglucose, an inhibitor of glucose metabolism, acted synergistically to reduce brain tumor growth (Marsh et al. 2008a). Previous studies also showed that calorie restriction is a powerful anti-angiogenic therapy and an inhibitor of Akt signaling (Mukherjee et al. 2002; Mukherjee et al. 2004; Marsh et al. 2008b). In addition, *in vitro*, glucose and glutamine acted synergistically to promote VM-M3 cell survival and growth. Therefore, I sought to determine if calorie restriction and DON treatment could act synergistically to reduce systemic metastasis *in vivo*. I show that DON treatment, either alone or in combination with CR, significantly reduced tumor growth and metastasis. Moreover, less DON was used to achieve therapeutic effect in the DON + CR mice than in the mice treated with DON alone. Drug doses for the mice were adjusted in order to reduce potential toxicities

or extreme energy stress. The mice on DON + CR were active throughout the study and maintained a healthy body weight. Interestingly, the mice on DON treatment alone showed a more adverse response to drug treatment than did the mice on DON + CR, as illustrated by a drop in body weight and lethargy over the last 3 days of the study. Toxicity in the mice treated with DON alone became more evident as the study progressed. Toxicity was reduced and survival was enhanced when DON was administered together with CR since less drug was needed to achieve therapeutic effect. Moreover, the incidence of metastasis to spleen was significantly lower in the DON + CR mice than in the mice treated with DON alone. This implies that both glucose and glutamine are major sources of energy for the VM-M3 tumor cell line. My findings should stimulate renewed interest in DON and other glutamine targeting drugs for the treatment for human metastatic cancer especially when combined with calorie restriction or other drugs that target glucose metabolism.

In addition to DON, phenylbutyrate (PBA) has been used extensively *in vitro* and in human clinical trials (Engelhard et al. 1998; Dyer et al. 2002; Li et al. 2004; Phuphanich et al. 2005; Lopez et al. 2007). In humans, PBA is metabolized to phenylacetate (PA), which then covalently conjugates with glutamine (Thibault et al. 1994; Darmaun et al. 1998). This PA-glutamine conjugate is then excreted, effectively removing glutamine from circulation (Darmaun et al. 1998). Although current studies utilize PBA as a histone deacetylase inhibitor, its mechanism of action could be due in part to a reduction of circulating glutamine. *In vitro,* PBA displayed a dose dependent toxicity towards the

VM-M3 cell line (supplemental Figure 2). However, studies *in vivo* could not be evaluated in our model because mice metabolize PBA differently than humans. In the mouse, PA primarily conjugates with glycine (James et al. 1972). Therefore, any possible inhibitory action of PBA could not be attributed to an inhibition of glutamine metabolism. Because PBA has already been introduced in clinical trials and is well tolerated by humans (Thibault et al. 1994), PBA can potentially be used in place of DON as a glutamine-targeting drug. Because PBA is well tolerated, the toxicities traditionally seen with DON treatment could be avoided.

It is interesting to note that the VM-M3 cell line is myeloid-like, displaying genetic, morphologic, and behavioral characteristics of macrophages (Huysentruyt et al. 2008). In addition, it is well known that glutamine along with glucose is a major energy substrate for cells of myeloid origin (Newsholme et al. 1987; Newsholme et al. 1996). High rates of both glycolysis and glutaminolysis allow for precise regulation of processes that use intermediates of these pathways (Newsholme et al. 1985; Newsholme et al. 1987). Current hypotheses state that mitochondrial instability leads to genomic instability via the retrograde signaling pathway, thus increasing the potential for oncogenic transformation (Butow and Avadhani 2004; Erol 2005; Singh et al. 2005). The retrograde signaling pathway consists of a series of sensors that detect mitochondrial instability as a result of impaired energy production. Sensors such as HIF-1α and NfκB respond to reactive oxygen species and increased intracellular calcium levels, which are indicators of mitochondrial damage and an impairment of respiration (Butow and Avadhani 2004).

Over time, this respiration impairment would result in the upregulation of TCA and glycolytic substrate level phosphorylation, induce the default state of proliferation, and induce genetic defects, resulting in cancer (Butow and Avadhani 2004; Soto and Sonnenschein 2004; Erol 2005; Singh et al. 2005; Seyfried and Shelton 2010). The VM-M3 cell line's dependence on TCA substrate level phosphorylation for energy, along with the cell's altered mitochondrial lipid profile and reduced ETC enzyme activity suggests an impaired respiratory capacity (Kiebish et al. 2008a). When this respiratory impairment occurs in a myeloid cell, the result is a tumor cell that is highly dependent on glutamine, and is capable of metastatic spread.

In addition to an increased dependence on glutamine, I also show that the VM-M3 cell line is capable of phagocytosis, another property of myeloid cells. A number of human metastatic tumors display similar phagocytic properties, to include, brain, skin, lung, and breast (Spivak 1973; Coopman et al. 1998; Ghoneum and Gollapudi 2004; Abodief et al. 2006; Lugini et al. 2006; Fais 2007; Huysentruyt et al. 2008; Moonda and Fatteh 2009; Huysentruyt et al. 2010). It had been suggested previously that these phagocytic capabilities were not for the destruction of host immune cells, but for the generation of ATP during times of energy stress (Lugini et al. 2006; Fais 2007). Because calorie restriction was ineffective in reducing metastatic spread I sought to test this phagocytic property by developing an *in vitro* assay utilizing a 3-dimensional matrix of extracellular matrix glycoproteins. I showed that when the VM-M3 cells are in this matrix, survival during energy stress is significantly enhanced relative to a non-matrix control. In

addition, I show that there is an increase in lactate, indicating an increase in glycolysis when in the presence of this matrix material. I further tested this hypothesis by adding chloroquine, a lysosomal targeting drug. Chloroquine is a lysotropic compound that aggregates in the lysosomes. As a result, lysosomal pH is increased, rendering digestive enzymes inactive (Dang 2008; Maclean et al. 2008). Therefore, chloroquine would render phagocytosed material unavailable for digestion. It is interesting that cholorquine not only inhibited cell survival in the matrix, but also in the absence of the matrix only when under energy stress. This perhaps suggests that these cells are also capable of autophagy and/or cannibalism (Fais 2007). Autophagy or "self eating" is often initiated in response to energy stress and serves as a mechanism to derive nutrients from the degradation of internal organelles and macromolecules (Jones and Thompson 2009). Therefore, chloroquine could act as a broad inhibitor of autophagy, cannibalism, and phagocytosis.

I also developed an additional assay to test whether or not the VM-M3 cells were capable of generating energy from the digestion of phagocytosed material. I coated non-opsinized latex beads with the most common matrix protein, collagen. Previous studies have shown that macrophages are capable of endocytosing extracellular proteins to be digested into individual amino acids, which can alter the rate of extracellular glutamine utilization (Newsholme et al. 1987). I show that survival was significantly enhanced in the presence of the collagen coated latex beads compared to the naked beads. This survival however was not accompanied by an increase in lactate due to the fact that

collagen does not contain any carbohydrate groups. However, the ammonia concentration was also not significantly higher in the presence of the coated latex beads. This may be due to the fact that collagen has a very high glycine content. In addition, the expected small increases in ammonia could have been below the detection limits of the assay.

I next hypothesized that under calorie restriction, the phagocytic behavior of the VM-M3 cells could be responsible for their continued survival and metastasis *in vivo*. I therefore sought to determine if chloroquine would be able to reduce tumor growth and metastasis in both the VM-M3 brain tumor model and the VM-M3 model for systemic metastatic cancer. As expected, chloroquine alone had no inhibitory effect on tumor growth, invasion, or metastasis. Unfortunately, chloroquine in conjunction with calorie restriction also did not have any effect on tumor growth, invasion, or metastasis. Calorie restriction should induce some level of energy stress on the cells because we know that glucose and glutamine work synergistically to allow for cell survival and growth *in vitro*. However, glutamine is a major energy source for the VM-M3 cells, indicating that in order to manage tumor growth and metastasis, a unique drug/diet therapy targeting glucose, glutamine, and phagocytosis should be developed.

Finally, the myeloid properties of the VM-M3 cells could explain why glutamine is more important than glucose as an energy generating fuel. It has been shown that an elevation in glucose uptake results in an elevation of activity in the pentose phosphate pathway

(PPP) in macrophages (Newsholme et al. 1996). The PPP primarily utilizes glucose-6-phosphate, a glycolytic intermediate, as a precursor. Therefore, a large majority of metabolized glucose may be contributing to the PPP for nucleotide and fatty acid synthesis (Jones and Thompson 2009). The PPP can also generate NADPH required for macromolecular synthesis (Tennant et al. 2009). It had previously been suggested that the high rate of glycolysis in tumor cells in the presence of glutamine was for the purpose of providing these essential precursors rather than strictly for energy production (Reitzer et al. 1979; McKeehan 1982; Mazurek et al. 2005; Christofk et al. 2008; Kroemer and Pouyssegur 2008). Though survival in glucose + glutamine was approximately 5-fold higher than survival in glucose alone (Figure 26), lactate only increased by a factor of 2.5 (Figure 27). Therefore, less lactate per cell was produced when glucose and glutamine were present, indicating that glycolytic intermediates may be used primarily for macromolecular synthesis via the PPP.

Taken together, these findings illustrate the usefulness of the VM-M3 tumor as a model for both human GBM and for systemic metastatic cancer. In addition I show that the invasive/metastatic VM-M3 tumor is highly dependent on glutamine for growth and survival specifically as a result of ATP generated from substrate level phosphorylation in the TCA cycle. Interestingly, during energy stress, phagocytosis may also play a role in maintaining a sufficient ATP supply for VM-M3 cell survival.

CONCLUSIONS

In conclusion, I describe a novel model for brain tumor growth and invasion. This model is unique in its invasive qualities and provides a new tool for evaluating potential therapies. To date, no xenograft model or chemically induced rodent model displays the invasive characteristics of the VM-M3 model, to include sub-pial and ventricular spread, perivascular, perineuronal, peri- and intra-fascicular growth, and inter-hemispheric invasion. The VM-M3 tumor cells also express molecular markers linked to highly malignant Glioblastoma multiforme (Hoelzinger et al. 2005; Li et al. 2009). In addition, the use of bioluminescent data provides a way to quantitate tumor growth and invasion. I also show that calorie restriction, which lowers circulating glucose and elevates ketones, is anti-invasive in the VM-M3 brain tumor model.

However, I also provide evidence of an increased dependence on glutamine in the VM-M3 cell line, similar to a number of other cancer cell lines (Reitzer et al. 1979; McKeehan 1982; DeBerardinis et al. 2007; Matheson et al. 2007). Glutamine utilization could support biosynthetic and anapleurotic reactions (DeBerardinis et al. 2007; Deberardinis et al. 2008). However, I have the first evidence in cancer cells that energy derived from glutamine is primarily a result of substrate level phosphorylation in the TCA cycle. Due to the myeloid properties of this cell line and of many other human metastatic cancers, (Spivak 1973; Ghoneum and Gollapudi 2004; Abodief et al. 2006; Lugini et al. 2006; Fais 2007; Huysentruyt et al. 2008; Moonda and Fatteh 2009;

Huysentruyt et al. 2010), I suggest that many metastatic cancers possess a higher dependence for glutamine rather than for glucose. In support of this, I show that calorie restriction was unable to inhibit tumor metastasis in the VM-M3 model for systemic metastasis. This could be a result of the high levels of glutamine found in circulation (Darmaun et al. 1986; Bode 2001; Newsholme et al. 2003a). The glutamine analog, DON, along with calorie restriction significantly reduced both tumor growth and metastasis indicating that metastatic cancer can be targeted with metabolic therapies.

In addition, the phagocytic properties of these myeloid-like tumor cells may also serve as a mechanism to provide metabolites during times of low nutrient supply (Fais 2007). This may occur via phagocytosis and digestion of extracellular material, host cells, internal organelles or even other tumor cells (Lugini et al. 2006; Fais 2007; Jones and Thompson 2009). Therefore, I suggest that a unique therapy should be designed that targets both the glutamine dependence of the VM-M3 cells as well as their phagocytic capabilities. Due to the similarities between VM-M3 tumor cell behavior and human metastatic cancer, the treatment of metastasis may involve similar targets.

APPENDIX

Publications

Seyfried, T.N., and **Shelton, L.M.** Cancer as a metabolic disease. *J Nutrition and Metabolism* 2010 Jan 27; 7(1): [epub ahead of print].

Shelton, L.M., Mukherje, P., Huysentruyt, L.C., Urits, I., Rosenberg, J.A., and Seyfried, T.N. A novel pre-clinical *in vivo* mouse model for malignant brain tumor growth and invasion. *J Neurooncol* 2010 Jan 13; [epub ahead of print].

Huysentruyt, L.C., **Shelton, L.M.**, and Seyfried, T.N. Influence of methotrexate and cisplatin on tumor progression and survival in the VM mouse model of systemic metastatic cancer. *Int J Cancer* 2010 Jan 1; 126(1): 65-72.

Huysentruyt LC, Mukherjee P, Banerjee D, **Shelton L.M**., and Seyfried, T.N. Metastatic cancer cells with macrophage properties: Evidence from a new murine tumor model. *Int J Cancer* 2008 Jul 1;123(1):73-84.

Mukherjee, P., Faber, A.C., **Shelton, L. M**., Baek, R. C., Chiles, T. C., and Seyfried, T. N. Ganglioside GM3 Suppresses the Pro-Angiogenic Effects of Vascular Endothelial Growth Factor and Ganglioside GD1a. *J. Lipid Res.* 2008 May 49; 929-938.

Abstracts

Shelton, L.M., Huysentruyt, L.C., Seyfried, T.N. (2010) Targeting glucose and glutamine for the metabolic management of systemic metastatic cancer. *American Association for Cancer Research* [accepted]

Shelton, L.M., Strelko, C.L., Roberts, M.F., Seyfried, T.N. (2010) Krebs cycle substrate level phosphorylation drives metastatic cancer cells. *American Association for Cancer Research* [accepted]

Huysentruyt, L.C., **Shelton, L.M**., Mukherjee, P., Seyfried, T.N. (2009) Mouse microgliomas with properties of human glioblastoma. *American Society for Neurochemistry*

Huysentruyt, L.C., **Shelton, L.M**., Seyfried, T.N. (2008) A novel pre-clinical mouse model of systemic metastatic cancer. *American Association for Cancer Research*

Mukherjee P.M., Faber A.C**., Shelton L.M**., Baek R.C., Chiles T.C., Seyfried T.N. (2008) Ganglioside GM3 Inhibits the Pro-Angiogenic Effects of Vascular Endothelial Growth Factor and Ganglioside GD1a. *American Association for Cancer Research*

Mukherjee P.M., Faber A.C**., Shelton L.M**., Baek R.C., Chiles T.C., Seyfried T.N. (2007) Ganglioside GM3 Inhibits the Pro-Angiogenic Effects of Vascular Endothelial Growth Factor and Ganglioside GD1a. *Glycobiology*

REFERENCES

Abate L. E., Mukherjee P. and Seyfried T. N. (2006) Gene-linked shift in ganglioside distribution influences growth and vascularity in a mouse astrocytoma. *J Neurochem* **98,** 1973-1984.

Abodief W. T., Dey P. and Al-Hattab O. (2006) Cell cannibalism in ductal carcinoma of breast. *Cytopathology* **17,** 304-305.

Aledo J. C., Segura J. A., Barbero L. G. and Marquez J. (1998) Early differential expression of two glutaminase mRNAs in mouse spleen after tumor implantation. *Cancer letters* **133,** 95-99.

Assanah M., Lochhead R., Ogden A., Bruce J., Goldman J. and Canoll P. (2006) Glial progenitors in adult white matter are driven to form malignant gliomas by platelet-derived growth factor-expressing retroviruses. *J Neurosci* **26,** 6781-6790.

Bacac M. and Stamenkovic I. (2008) Metastatic cancer cell. *Annual review of pathology* **3,** 221-247.

Baggetto L. G. (1992) Deviant energetic metabolism of glycolytic cancer cells. *Biochimie* **74,** 959-974.

Barth R. F. (1998) Rat brain tumor models in experimental neuro-oncology: the 9L, C6, T9, F98, RG2 (D74), RT-2 and CNS-1 gliomas. *Journal of neuro-oncology* **36,** 91-102.

Bian X. W., Yang S. X., Chen J. H., Ping Y. F., Zhou X. D., Wang Q. L., Jiang X. F., Gong W., Xiao H. L., Du L. L., Chen Z. Q., Zhao W., Shi J. Q. and Wang J. M. (2007) Preferential expression of chemokine receptor CXCR4 by highly

malignant human gliomas and its association with poor patient survival. *Neurosurgery* **61,** 570-578; discussion 578-579.

Board M. and Newsholme E. (1996) Hydroxycitrate causes altered pyruvate metabolism by tumorigenic cells. *Biochemistry and molecular biology international* **40,** 1047-1056.

Board M., Humm S. and Newsholme E. A. (1990) Maximum activities of key enzymes of glycolysis, glutaminolysis, pentose phosphate pathway and tricarboxylic acid cycle in normal, neoplastic and suppressed cells. *The Biochemical journal* **265,** 503-509.

Bode B. P. (2001) Recent molecular advances in mammalian glutamine transport. *The Journal of nutrition* **131,** 2475S-2485S; discussion 2486S-2477S.

Briceno E., Calderon A. and Sotelo J. (2007) Institutional experience with chloroquine as an adjuvant to the therapy for glioblastoma multiforme. *Surgical neurology* **67,** 388-391.

Butow R. A. and Avadhani N. G. (2004) Mitochondrial signaling: the retrograde response. *Molecular cell* **14,** 1-15.

Cahill G. F., Jr. (1970) Starvation in man. *The New England journal of medicine* **282,** 668-675.

Candolfi M., Curtin J. F., Nichols W. S., Muhammad A. G., King G. D., Pluhar G. E., McNiel E. A., Ohlfest J. R., Freese A. B., Moore P. F., Lerner J., Lowenstein P. R. and Castro M. G. (2007) Intracranial glioblastoma models in preclinical neuro-

oncology: neuropathological characterization and tumor progression. *Journal of neuro-oncology* **85,** 133-148.

Castellanos T., Ascencio F. and Bashan Y. (2000) Starvation-induced changes in the cell surface of Azospirillum lipoferum. *FEMS microbiology ecology* **33,** 1-9.

Chambers A. F., Groom A. C. and MacDonald I. C. (2002) Dissemination and growth of cancer cells in metastatic sites. *Nature reviews* **2,** 563-572.

Chang S. M., Parney I. F., Huang W., Anderson F. A., Jr., Asher A. L., Bernstein M., Lillehei K. O., Brem H., Berger M. S. and Laws E. R. (2005) Patterns of care for adults with newly diagnosed malignant glioma. *Jama* **293,** 557-564.

Christofk H. R., Vander Heiden M. G., Harris M. H., Ramanathan A., Gerszten R. E., Wei R., Fleming M. D., Schreiber S. L. and Cantley L. C. (2008) The M2 splice isoform of pyruvate kinase is important for cancer metabolism and tumour growth. *Nature* **452,** 230-233.

Coopman P. J., Thomas D. M., Gehlsen K. R. and Mueller S. C. (1996) Integrin alpha 3 beta 1 participates in the phagocytosis of extracellular matrix molecules by human breast cancer cells. *Molecular biology of the cell* **7,** 1789-1804.

Coopman P. J., Do M. T., Thompson E. W. and Mueller S. C. (1998) Phagocytosis of cross-linked gelatin matrix by human breast carcinoma cells correlates with their invasive capacity. *Clin Cancer Res* **4,** 507-515.

Dai C. and Holland E. C. (2001) Glioma models. *Biochimica et biophysica acta* **1551,** M19-27.

Daikhin Y. and Yudkoff M. (2000) Compartmentation of brain glutamate metabolism in neurons and glia. *The Journal of nutrition* **130,** 1026S-1031S.

Dang C. V. (2008) Antimalarial therapy prevents Myc-induced lymphoma. *The Journal of clinical investigation* **118,** 15-17.

Dang L., White D. W., Gross S., Bennett B. D., Bittinger M. A., Driggers E. M., Fantin V. R., Jang H. G., Jin S., Keenan M. C., Marks K. M., Prins R. M., Ward P. S., Yen K. E., Liau L. M., Rabinowitz J. D., Cantley L. C., Thompson C. B., Vander Heiden M. G. and Su S. M. (2009) Cancer-associated IDH1 mutations produce 2-hydroxyglutarate. *Nature* **462,** 739-744.

Darmaun D., Matthews D. E. and Bier D. M. (1986) Glutamine and glutamate kinetics in humans. *The American journal of physiology* **251,** E117-126.

Darmaun D., Welch S., Rini A., Sager B. K., Altomare A. and Haymond M. W. (1998) Phenylbutyrate-induced glutamine depletion in humans: effect on leucine metabolism. *The American journal of physiology* **274,** E801-807.

DeBerardinis R. J. (2008) Is cancer a disease of abnormal cellular metabolism? New angles on an old idea. *Genet Med* **10,** 767-777.

Deberardinis R. J., Sayed N., Ditsworth D. and Thompson C. B. (2008) Brick by brick: metabolism and tumor cell growth. *Current opinion in genetics & development* **18,** 54-61.

DeBerardinis R. J., Mancuso A., Daikhin E., Nissim I., Yudkoff M., Wehrli S. and Thompson C. B. (2007) Beyond aerobic glycolysis: transformed cells can engage in glutamine metabolism that exceeds the requirement for protein and nucleotide

synthesis. *Proceedings of the National Academy of Sciences of the United States of America* **104,** 19345-19350.

Deroose C. M., Reumers V., Gijsbers R., Bormans G., Debyser Z., Mortelmans L. and Baekelandt V. (2006) Noninvasive monitoring of long-term lentiviral vector-mediated gene expression in rodent brain with bioluminescence imaging. *Mol Ther* **14,** 423-431.

Derr R. L., Ye X., Islas M. U., Desideri S., Saudek C. D. and Grossman S. A. (2009) Association between hyperglycemia and survival in patients with newly diagnosed glioblastoma. *J Clin Oncol* **27,** 1082-1086.

Do Nascimento K. H., Davies D. D. and Patil K. D. (1975) Unidirectional inhibition and activation of "malic' enzyme of Solanum tuberosum by meso-tartrate. *The Biochemical journal* **149,** 349-355.

Duffner P. K. (2006) The long term effects of chemotherapy on the central nervous system. *Journal of biology* **5,** 21.

Dyer E. S., Paulsen M. T., Markwart S. M., Goh M., Livant D. L. and Ljungman M. (2002) Phenylbutyrate inhibits the invasive properties of prostate and breast cancer cell lines in the sea urchin embryo basement membrane invasion assay. *International journal of cancer* **101,** 496-499.

Dzeja P. P. and Terzic A. (2003) Phosphotransfer networks and cellular energetics. *The Journal of experimental biology* **206,** 2039-2047.

Dzeja P. P., Bortolon R., Perez-Terzic C., Holmuhamedov E. L. and Terzic A. (2002) Energetic communication between mitochondria and nucleus directed by

catalyzed phosphotransfer. *Proceedings of the National Academy of Sciences of the United States of America* **99,** 10156-10161.

Ehtesham M., Stevenson C. B. and Thompson R. C. (2008) Preferential expression of chemokine receptor CXCR4 by highly malignant human gliomas and its association with poor patient survival. *Neurosurgery* **63,** E820; author reply E820.

El-Abbadi M., Seyfried T. N., Yates A. J., Orosz C. and Lee M. C. (2001) Ganglioside composition and histology of a spontaneous metastatic brain tumour in the VM mouse. *Br J Cancer* **85,** 285-292.

Engelhard H. H., Homer R. J., Duncan H. A. and Rozental J. (1998) Inhibitory effects of phenylbutyrate on the proliferation, morphology, migration and invasiveness of malignant glioma cells. *Journal of neuro-oncology* **37,** 97-108.

Erol A. (2005) Retrograde regulation due to mitochondrial dysfunction may be an important mechanism for carcinogenesis. *Medical hypotheses* **65,** 525-529.

Fais S. (2007) Cannibalism: a way to feed on metastatic tumors. *Cancer Lett* **258,** 155-164.

Fantin V. R., St-Pierre J. and Leder P. (2006) Attenuation of LDH-A expression uncovers a link between glycolysis, mitochondrial physiology, and tumor maintenance. *Cancer cell* **9,** 425-434.

Feron O. (2009) Pyruvate into lactate and back: from the Warburg effect to symbiotic energy fuel exchange in cancer cells. *Radiother Oncol* **92,** 329-333.

Fomchenko E. I. and Holland E. C. (2006) Mouse models of brain tumors and their applications in preclinical trials. *Clin Cancer Res* **12,** 5288-5297.

Foster E. S., Carrillo J. M. and Patnaik A. K. (1988) Clinical signs of tumors affecting the rostral cerebrum in 43 dogs. *Journal of veterinary internal medicine / American College of Veterinary Internal Medicine* **2,** 71-74.

Fraser H. (1971) Astrocytomas in an inbred mouse strain. *The Journal of pathology* **103,** 266-270.

Fraser H. (1986a) Brain tumours in mice, with particular reference to astrocytoma. *Food Chem Toxicol* **24,** 105-111.

Fraser H. (1986b) Brain tumours in mice, with particular reference to astrocytoma. *Food Chem. Toxicol.* **24,** 105-111.

Fredericks M. and Ramsey R. B. (1978) 3-Oxo acid coenzyme A transferase activity in brain and tumors of the nervous system. *Journal of neurochemistry* **31,** 1529-1531.

Fredericksen B. L., Wei B. L., Yao J., Luo T. and Garcia J. V. (2002) Inhibition of endosomal/lysosomal degradation increases the infectivity of human immunodeficiency virus. *Journal of virology* **76,** 11440-11446.

Fuller G. N., Rhee C. H., Hess K. R., Caskey L. S., Wang R., Bruner J. M., Yung W. K. and Zhang W. (1999) Reactivation of insulin-like growth factor binding protein 2 expression in glioblastoma multiforme: a revelation by parallel gene expression profiling. *Cancer research* **59,** 4228-4232.

Ghoneum M. and Gollapudi S. (2004) Phagocytosis of Candida albicans by metastatic and non metastatic human breast cancer cell lines in vitro. *Cancer detection and prevention* **28,** 17-26.

Griffiths M., Keast D., Patrick G., Crawford M. and Palmer T. N. (1993) The role of glutamine and glucose analogues in metabolic inhibition of human myeloid leukaemia in vitro. *The International journal of biochemistry* **25,** 1749-1755.

Guppy M., Leedman P., Zu X. and Russell V. (2002) Contribution by different fuels and metabolic pathways to the total ATP turnover of proliferating MCF-7 breast cancer cells. *The Biochemical journal* **364,** 309-315.

Heidner G. L., Kornegay J. N., Page R. L., Dodge R. K. and Thrall D. E. (1991) Analysis of survival in a retrospective study of 86 dogs with brain tumors. *Journal of veterinary internal medicine / American College of Veterinary Internal Medicine* **5,** 219-226.

Hoelzinger D. B., Mariani L., Weis J., Woyke T., Berens T. J., McDonough W. S., Sloan A., Coons S. W. and Berens M. E. (2005) Gene expression profile of glioblastoma multiforme invasive phenotype points to new therapeutic targets. *Neoplasia (New York, N.Y* **7,** 7-16.

Hoffman H. J. and Duffner P. K. (1985) Extraneural metastases of central nervous system tumors. *Cancer* **56,** 1778-1782.

Holland E. C. (2001) Gliomagenesis: genetic alterations and mouse models. *Nat Rev Genet* **2,** 120-129.

Hu X. and Holland E. C. (2005) Applications of mouse glioma models in preclinical trials. *Mutation research* **576,** 54-65.

Huang L. S., Sun G., Cobessi D., Wang A. C., Shen J. T., Tung E. Y., Anderson V. E. and Berry E. A. (2006) 3-nitropropionic acid is a suicide inhibitor of

mitochondrial respiration that, upon oxidation by complex II, forms a covalent adduct with a catalytic base arginine in the active site of the enzyme. *The Journal of biological chemistry* **281,** 5965-5972.

Huse J. T. and Holland E. C. (2009) Genetically engineered mouse models of brain cancer and the promise of preclinical testing. *Brain pathology (Zurich, Switzerland)* **19,** 132-143.

Huysentruyt L. C., Shelton L. M. and Seyfried T. N. (2010) Influence of methotrexate and cisplatin on tumor progression and survival in the VM mouse model of systemic metastatic cancer. *International journal of cancer* **126,** 65-72.

Huysentruyt L. C., Mukherjee P., Banerjee D., Shelton L. M. and Seyfried T. N. (2008) Metastatic cancer cells with macrophage properties: evidence from a new murine tumor model. *International journal of cancer* **123,** 73-84.

James M. O., Smith R. L., Williams R. T. and Reidenberg M. (1972) The conjugation of phenylacetic acid in man, sub-human primates and some non-primate species. *Proceedings of the Royal Society of London. Series B, Containing papers of a Biological character* **182,** 25-35.

Janssen E., Dzeja P. P., Oerlemans F., Simonetti A. W., Heerschap A., de Haan A., Rush P. S., Terjung R. R., Wieringa B. and Terzic A. (2000) Adenylate kinase 1 gene deletion disrupts muscle energetic economy despite metabolic rearrangement. *The EMBO journal* **19,** 6371-6381.

Jelluma N., Yang X., Stokoe D., Evan G. I., Dansen T. B. and Haas-Kogan D. A. (2006) Glucose withdrawal induces oxidative stress followed by apoptosis in

glioblastoma cells but not in normal human astrocytes. *Mol Cancer Res* **4,** 319-330.

Jones R. G. and Thompson C. B. (2009) Tumor suppressors and cell metabolism: a recipe for cancer growth. *Genes & development* **23,** 537-548.

Kauffman H. M., Cherikh W. S., McBride M. A., Cheng Y. and Hanto D. W. (2007) Deceased donors with a past history of malignancy: an organ procurement and transplantation network/united network for organ sharing update. *Transplantation* **84,** 272-274.

Kibbey R. G., Pongratz R. L., Romanelli A. J., Wollheim C. B., Cline G. W. and Shulman G. I. (2007) Mitochondrial GTP regulates glucose-stimulated insulin secretion. *Cell metabolism* **5,** 253-264.

Kiebish M. A., Han X., Cheng H. and Seyfried T. N. (2008a) Mitochondrial lipidome and electron transport chain alterations in non-metastatic and metastatic murine brain tumors. *J. Neurochem* **104** 34-38.

Kiebish M. A., Han X., Cheng H., Chuang J. H. and Seyfried T. N. (2008b) Cardiolipin and electron transport chain abnormalities in mouse brain tumor mitochondria: lipidomic evidence supporting the Warburg theory of cancer. *Journal of lipid research* **49,** 2545-2556.

Koehler-Stec E. M., Simpson I. A., Vannucci S. J., Landschulz K. T. and Landschulz W. H. (1998) Monocarboxylate transporter expression in mouse brain. *Am J Physiol* **275,** E516-524.

Kovacevic Z. and McGivan J. D. (1983) Mitochondrial metabolism of glutamine and glutamate and its physiological significance. *Physiological reviews* **63,** 547-605.

Kroemer G. and Pouyssegur J. (2008) Tumor cell metabolism: cancer's Achilles' heel. *Cancer cell* **13,** 472-482.

Kruse C. A., Molleston M. C., Parks E. P., Schiltz P. M., Kleinschmidt-DeMasters B. K. and Hickey W. F. (1994) A rat glioma model, CNS-1, with invasive characteristics similar to those of human gliomas: a comparison to 9L gliosarcoma. *Journal of neuro-oncology* **22,** 191-200.

Laws E. R., Jr., Goldberg W. J. and Bernstein J. J. (1993) Migration of human malignant astrocytoma cells in the mammalian brain: Scherer revisited. *Int J Dev Neurosci* **11,** 691-697.

LeCouteur R. A. (1999) Current concepts in the diagnosis and treatment of brain tumours in dogs and cats. *The Journal of small animal practice* **40,** 411-416.

Lehr H. A., van der Loos C. M., Teeling P. and Gown A. M. (1999) Complete chromogen separation and analysis in double immunohistochemical stains using Photoshop-based image analysis. *J Histochem Cytochem* **47,** 119-126.

Li S. W., Qiu X. G., Chen B. S., Zhang W., Ren H., Wang Z. C. and Jiang T. (2009) Prognostic factors influencing clinical outcomes of glioblastoma multiforme. *Chinese medical journal* **122,** 1245-1249.

Li X. N., Parikh S., Shu Q., Jung H. L., Chow C. W., Perlaky L., Leung H. C., Su J., Blaney S. and Lau C. C. (2004) Phenylbutyrate and phenylacetate induce

differentiation and inhibit proliferation of human medulloblastoma cells. *Clin Cancer Res* **10,** 1150-1159.

Lipsitz D., Higgins R. J., Kortz G. D., Dickinson P. J., Bollen A. W., Naydan D. K. and LeCouteur R. A. (2003) Glioblastoma multiforme: clinical findings, magnetic resonance imaging, and pathology in five dogs. *Veterinary pathology* **40,** 659-669.

Livingston R. B., Venditti J. M., Cooney D. A. and Carter S. K. (1970) Glutamine antagonists in chemotherapy. *Advances in pharmacology and chemotherapy* **8,** 57-120.

Lopez C. A., Feng F. Y., Herman J. M., Nyati M. K., Lawrence T. S. and Ljungman M. (2007) Phenylbutyrate sensitizes human glioblastoma cells lacking wild-type p53 function to ionizing radiation. *International journal of radiation oncology, biology, physics* **69,** 214-220.

Louis D. N. (2006) Molecular pathology of malignant gliomas. *Annual review of pathology* **1,** 97-117.

Lugini L., Matarrese P., Tinari A., Lozupone F., Federici C., Iessi E., Gentile M., Luciani F., Parmiani G., Rivoltini L., Malorni W. and Fais S. (2006) Cannibalism of live lymphocytes by human metastatic but not primary melanoma cells. *Cancer research* **66,** 3629-3638.

Lyons S. D., Sant M. E. and Christopherson R. I. (1990) Cytotoxic mechanisms of glutamine antagonists in mouse L1210 leukemia. *The Journal of biological chemistry* **265,** 11377-11381.

Maclean K. H., Dorsey F. C., Cleveland J. L. and Kastan M. B. (2008) Targeting lysosomal degradation induces p53-dependent cell death and prevents cancer in mouse models of lymphomagenesis. *The Journal of clinical investigation* **118,** 79-88.

Maes W., Deroose C., Reumers V., Krylyshkina O., Gijsbers R., Baekelandt V., Ceuppens J., Debyser Z. and Van Gool S. W. (2008) In vivo bioluminescence imaging in an experimental mouse model for dendritic cell based immunotherapy against malignant glioma. *Journal of neuro-oncology*.

Magee B. A., Potezny N., Rofe A. M. and Conyers R. A. (1979) The inhibition of malignant cell growth by ketone bodies. *Aust J Exp Biol Med Sci* **57,** 529-539.

Magill G. B., Myers W. P., Reilly H. C., Putnam R. C., Magill J. W., Sykes M. P., Escher G. C., Karnofsky D. A. and Burchenal J. H. (1957) Pharmacological and initial therapeutic observations on 6-diazo-5-oxo-1-norleucine (DON) in human neoplastic disease. *Cancer* **10,** 1138-1150.

Marsh J., Mukherjee P. and Seyfried T. N. (2008a) Drug/diet synergy for managing malignant astrocytoma in mice: 2-deoxy-D-glucose and the restricted ketogenic diet. *Nutrition & metabolism* **5,** 33-37.

Marsh J., Mukherjee P. and Seyfried T. N. (2008b) Akt-dependent proapoptotic effects of caloric restriction on late-stage management of a PTEN/TSC2-deficient mouse astrocytoma. *Proc. Amer. Assoc. Cancer Res.* **14,** 7751-7762.

Martinez-Murillo R. and Martinez A. (2007) Standardization of an orthotopic mouse brain tumor model following transplantation of CT-2A astrocytoma cells. *Histology and histopathology* **22,** 1309-1326.

Matheson B. K., Adams J. L., Zou J., Patel R. and Franklin R. B. (2007) Effect of metabolic inhibitors on ATP and citrate content in PC3 prostate cancer cells. *The Prostate* **67,** 1211-1218.

Mazurek S., Boschek C. B., Hugo F. and Eigenbrodt E. (2005) Pyruvate kinase type M2 and its role in tumor growth and spreading. *Seminars in cancer biology* **15,** 300-308.

McGirt M. J., Chaichana K. L., Gathinji M., Attenello F., Than K., Ruiz A. J., Olivi A. and Quinones-Hinojosa A. (2008) Persistent outpatient hyperglycemia is independently associated with decreased survival after primary resection of malignant brain astrocytomas. *Neurosurgery* **63,** 286-291; discussion 291.

McKeehan W. L. (1982) Glycolysis, glutaminolysis and cell proliferation. *Cell biology international reports* **6,** 635-650.

Medina M. A. (2001) Glutamine and cancer. *The Journal of nutrition* **131,** 2539S-2542S; discussion 2550S-2531S.

Montcourrier P., Mangeat P. H., Valembois C., Salazar G., Sahuquet A., Duperray C. and Rochefort H. (1994) Characterization of very acidic phagosomes in breast cancer cells and their association with invasion. *Journal of cell science* **107 (Pt 9),** 2381-2391.

Moonda A. and Fatteh S. (2009) Metastatic colorectal carcinoma: an unusual presentation. *Journal of cutaneous pathology* **36,** 64-66.

Moore T., Beltran L., Carbajal S., Strom S., Traag J., Hursting S. D. and DiGiovanni J. (2008) Dietary energy balance modulates signaling through the Akt/mammalian target of rapamycin pathways in multiple epithelial tissues. *Cancer prevention research (Philadelphia, Pa* **1,** 65-76.

Moreadith R. W. and Lehninger A. L. (1984) The pathways of glutamate and glutamine oxidation by tumor cell mitochondria. Role of mitochondrial NAD(P)+-dependent malic enzyme. *The Journal of biological chemistry* **259,** 6215-6221.

Morris A. A. (2005) Cerebral ketone body metabolism. *J Inherit Metab Dis* **28,** 109-121.

Mukherjee P., Abate L. E. and Seyfried T. N. (2004) Antiangiogenic and proapoptotic effects of dietary restriction on experimental mouse and human brain tumors. *Clin Cancer Res* **10,** 5622-5629.

Mukherjee P., El-Abbadi M. M., Kasperzyk J. L., Ranes M. K. and Seyfried T. N. (2002) Dietary restriction reduces angiogenesis and growth in an orthotopic mouse brain tumour model. *Br J Cancer* **86,** 1615-1621.

Naidu A. S., Paulsson M. and Wadstrom T. (1988) Particle agglutination assays for rapid detection of fibronectin, fibrinogen, and collagen receptors on Staphylococcus aureus. *Journal of clinical microbiology* **26,** 1549-1554.

Nebeling L. C., Miraldi F., Shurin S. B. and Lerner E. (1995) Effects of a ketogenic diet on tumor metabolism and nutritional status in pediatric oncology patients: two case reports. *J. Am. Coll. Nutr.* **14,** 202-208.

Nelson D. L. and Cox M. M. (2005) *Lehninger Principles of Biochemistry,* Fourth Edition. W.H. Freeman and Company, New York.

Newsholme E. A., Crabtree B. and Ardawi M. S. (1985) The role of high rates of glycolysis and glutamine utilization in rapidly dividing cells. *Bioscience reports* **5,** 393-400.

Newsholme P., Gordon S. and Newsholme E. A. (1987) Rates of utilization and fates of glucose, glutamine, pyruvate, fatty acids and ketone bodies by mouse macrophages. *The Biochemical journal* **242,** 631-636.

Newsholme P., Costa Rosa L. F., Newsholme E. A. and Curi R. (1996) The importance of fuel metabolism to macrophage function. *Cell biochemistry and function* **14,** 1-10.

Newsholme P., Procopio J., Lima M. M., Pithon-Curi T. C. and Curi R. (2003a) Glutamine and glutamate--their central role in cell metabolism and function. *Cell biochemistry and function* **21,** 1-9.

Newsholme P., Lima M. M., Procopio J., Pithon-Curi T. C., Doi S. Q., Bazotte R. B. and Curi R. (2003b) Glutamine and glutamate as vital metabolites. *Brazilian journal of medical and biological research = Revista brasileira de pesquisas medicas e biologicas / Sociedade Brasileira de Biofisica ... [et al* **36,** 153-163.

Ng W. H., Yeo T. T. and Kaye A. H. (2005) Spinal and extracranial metastatic dissemination of malignant glioma. *J Clin Neurosci* **12,** 379-382.

Oda T. and Maeda H. (1986) A new simple fluorometric assay for phagocytosis. *Journal of immunological methods* **88,** 175-183.

Ortega A. D., Sanchez-Arago M., Giner-Sanchez D., Sanchez-Cenizo L., Willers I. and Cuezva J. M. (2009) Glucose avidity of carcinomas. *Cancer letters* **276,** 125-135.

Ovejera A. A., Houchens D. P., Catane R., Sheridan M. A. and Muggia F. M. (1979) Efficacy of 6-diazo-5-oxo-L-norleucine and N-[N-gamma-glutamyl-6-diazo-5-oxo-norleucinyl]-6-diazo-5-oxo-norleucine against experimental tumors in conventional and nude mice. *Cancer research* **39,** 3220-3224.

Owen O. E., Morgan A. P., Kemp H. G., Sullivan J. M., Herrera M. G. and Cahill G. F., Jr. (1967) Brain metabolism during fasting. *J Clin Invest* **46,** 1589-1595.

Parsons D. W., Jones S., Zhang X., Lin J. C., Leary R. J., Angenendt P., Mankoo P., Carter H., Siu I. M., Gallia G. L., Olivi A., McLendon R., Rasheed B. A., Keir S., Nikolskaya T., Nikolsky Y., Busam D. A., Tekleab H., Diaz L. A., Jr., Hartigan J., Smith D. R., Strausberg R. L., Marie S. K., Shinjo S. M., Yan H., Riggins G. J., Bigner D. D., Karchin R., Papadopoulos N., Parmigiani G., Vogelstein B., Velculescu V. E. and Kinzler K. W. (2008) An integrated genomic analysis of human glioblastoma multiforme. *Science (New York, N.Y* **321,** 1807-1812.

Pellerin L., Bergersen L. H., Halestrap A. P. and Pierre K. (2005) Cellular and subcellular distribution of monocarboxylate transporters in cultured brain cells and in the adult brain. *J Neurosci Res* **79,** 55-64.

Perez-Gomez C., Campos-Sandoval J. A., Alonso F. J., Segura J. A., Manzanares E., Ruiz-Sanchez P., Gonzalez M. E., Marquez J. and Mates J. M. (2005) Co-expression of glutaminase K and L isoenzymes in human tumour cells. *The Biochemical journal* **386,** 535-542.

Persson A. and Englund E. (2008) Different assessments of immunohistochemically stained Ki-67 and hTERT in glioblastoma multiforme yield variable results: a study with reference to survival prognosis. *Clinical neuropathology* **27,** 224-233.

Phillips D., Aponte A. M., French S. A., Chess D. J. and Balaban R. S. (2009) Succinyl-CoA synthetase is a phosphate target for the activation of mitochondrial metabolism. *Biochemistry* **48,** 7140-7149.

Phuphanich S., Baker S. D., Grossman S. A., Carson K. A., Gilbert M. R., Fisher J. D. and Carducci M. A. (2005) Oral sodium phenylbutyrate in patients with recurrent malignant gliomas: a dose escalation and pharmacologic study. *Neuro-oncology* **7,** 177-182.

Pisarenko O. I., Solomatina E. S., Ivanov V. E., Studneva I. M., Kapelko V. I. and Smirnov V. N. (1985) On the mechanism of enhanced ATP formation in hypoxic myocardium caused by glutamic acid. *Basic research in cardiology* **80,** 126-134.

Pless D. D. and Wellner R. B. (1996) In vitro fusion of endocytic vesicles: effects of reagents that alter endosomal pH. *Journal of cellular biochemistry* **62,** 27-39.

Pongratz R. L., Kibbey R. G., Shulman G. I. and Cline G. W. (2007) Cytosolic and mitochondrial malic enzyme isoforms differentially control insulin secretion. *The Journal of biological chemistry* **282,** 200-207.

Portais J. C., Voisin P., Merle M. and Canioni P. (1996) Glucose and glutamine metabolism in C6 glioma cells studied by carbon 13 NMR. *Biochimie* **78,** 155-164.

Quesada A. R., Medina M. A., Marquez J., Sanchez-Jimenez F. M. and Nunez de Castro I. (1988) Contribution by host tissues to circulating glutamine in mice inoculated with Ehrlich ascites tumor cells. *Cancer research* **48,** 1551-1553.

Rabinovitz M., Olson M. E. and Greenberg D. M. (1959) Effect of glutamine analogs on amino acid incorporation into protein of some normal and neoplastic cells in vitro. *Cancer research* **19,** 388-392.

Ranes M. K., El-Abbadi M., Manfredi M. G., Mukherjee P., Platt F. M. and Seyfried T. N. (2001) N -butyldeoxynojirimycin reduces growth and ganglioside content of experimental mouse brain tumours. *Br J Cancer* **84,** 1107-1114.

Reitzer L. J., Wice B. M. and Kennell D. (1979) Evidence that glutamine, not sugar, is the major energy source for cultured HeLa cells. *The Journal of biological chemistry* **254,** 2669-2676.

Rickman D. S., Bobek M. P., Misek D. E., Kuick R., Blaivas M., Kurnit D. M., Taylor J. and Hanash S. M. (2001) Distinctive molecular profiles of high-grade and low-grade gliomas based on oligonucleotide microarray analysis. *Cancer research* **61,** 6885-6891.

Rubinstein L. J. (1972) *Tumors of the Central Nervous System*, Vol. Atlas of Tumor Pathology, p 400. Armed Forces Institute of Pathology, Washington, D.C.

Sato K., Kashiwaya Y., Keon C. A., Tsuchiya N., King M. T., Radda G. K., Chance B., Clarke K. and Veech R. L. (1995) Insulin, ketone bodies, and mitochondrial energy transduction. *Faseb J* **9,** 651-658.

Sauer L. A. and Dauchy R. T. (1978) Identification and properties of the nicotinamide adenine dinucleotide (phosphate)+-dependent malic enzyme in mouse ascites tumor mitochondria. *Cancer research* **38,** 1751-1756.

Scallet A. C., Haley R. L., Scallet D. M., Duhart H. M. and Binienda Z. K. (2003) 3-nitropropionic acid inhibition of succinate dehydrogenase (complex II) activity in cultured Chinese hamster ovary cells: antagonism by L-carnitine. *Annals of the New York Academy of Sciences* **993,** 305-312; discussion 345-309.

Scherer H. J. (1938) Structural Development in gliomas. *American Journal of Cancer* **34,** 333-351.

Scherer H. J. (1940a) The forms of growth in gliomas and their practical significance. *Brain* **63,** 1-34.

Scherer H. J. (1940b) The Pathology of Cerebral Gliomas. A Critical Review. *J Neurol,* 147-177.

Scholzen T. and Gerdes J. (2000) The Ki-67 protein: from the known and the unknown. *Journal of cellular physiology* **182,** 311-322.

Schwimmer C., Lefebvre-Legendre L., Rak M., Devin A., Slonimski P. P., di Rago J. P. and Rigoulet M. (2005) Increasing mitochondrial substrate-level phosphorylation can rescue respiratory growth of an ATP synthase-deficient yeast. *The Journal of biological chemistry* **280,** 30751-30759.

Selman C., Kerrison N. D., Cooray A., Piper M. D., Lingard S. J., Barton R. H., Schuster E. F., Blanc E., Gems D., Nicholson J. K., Thornton J. M., Partridge L. and Withers D. J. (2006) Coordinated multitissue transcriptional and plasma

metabonomic profiles following acute caloric restriction in mice. *Physiological genomics* **27,** 187-200.

Seyfried T. N. and Mukherjee P. (2005a) Targeting energy metabolism in brain cancer: review and hypothesis. *Nutr Metab (Lond)* **2,** 30.

Seyfried T. N. and Mukherjee P. (2005b) Targeting energy metabolism in brain cancer: review and hypothesis. *Nutrition & metabolism* **2,** 30-38.

Seyfried T. N., el-Abbadi M. and Roy M. L. (1992) Ganglioside distribution in murine neural tumors. *Mol Chem Neuropathol* **17,** 147-167.

Seyfried T. N., Sanderson T. M., El-Abbadi M. M., McGowan R. and Mukherjee P. (2003) Role of glucose and ketone bodies in the metabolic control of experimental brain cancer. *Br J Cancer* **89,** 1375-1382.

Seyfried T. N. and Shelton L. M. (2010) Cancer as a Metabolic Disease. *Journal of Nutrition and Metabolism* **7**.

Shapiro W. R., Ausman J. I. and Rall D. P. (1970) Studies on the chemotherapy of experimental brain tumors: evaluation of 1,3-bis(2-chloroethyl)-l-nitrosourea, cyclophosphamide, mithramycin, and methotrexate. *Cancer research* **30,** 2401-2413.

Singh K. K., Kulawiec M., Still I., Desouki M. M., Geradts J. and Matsui S. (2005) Inter-genomic cross talk between mitochondria and the nucleus plays an important role in tumorigenesis. *Gene* **354,** 140-146.

Smith Q. R. (1991) *Fuel Homeostasis and the Nervous System*, Vol. 291. Plenum Press, New York.

Soto A. M. and Sonnenschein C. (2004) The somatic mutation theory of cancer: growing problems with the paradigm? *Bioessays* **26,** 1097-1107.

Souba W. W. (1993) Glutamine and cancer. *Annals of surgery* **218,** 715-728.

Spivak J. L. (1973) Phagocytic tumour cells. *Scandinavian journal of haematology* **11,** 253-256.

Stevenson C. B., Ehtesham M., McMillan K. M., Valadez J. G., Edgeworth M. L., Price R. R., Abel T. W., Mapara K. Y. and Thompson R. C. (2008) CXCR4 expression is elevated in glioblastoma multiforme and correlates with an increase in intensity and extent of peritumoral T2-weighted magnetic resonance imaging signal abnormalities. *Neurosurgery* **63,** 560-569; discussion 569-570.

Swirski F. K., Nahrendorf M., Etzrodt M., Wildgruber M., Cortez-Retamozo V., Panizzi P., Figueiredo J. L., Kohler R. H., Chudnovskiy A., Waterman P., Aikawa E., Mempel T. R., Libby P., Weissleder R. and Pittet M. J. (2009) Identification of splenic reservoir monocytes and their deployment to inflammatory sites. *Science (New York, N.Y* **325,** 612-616.

Szatmari T., Lumniczky K., Desaknai S., Trajcevski S., Hidvegi E. J., Hamada H. and Safrany G. (2006) Detailed characterization of the mouse glioma 261 tumor model for experimental glioblastoma therapy. *Cancer science* **97,** 546-553.

Szentirmai O., Baker C. H., Lin N., Szucs S., Takahashi M., Kiryu S., Kung A. L., Mulligan R. C. and Carter B. S. (2006) Noninvasive bioluminescence imaging of luciferase expressing intracranial U87 xenografts: correlation with magnetic resonance imaging determined tumor volume and longitudinal use in assessing

tumor growth and antiangiogenic treatment effect. *Neurosurgery* **58,** 365-372; discussion 365-372.

Taha M., Ahmad A., Wharton S. and Jellinek D. (2005) Extra-cranial metastasis of glioblastoma multiforme presenting as acute parotitis. *Br J Neurosurg* **19,** 348-351.

Teller J. K., Fahien L. A. and Davis J. W. (1992) Kinetics and regulation of hepatoma mitochondrial NAD(P) malic enzyme. *The Journal of biological chemistry* **267,** 10423-10432.

Tennant D. A., Duran R. V., Boulahbel H. and Gottlieb E. (2009) Metabolic transformation in cancer. *Carcinogenesis* **30,** 1269-1280.

Thibault A., Cooper M. R., Figg W. D., Venzon D. J., Sartor A. O., Tompkins A. C., Weinberger M. S., Headlee D. J., McCall N. A., Samid D. and et al. (1994) A phase I and pharmacokinetic study of intravenous phenylacetate in patients with cancer. *Cancer research* **54,** 1690-1694.

Tisdale M. J. (1984) Role of acetoacetyl-CoA synthetase in acetoacetate utilization by tumor cells. *Cancer Biochem Biophys* **7,** 101-107.

Vander Heiden M. G., Cantley L. C. and Thompson C. B. (2009) Understanding the Warburg effect: the metabolic requirements of cell proliferation. *Science (New York, N.Y* **324,** 1029-1033.

VanItallie T. B. and Nufert T. H. (2003) Ketones: metabolism's ugly duckling. *Nutr Rev* **61,** 327-341.

Veech R. L. (2004) The therapeutic implications of ketone bodies: the effects of ketone bodies in pathological conditions: ketosis, ketogenic diet, redox states, insulin resistance, and mitochondrial metabolism. *Prostaglandins Leukot Essent Fatty Acids* **70,** 309-319.

Vince G. H., Bendszus M., Schweitzer T., Goldbrunner R. H., Hildebrandt S., Tilgner J., Klein R., Solymosi L., Christian Tonn J. and Roosen K. (2004) Spontaneous regression of experimental gliomas--an immunohistochemical and MRI study of the C6 glioma spheroid implantation model. *Experimental neurology* **190,** 478-485.

Warburg O. (1931) *The Metabolism of Tumours,* p 327. Richard R. Smith, New York.

Warburg O. (1956) On the origin of cancer cells. *Science (New York, N.Y* **123,** 309-314.

Weinberg J. M., Venkatachalam M. A., Roeser N. F. and Nissim I. (2000) Mitochondrial dysfunction during hypoxia/reoxygenation and its correction by anaerobic metabolism of citric acid cycle intermediates. *Proceedings of the National Academy of Sciences of the United States of America* **97,** 2826-2831.

Wen P. Y. and Kesari S. (2008) Malignant gliomas in adults. *The New England journal of medicine* **359,** 492-507.

Williamson D. H., Mellanby J. and Krebs H. A. (1962) Enzymic determination of D(-)-beta-hydroxybutyric acid and acetoacetic acid in blood. *Biochem J* **82,** 90-96.

Xie Q., Thompson R., Hardy K., DeCamp L., Berghuis B., Sigler R., Knudsen B., Cottingham S., Zhao P., Dykema K., Cao B., Resau J., Hay R. and Vande Woude

G. F. (2008) A highly invasive human glioblastoma pre-clinical model for testing therapeutics. *Journal of translational medicine* **6,** 77.

Youness E., Barlogie B., Ahearn M. and Trujillo J. M. (1980) Tumor cell phagocytosis. Its occurrence in a patient with medulloblastoma. *Archives of pathology & laboratory medicine* **104,** 651-653.

Yuneva M. (2008) Finding an "Achilles' heel" of cancer: the role of glucose and glutamine metabolism in the survival of transformed cells. *Cell cycle (Georgetown, Tex* **7,** 2083-2089.

Zagzag D., Esencay M., Mendez O., Yee H., Smirnova I., Huang Y., Chiriboga L., Lukyanov E., Liu M. and Newcomb E. W. (2008) Hypoxia- and vascular endothelial growth factor-induced stromal cell-derived factor-1alpha/CXCR4 expression in glioblastomas: one plausible explanation of Scherer's structures. *The American journal of pathology* **173,** 545-560.

Zeilhofer H. U., Mollenhauer J. and Brune K. (1989) Selective growth inhibition of ductal pancreatic adenocarcinoma cells by the lysosomotropic agent chloroquine. *Cancer letters* **44,** 61-66.

Zhou W., Mukherjee P., Kiebish M. A., Markis W. T., Mantis J. G. and Seyfried T. N. (2007) The calorically restricted ketogenic diet, an effective alternative therapy for malignant brain cancer. *Nutr Metab (Lond)* **4,** 5.

Zielke H. R., Ozand P. T., Tildon J. T., Sevdalian D. A. and Cornblath M. (1976) Growth of human diploid fibroblasts in the absence of glucose utilization. *Proceedings of the National Academy of Sciences of the United States of America* **73,** 4110-4114